UNIVERSITÀ DEGLI STUDI DI PAVIA

DOTTORATO IN SCIENZE CHIMICHE E FARMACEUTICHE

XXIX CICLO

Coordinatore: Chiar.mo Prof. Mauro Freccero

MECHANISM OF ELECTROCATALYTIC AND PHOTO-ELECTROCATALYTIC REACTIONS BY IN OPERANDO X-RAY ABSORPTION SPECTROSCOPY

Tutore

Prof. Paolo Ghigna

Tesi di Dottorato di

ELISABETTA ACHILLI

a.a. 2015 - 2016

INDEX

ABSTRACT

The purpose of this PhD thesis work is the investigation of the mechanism and the kinetics of electrocatalytic and photo-electrocatalytic reactions by means of *in operando* X-ray Absorption Spectroscopy. The attention has been focused on five electrochemical systems which can be divided into two groups on the basis of their catalytic properties. The first group essentially deals with the catalysis of the water splitting reaction: belonging to this group I firstly considered electrodes constituted of IrO_x, which represents one of the major electrocatalysts in this field. Coupling IrO_x electrocatalyst to a semiconductor like hematite it became possible to obtain and investigate bilayer electrodic systems for light driven water splitting. Afterward, I considered bilayer architectures composed of $Ni(OH)_2$ and hematite, which represent cheaper and more sustainable alternatives to iridium based systems. Finally, some research work was devoted to Cu_2O material, also very promising for photovoltaic applications. The experiments carried out for this materials were aimed at studying the structure and stability of one of the main precursors: copper(II) lactate in alkaline solution. The second group of electrodes plays a key role in the environmental field since comprises materials constituted of silver nanoparticles, which show great potentialities in the electrochemical de-halogenation of organic pollutants. Since the study of electrocatalytic processes involves the presence of systems in their real working conditions, adequate experimental setups and electrochemical devices were required in order to control the physic-chemical conditions of the sample. For each electrodic system the research work consisted of four steps: *(i)* experimental planning and construction of adequate spectro-electrochemical devices according to the subsequent experimental needs (these can be either manually-built or 3D printed); *(ii)* preparation of the electrodic materials (in collaboration with the University of Milan); *(iii) In Situ* and *In Operando* investigation by means of XAS Spectroscopy techniques at the ESRF (European Synchrotron Radiation Facility, Grenoble, France); and *(iv)* data analysis and fitting procedure.

1. INTRODUCTION

In material science, a growing attention is devoted to the study of the mechanism and the kinetics of electrochemical and photo-electrochemical processes based on electrocatalysis. The explanation to this recent interest lies in the wide variety of applications allowed by the electrocatalytic devices. Besides the relevance in the fundamental study, their importance ranges from the energy and environment[1,2] to the biomedical and pharmaceutical[3] fields. A great challenge in the energy field is the direct production of high purity hydrogen from sunlight: photoelectrochemical water splitting represents in principle the ideal energy conversion system. Among the main electrocatalysts for the oxygen evolution reaction, much attention is focused on iridium[1,4,5]. Photoanodes for photo-electrochemical water splitting can be obtained by coupling iridium oxide to a semiconductor like hematite which is UV-Vis light sensitive[6,7]. Furthermore, environmentally friendly copper oxides are being studied as possible candidates for photovoltaic applications because of highly acceptable electrical and optical properties[8]. Much attention has been devoted to the preparation and investigation of Cu_2O films because they are characterized by a band gap of 2 eV, which lies in the acceptable range of window material for photovoltaic applications[8,9]. Another important electrocatalytic process deals with the oxidation of $Ni(OH)_2$: this plays a key role in the fields of charge storage and corrosion[10,11]. Coupling this material to hematite it is possible to obtain bilayer architectures which can also show photo-electrocatalytic activity towards the water splitting reaction. However, very little is present in literature about these systems.

Electrocatalysis can gain a key role also in the environmental field: Ag shows a great electrocatalytic activity toward the electro-dehalogenation of organic

halides[2]. This is particularly important in the case of the C-Cl bond, because of the toxicity of the chlorinated organic compounds. Organic halides are employed in many industrial processes as solvents or building blocks for intermediates and they are utilized as herbicides, fungicides and pesticides in agriculture[12,13]. Electrochemical methods can become an excellent solution for the detoxification of wastes as they provide mild reaction conditions and they avoid secondary pollution effects.

Finally, in the biomedical field, electrocatalysis is employed for many purposes in the development of chemical and biological sensors[3]. The major needs range from the early detection of disease biomarkers or continuous monitoring of glucose and lactate to the early detection of biological warfare agents.

Eletcrocatalysis is a kind of heterogeneous catalysis[14], where further complications arise from the need of a conductive support onto which the catalyst is deposited or chemically bound (permanently or just by charge transfer). The presence of a conductive support often restricts the available specific surface area and therefore the number of active sites. The best strategy to increase the contact area between the electrodic solution and the catalyst is based on the employment of nano-materials, characterized by a large surface/volume ratio. It is important to point out that the mechanism and kinetics at the basis of heterogeneous processes are different if compared to those governing homogeneous reactions. Heterogeneous reactions take place on a surface, characterized by physic-chemical properties different from those of the rest of the mass. The surface presents the so-called dangling bonds and atoms are subject to asymmetric and unbalanced forces. Furthermore, the different crystallographic orientation results in a different arrangement and density of the atoms.

When investigating catalytic processes, one of the crucial points is the evaluation of the oxidation state and local structure of the catalyst and the chemical species involved depending on their chemical, geometric and

electronic surroundings. Thanks to the advent of the third generation synchrotron radiation facilities it has become possible to investigate the fine structure of the absorption coefficient to get information both about the local geometric and electronic structure of matter. X-ray Absorption Spectroscopy (XAS), X-ray Absorption Near Edge Spectroscopy (XANES) and Extended X-ray Absorption Fine Structure (EXAFS) provide a key tool for the determination of the chemical surrounding of atoms and their oxidation states. In addition, time resolved XAS technique can provide useful information concerning kinetics aspects. One of the main limitations of the beamlines lies in their adaptation to the different experimental needs. The study of electrocatalytic and photo-electrocatalytic processes involves the presence of systems in their real working conditions and thus requires adequate experimental set-ups to monitor and control the physic-chemical conditions of the sample. From this we understand the need of developing *in situ* and *in operando* techniques with synchrotron radiation facilities[12]. In the present thesis work synchrotron radiation methods are coupled to electrochemical techniques in order to develop new procedures for investigating the mechanism and the kinetics of electrocatalytic and photo-electrocatalytic processes.

REFERENCES

[1] K. S. Joya, N. K. Subbaiyan, F. D'Souza, and H. J. M. de Groot, *Angew. Chem.* (2012), 51, 9601-9605;

[2] A. Wang, Y. Huang, U. Kumar Sur, D. Wu, B. Ren, S. Rondinini, C. Amatore, Z. Tian, *J. Am. Chem. Soc.* (2010), 132, 9534–9536;

[3] X. Zhang, H. Ju, J. Wang, Electrochemical Sensors, Biosensors and their Biomedical Applications (2011);

[4] H. Junge, N. Marquet, A. Kammer, S. Denurra, M. Bauer, S. Wohlrab, F. Gärtner, M. Pohl, A. Spannenberg, S. Gladiali, and M. Beller, *Chem. Eur. J.* (2012), 18, 12749 – 12758;

[5] A. R. Hillman, M. A. Skopeka, and S. J. Gurmanb, *Phys. Chem. Chem. Phys.* (2011), 13, 5252–5263;

[6] S. D. Tilley, M. Cornuz, K. Sivula, and M. Grätzel, *Angew. Chem.* (2010), 122, 6549 –6552;

[7] L. Badia-Bou, E. Mas-Marza, P. Rodenas, E. M. Barea, F. Fabregat-Santiago, S.Gimenez, E. Peris, and J. Bisquert, *J. Phys. Chem.* (2013), 117, 3826–3833;

[8] L. A. Kosyachenko, Solar Cells Thin Film Technologies (2011);

[9] T. D. Golden, M. G. Shumsky, Y. Zhou, R. A. VanderWerf, R. A. V. Leeuwen, and J. A. Switzer, Chem Matt. (1996), 8, 2499—2504;

[10] J. McBreen, W. E. O'Grady, K. I. Pandya, R. W. Hoffman, and D.E. Sayers, *Langmuir* (1987), 3, 428—433;

[11] J. McBreen, W. E. O'Grady, G. Tourillon, E. Dartyge, A. Fontaine, and K. I. Pandya, *J. Phys. Chem,* (1989), 93, 6308—6311;

[12] J. Simonet, M. Stratmann (Ed.), Electrochemistry applied to organic synthesis: principles and main achievements, encyclopedia of electrochemistry (2007), 5, 317–376;

[13] S. Rondinini, P.R. Mussini, G. Sello and E. Vismara, *J. Electrochem. Soc.* (1998), 145, 1108–1112;

[14] J. D. Blakemore, N. D. Schley, G. W. Olack, Ch. D. Incarvito, G. W. Brudvig, and R. H Crabtree,. *Chem. Sci.* (2011), 2, 94.

2. ELECTROCATALYSIS AND PHOTO-ELECTROCATALYSIS

Electrocatalysis can be considered as the part of electrochemistry that deals with the study of reactions involving species, deposited onto conducting supports, able to change the kinetics and in some cases also the mechanism[1] of the process. As for an example, Fig. 2.1 shows an image of Ag acting as electrocatalyst in the electrodechlorination of benzyl chloride. Electrocatalysts are usually deposited onto the electrodic materials either in the form of nano-particles or in the form of films characterized by high hydration degrees. The intention is to optimize of the utilization of the electrocatalytic material by maximizing the number of active sites involved in the electrochemical process. The performance of electrocatalysts in a particular reaction or application is the result of a complicate interplay between a large number of factors, starting from the nature of the electrocatalytic domain (material, surface area, structure and electron transfer properties) to the interaction between the catalytic particles and the electrodic material.

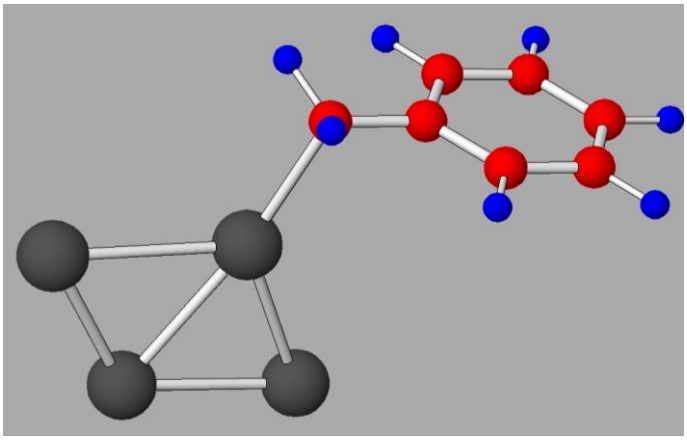

Figure 2.1. Image of Ag acting as a catalyst in the electrodechlorination of benzyl chloride.

A further step in electrocatalysis is represented by photo-electrochemical experiments, in which the elctrocatalytic domain is coupled to a semiconductor part, which is able to interact with UV-Vis light (for example IrO_x and hematite for *light-driven* water splitting). In this case, the irradiation of the electrode with light is able to produce a current, also called *photo-current*[2]. This is strongly dependant on wavelength, electrode potential and solution composition.

The electronic properties of semiconductors are usually described in terms of *band model*[2], in which the *valence band* and the *conduction band* are separated by a forbidden region or *band gap* of energy E_g. The *Fermi energy* E_f is defined as the energy where the probability of a level of being occupied by an electron is ½. It is important to note that for an intrinsic semiconductor neither electrons nor unfilled states exist near E_f. It is useful to define in E_f in a thermodynamic way:

$$E_f = \mu_e - e\varphi \tag{2,1}$$

Where μ_e merely is the familiar chemical potential and φ is the work required to bring a unit positive charge from an infinite distance.

Let us consider the formation of a semiconductor solution interface: when the semiconductor and the solution are brought into contact and electrostatic equilibrium is attained, the Fermi levels should be equal[2]. Fig. 2.2 shows the formation of the junction between a *n*-type semiconductor and a solution containing a redox couple O/R. In this case E_f of the semiconductor is above that in the solution and electrons flow from the semiconductor to the solution. The charge generated at the semiconductor is distributed in a so called *space charge region*. The electric field generated is presented by a bending of the bands. The bending upward is due to a positive charge of the semiconductor with respect to the solution.

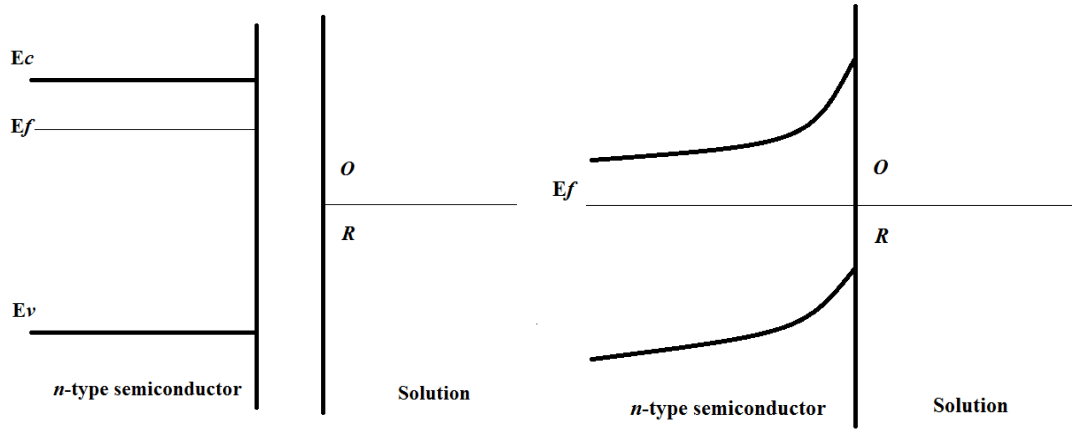

Figure 2.2. Representation of the formation of the junction between a *n*-type semiconductor and a solution containing a redox couple O/R (A) before and (B) after the contact in dark conditions.

When the interface is irradiated by light characterized by larger energy than the band gap, photons are absorbed and electron-hole pairs are generated (Fig. 2.3). A part of these recombine very rapidly but the presence of the space charge region promotes the separation between electrons and holes. The holes, delivered to the surface at an effective potential which is equivalent to the valence band edge, causes the oxidation of R to O while the electrons move into the external circuit. Thus the irradiation of a *n*-type semiconductor promotes photo-oxidation (or determines photo-anodic currents). As a consequence, the photo-oxidation of R to O takes place at less positive applied potentials than those required to carry out this process at an inert metal electrode[2] (Fig. 2.4.A). For this reason we can assess that the light contributes to the oxidation reaction and

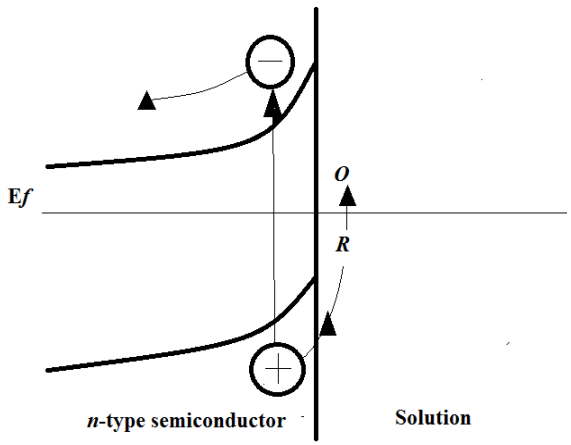

Figure 2.3. Representation of the junction between the *n*-type semiconductor and the solution under illumination.

we can define these processes as “photo-assisted” electrode reactions. Fig. 2.4.A shows the *i-E* curves for a *n*-type semiconductor in dark conditions (curve 1), under illumination (curve 2) and at an inert Pt electrode (curve 3).

Analogous considerations can be made with respect to *p*-type semiconductors (Fig. 2.4.B): in this case the space charge region moves the electrons toward the surface and the holes toward the bulk. Thus the photo-reduction of O to R occurs at more positive applied potentials than those required at an inert metal electrode.

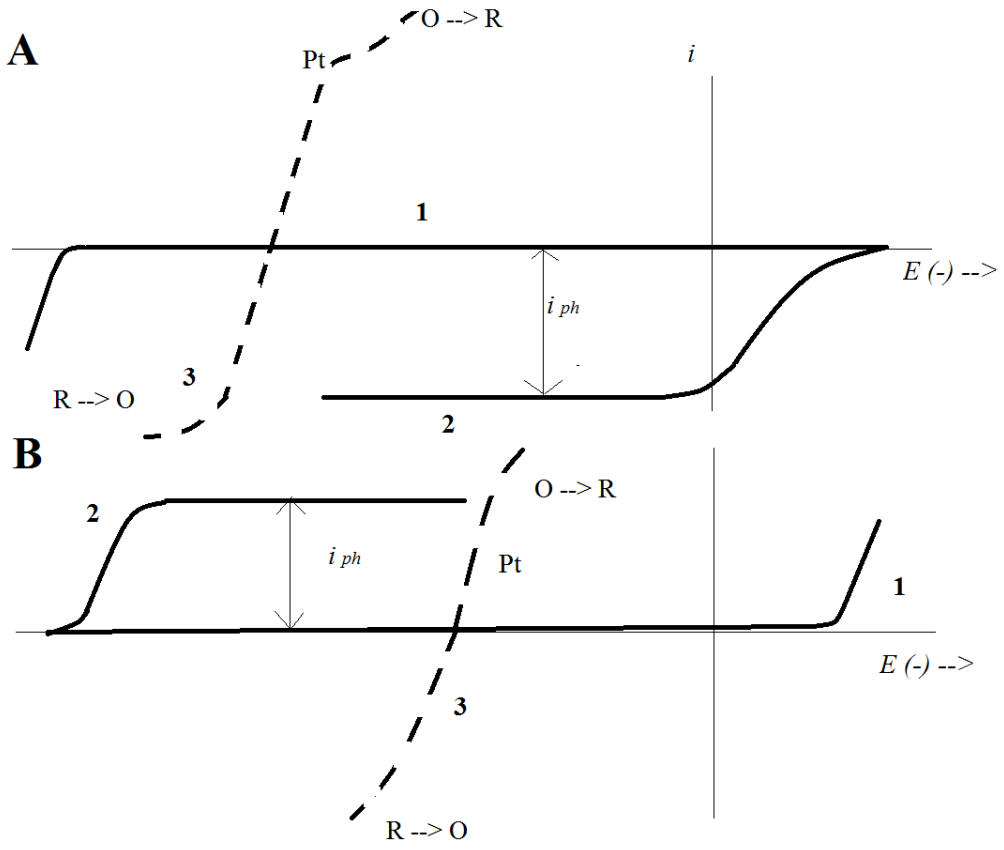

Figure 2.4. Current Vs potential curves for solutions containing couple O/R. A) *n*-type semiconductor in dark conditions (curve 1) and under irradiation (curve 2). B) *p*-type semiconductor in dark conditions (curve 1) and under irradiation (curve 2). For both materials curve 3 represents the current vs potential curve at a platinum electrode.

The efficiency of the photo-electrochemical process is associated to different features of the semiconductor[3]: *(i)* energy position of the band edges, *(ii)* band gap E_p (lying in the visible range), *(iii)* kinetics of hydrogen /oxygen evolution reactions, *(iv)* low resistance for fast migration of photo-generated charge carriers, *(v)* negligible hole electron recombination, *(vi)* stability of the material and *(vii)* chemical formula based on low cost and abundant elements. The theoretical efficiency of the solar-to-chemical energy conversion can be calculated on the base of equation:

$$\eta = \frac{J_{ph} u_{ex} \varphi_{conv}}{S} \tag{2,2}$$

Where J_{ph} is the photon flux, u_{ex} is the exceeding potential generated by the light absorption, φ_{conv} is the quantum yield generated by the photon absorption and S is the total energy for surface unit.

The photo-electrochemical process which has attracted more attention is the light–driven water splitting. This represents the ideal energy conversion system since it allows the direct production of high purity hydrogen from sunlight (Fig. 2.5). According to thermodynamics, the variation in the Gibbs energy associated to the conversion of H_2O to H_2 and O_2 is +237 kJ/mol. Taking into account Nernst equation the ΔE_o of the process is equal to 1.23 V: as a consequence the photo-voltage output must include this value. It is important to note that significant polarization losses and potential drop in the bulk of the electrolyte can be present when oxygen evolution occurs.

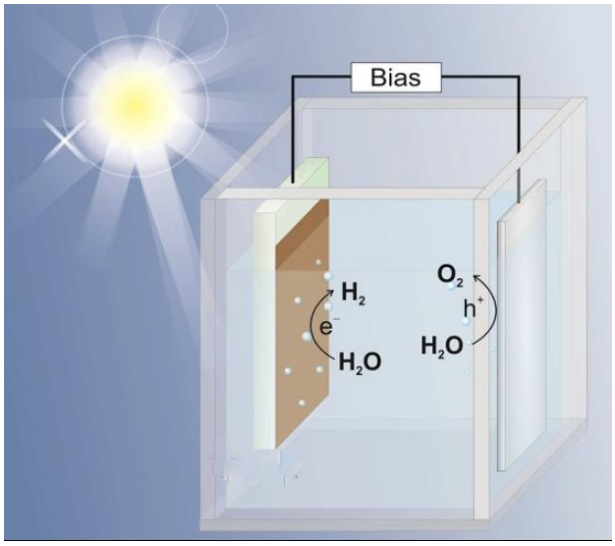

Figure 2.5. Scheme of electrochemical cell for light driven water splitting.

Let us now suppose to couple the semiconductor material to an electrocatalytic overlayer: this is usually composed of a thin film or nanoparticles (Fig. 2.6). It has been demonstrated that the presence of the overlayers determines very high photo-currents and reduced bias[4,5,6]. Nevertheless, the role of the electrocatalyst is still ambiguous and different are the hypothesis concerning its mechanism in the process and whether it actively participates in the reaction or not. According to transient spectroscopy[7], the overlayer is able to reduce the electron density in the semiconductor, while electrochemical impedance spectroscopy[8] suggests that the overlayer acts as storage for holes, thus improving their lifetime and reducing the recombination with electrons. More recently, the overlayer was attributed the effect of optimizing the energy value assumed by the semiconductor surface states[9].

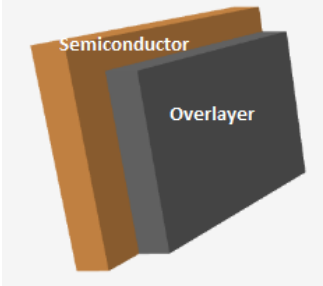

Figure 2.6. Scheme of a semiconductdomain coupled to an overlayer.

Despite the importance of the electrocatalyst/semiconductor interface, the mechanisms of the charge transfer processes are not well understood. The main reason lies in the fact that the semiconductor/overlayer interface is quite difficult to characterize and that charge transfers between the two are hardly directly observable. One of the main goals of this thesis work is to investigate the local chemical and electronic environment of the species involved, during the occurrence of photo-electrocatalytic processes, in order to shed light on the underlying mechanism and the kinetics.

REFERENCES

[1] C. F. Zinola, M. E. Martins, E. P. Tejera, and N. P. Neves Jr. *j. of Electrochem* (2012);

[2] A. J. Bard and L. R. Faulkner, Electrochemical Methods (1980);

[3] A. Fujishima, and K. Honda, *Nature* (1972), 238, 37;

[4] S.D. Tilley, M. Cornuz, K. Sivula, and M. Grätzel, *Angew. Chemie - Int.* (2010), 49, 6405–6408;

[5] D.K. Zhong, and D.R. Gamelin, *J. Am. Chem. Soc.* (2010), 132, 4202–4207;

[6] F. Malara, A. Minguzzi, M. Marelli, S. Morandi, R. Psaro, V. Dal Santo, A. Naldoni, *ACS Catal.* (2015), 5, 5292–5300;

[7] M. Barroso, C. a. Mesa, S.R. Pendlebury, a. J. Cowan, T. Hisatomi, K. Sivula, M. Gratzel, D.R. Klug, and J.R. Durrant, *Proc. Natl. Acad. Sci.* (2012), 109, 15640–15645;

[8] L. Badia-Bou, E. Mas-Marza, P. Rodenas, E.M. Barea, F. Fabregat-Santiago, S. Gimenez, E. Peris, and J. Bisquert, *J. Phys. Chem. C.* (2013), 117, 3826–3833;

[9] L. Steier, I. Herraiz-Cardona, S. Gimenez, F. Fabregat-Santiago, J. Bisquert, S.D. Tilley, and M. Grätzel, *Adv. Funct. Mater.* (2014), 24, 768.

3. THE CHOICE OF THE MATERIALS

One of the main goals in electrocatalysis deals with the synthesis and investigation of nano-materials characterized by high stability in aqueous media over a broad range of pH, temperature and potential. The most important advantage of nano-structured materials lies in their large surface/volume ratio, which allows to gain the maximum number of active sites involved in the occurring electrochemical processes.

In this thesis work the attention is focused on five electrodic systems characterized by important properties as electrocatalysts and photo-electrocatalysts:

(i) iridium oxide films and nano-particles,
(ii) iridium oxide films deposited onto hematite,
(iii) nichel hydroxide films deposited onto hematite,
(iv) copper oxide films and
(v) silver nano-particles.

The importance of the first four systems lies in their high activity as catalysts in the oxygen evolution reaction while silver nano-particles play a key role in the electro-declorination of organic pollutants.

3.1. IrO_x BASED ELECTRODES

Iridium oxide is considered one of the most interesting anode materials and it is employed in many industrial processes[1], such as cathodic protection[2], metal electrowinning[3] and water electrolysis[4]; and in photo-anodes[5]. However, the

turnover mechanism of Ir catalyst in the water splitting reaction has not been clarified yet. In literature it is suggested that the catalytic site acts as redox mediator according to the following reactions[6]:

Higher valence oxide formation:

$$Ir^{2x}O_x + H_2O \rightarrow Ir^{2(x+1)}O_{x+1} + 2H^+ + 2e^- \quad (3,1)$$

Higher valence oxide decomposition:

$$Ir^{2(x+1)}O_{x+1} \rightarrow Ir^{2x}O_x + 1/2O_2 \quad (3,2)$$

The aim of the work described in this thesis is *(i)* to suggest a catalytic cycle for the iridium acting as a single site heterogeneous catalyst in the water splitting process, *(ii)* to study its behaviour during in different chrono-amperometric programs and (iv) to study its role when coupled to a semiconductor for light-driven processes.
Electrodeposited Iridium oxide samples considered are in the form of films and nano-particles.

3.1.1. Ir STANDARDS

The reference samples employed in the XAS investigation are $IrCl_3$ (Alfa Aesar) and pure IrO_2. The latter was obtained from calcination at 700 °C under O_2 flux (50 NL/h) for 2 h of $IrCl_3$, which was previously finely ground for 10 minutes. A proper amount of sample was mixed with cellulose and then pressed to pellets.

3.1.2. IrO_x FILM PREPARATION

The preparation of electrodeposited iridium oxide films (EIROF) was carried out on the basis of a modified version of the method in refs [7] and [8]. This began with the dissolution of 0.0151 g of $IrCl_3 \cdot 3H_2O$ (Alfa Aesar) in 10 ml of Milli-Q water. 100 µl of H_2O_2 (30%) were added after 30 minutes of stirring and then the resulting solution was stirred again for other 30 minutes. 0.0518 g of oxalic acid were added and the solution was kept under stirring for other 10 minutes. Finally, dried K_2CO_3 was added in order to reach pH 10.5. The yellow solution obtained by this procedure turned blue/violet after three days at room temperature. This was used as deposition bath to deposit IrO_x onto a conductive support at constant current density. Suitable samples ware obtained by applying 0.1 mA/cm² for 600 s and using a Pt plate as counter electrode.

3.1.3. IrO_x NANOPARTICLES PREPARATION

IrO_x nanoparticles were obtained from a 17 mM aqueous solution of $IrCl_3 \cdot 3H_2O$ (Alfa Aesar) adjusted to pH 13 by adding 1 M NaOH and then heated at 90 °C for 20 minutes while stirring. Then it was cooled in an ice-bath[9] where a blue suspension was obtained. This was purified by dialysis in a glycerolcontaining SpectrumLabs Spectra/Por 4 Basic cellulose membrane. The powder was then dried at 80 °C in order to obtain powder P1 and finally calcinated. Powder P2 is the result of calcination at 450 °C (temperature ensuring sufficient crystallinity without compromising specific surface area) under O_2 flux. To perform electrochemical analysis, P1 and P2 materials are deposited onto conducting supports by dropcasting 55 µl of a 3.5 mg/ml dispersion (this corresponds to a loading of 1 mg/cm² of iridium): electrodes el_1 and el_2 were obtained respectively. The support is a carbon disposable electrode DRP–P-C11XX

(Dropsens) including an Ag track for the external electrical connection. 2.5 µl of a 0.15 w% Nafion suspension were finally added to improve the adhesion of the powders onto the support.

3.1.4. IrO_x/Fe_2O_3 PHOTO-ANODES

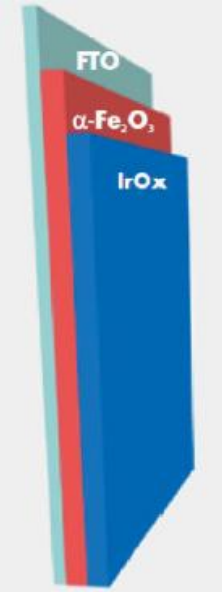

Figure 3.1. Photoanode architecture: IrO_x film in contact with the Fe_2O_3 deposited onto the FTO substrate.

These photo-anodes are composed of IrO_x as elecrocatalytic domain and Fe_2O_3 as semiconductor counterpart (Fig. 3.1). The hematite employed is constituted of α-Fe_2O_3 hierarchical nanoplatelets. This was prepared according to the method described in ref. [10]. IrO_x/Fe_2O_3 electrodes were prepared starting from the deposition bath described before. Two different ways of deposition were performed. *(i)* Photo-electrodeposition of iridium oxide onto Fe_2O_3 was carried out by using Fe_2O_3@FTO (Fluorine-doped Tin Oxide) as working electrode, a saturated calomel electrode as reference and a platinum sheet as counter electrode. *(ii)* Potentiostatic photo-deposition was achieved applying a potential of 0.6 V *vs.* SCE with a LED (λ=400nm, LED ENGINE LZ1-00UA00) as a light source. The deposition time was equal to 15 minutes.

3.2. $Ni(OH)_2/ Fe_2O_3$ SYSTEMS

In addition to their importance as supercapacitors, gel sensors, electrochromic films and rechargeable batteries[11,12], $Ni(OH)_2$ based materials can gain a key role also in the electrocatalytic and photo-electrocatalytic fields. In this thesis, bilayer architectures, in which Ni electrocatalyst is coupled to hematite as

semiconductor, are studied as cheaper alternatives for the photo-electrocatalysis of the water splitting reaction. Two synthesis have been carried out to obtain $Ni(OH)_2/Fe_2O_3$ bilayer electrodes.

(i) $Ni(OH)_2/Fe_2O_3$ Type 1 Electrodes

The synthesis started with the deposition of hematite onto FTO coated glass substrates (Solaronix, 10 Ω/sq.) by thermal solution deposition at 70 °C for 3 h starting from a 0.15 M solution of $Fe_2Cl_3 \cdot 6H_2O$ containing $NaNO_3$ (1 M). pH was maintained equal to 1.5 with HCl[13]. Afterwards the electrodes were calcinated at 550 °C for 1 h and then at 800 °C for 20 min.[14]. Ni-catalyst was deposited onto the hematite layer by applying a constant current density (16 mA/cm^2) for 60 s.: α-Fe_2O_3 electrodes were immersed in a 0.1 M solution of $Ni(NO_3)_2 \cdot 6H_2O$, whose pH was adjusted to 6.6 by NaOH. The solution was first treated with hydrogen for 1 h. Finally, in order to remove any metal ion excess the electrodes were lightly rinsed with deionized water[15].

(ii) $Ni(OH)_2/Fe_2O_3$ Type 2 Electrodes

The first part of the synthesis is the same as that employed for Type 1 electrodes. The difference lies in the deposition of the electrocatalyst: this was deposited onto hematite by electro and photo-deposition. In the former case bilayer systems were obtained by applying 1.23 V (Vs RHE) for 1800 s, in the latter the electrodes were obtained at open circuit potential (Vs Ag/AgCl) for 1200 s. In order to remove any metal ion excess, the electrodes were lightly rinsed with deionized water[15].

3.3. Cu_2O ELECTRODES

Cu_2O represents a low cost, non-toxic and environmental acceptable material, which can be employed in devices for solar energy convesion[16]. Its band gap, characterized by values ranging from 1.96 to 2.38 eV[17], makes it one of the most suitable material among the candidates for photovoltaic applications[18].

One of the most wide-spread and cost-effective methods for preparing Cu_2O films is to electrolyze an alkaline solution of copper sulphate, in which the precipitation of copper hydroxide and oxide is avoided by adding a large excess of lactate ions[19]. Cu_2O films obtained by this way are marked by exceptional activity towards photo-electrochemical water splitting[19]. Their poor stability can be overcome by the employment of protective layers[20]. On the basis of solid state structural determinations[21], lactate ions are thought to form a complex with Cu with 1:2 (Cu:L) stoichiometry, but no direct information is available. Furthermore, Cu(II) alkalyne solutions with lactate in large excess shows a complicate electrochemical behaviour characterized by different peaks in the Cyclic Voltammetry (CV) sweep. This aim of the work described is to shed light on the structure and electrochemical stability of Cu(II) lactate complexes in alkaline solution. The starting bath was composed of 0.2 M $CuSO_4$ (Sigma Aldrich), 3M lactic acid (Fischer Scientific) and 0.5 M K_2HPO_4 (Sigma Aldrich)[19], which acts as a buffer. This solution was subsequently adjusted to pH=12 by adding 2 volumes of 2 M KOH.

3.4. Ag ELECTROCATALYST

The important role played by Ag nanoparticles in electrochemistry is associated to their capabilities in the detoxification of wastes. In particular, Ag is recognized as very powerful catalyst for the electro-dehalogenation of organic

halides[22,23]. This represent a very challenging topic since organic halides are widespread in many industrial processes (like polymer synthesis), in agriculture (herbicides, fungicides, pesticides) and in commercial solvents for industry and housework[24,25]. However, the reason that lies in the exceptional activity of Ag is still not fully understood, even though it has recently been studied the role of adsorption of the organic halide on silver[26]. The *in operando* XAS techniques described in this work allowed to gain a deeper understanding of the electrocatalytic activity of Ag in the electro-dehalogenation of organic halides by investigating the interaction between the Ag electrode and the reactants, the intermediates and the products. In detail, we studied the electroreductive hydrodehalogenation of $CHCl_3$ and bromophenol at carbon supported Ag nanoparticles.

3.4.1. THE PREPARATION OF Ag NANOPARTICLES

Silver nanoparticles were obtained by employing $NaBH_4$ as reducing agent[27,28] More details about the preparation method, morphology, size distribution and aging are reported in [28]. A 20 ml aqueous solution composed of $2.5 \cdot 10^{-4}$ M trisodium citrate dihydrate (which acts as stabilizer) and $1.25 \cdot 10^{-4}$ M $AgNO_3$ (which acts as metallic precursor) was prepared in a conical flask at room temperature. Then, 0.6 ml of an ice-cold freshly prepared 0.1 M $NaBH_4$ solution was added while stirring vigorously. The stirring was slowed down after 30 s and for the next 15 minutes the solution was stirred gently to ensure the removal of $NaBH_4$ excess. Once the nanoparticles were synthesized, NaOH in pellets was added to the colloidal solution in order to precipitate the corresponding solid. When the precipitation was complete, the samples were rinsed with water, at least 3–4 times. Nanoparticles with diameter of ca. 6 nm were obtained (Fig. 3.2.A). Afterwards, the cleaning procedure and the storage for a few days led to

a further growth and to the formation of nanorods characterized by a diameter of ca. 25 nm (Fig. 3.2.B).

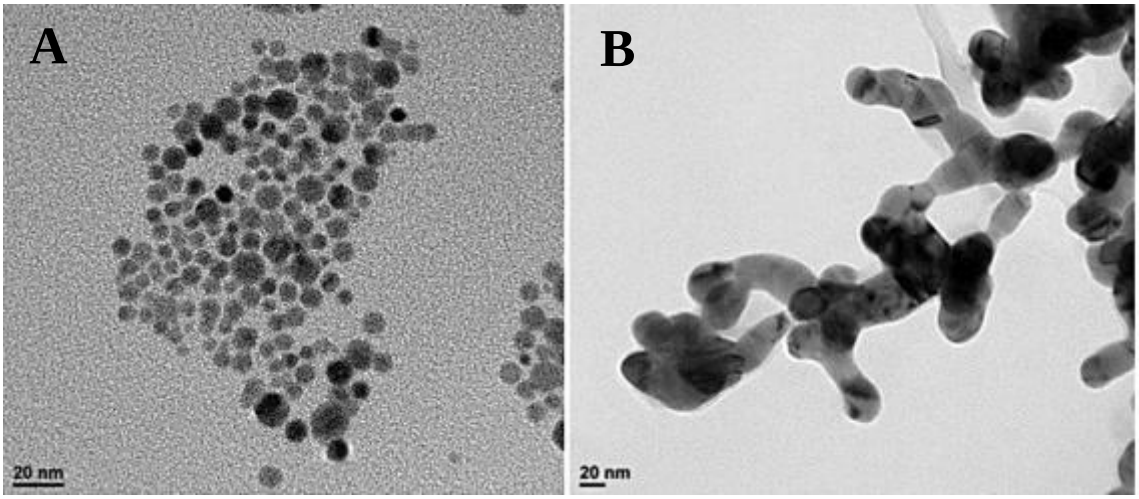

Figure 3.2. TEM pictures of Ag nanoparticles before (A) and after (B) the storage step[28].

Ag nanoparticles were finally deposited by dropcasting onto Glassy Carbon (GC, 1 mm thick, 1 cm^2 area, from Goodfellow) in order to have 0.1 to 0.2 mg/cm^2 of Ag on the electrode.

REFERENCES

[1] A. Minguzzi, F.-R. F. Fan, A. Vertova, S. Rondinini and A.J. Bard, *Chem. Sci.* (2012), 3, 217–229;
[2] J.P. Gueneau de Mussy, J. V. Macpherson and J.-L. Delplancke, *Electrochim. Acta* (2003), 48, 1131-1141;
[3] P. Pedeferri, *Constr. Build. Mater.* (1996), 10, 391;
[4] M. Carmo, D. L. Fritz, J. Mergel and D. Stolten, *Int. J. Hydr. En.* (2013), 38 , 4901-4934;
[5] S. D. Tilley, M. Cornuz, K. Sivula and M. Grätzel, *Angew. Chem.* (2010), 122, 6549 –6552;
[6] S. Trasatti, *Electrochim. Acta* (1984), 29, 1503-1512;
[7] K. Yamanaka, *Jpn. J. Appl. Phys.* (1989), 28, 632–637;
[8] M.A. Petit and V. Plichon, *J. Electroanal. Chem.* (1998), 444, 247–252;
[9] T. Nakagawa, N. S. Bjorge and R. W. Murray, *J. Am. Chem. Soc.* (2009), 131, 15578–15579;
[10] F. Malara, A. Minguzzi, M. Marelli, S. Morandi, R. Psaro and V. Dal Santo, *ACS Catal.* (2015), 5, 5292–5300;
[11] K-W. Nam, W.-S. Yoon, and K.-B. Kim, *Electrochim. Acta* (2002), 47, 3201—3209;
[12] M. Casas-Cabanas, J. Canales-Vazquez, J. Rodriguez-Carvajal, and M. R. Palacin, *J. Am. Chem. Soc.* (2007), 129, 5840—5842;
[13] K. Sivula, R. Zboril, F. Le Formal, R. Robert, A. Weidenkaff, J. Tucek, J. Frydrych, and M. Grä¤tzel, J. Am. Chem. Soc. (2010), 132, 7436-7444;
[14] J. Y. Kim, G. Magesh, D. H. Youn, J.-W. Jang, J. Kubota, K. Domen, and J. S. Lee, *J. S. Sci. Rep.* (2013), 3, 2681;
[15] T. W. Kim, and K.-S. Choi, *Science* (2014), 343, 990—994;
[16] T. D. Golden, M. G. Shumsky, Y. Zhou, R. A. VanderWerf, R. A. Van Leeuwen and J. A. Switzer, *Chem. Mater.* (1996), 8, 2499-2504;
[17] J. Katayama, K. Ito, M. Masuoka and J. Tamaki, *J. Appl. Electrochem.* (2004), 34, 687–692;
[18] M. Benfatto and C. R. Natoli, *Phys. Rev.* (1986), 34, 5774—5781;
[19] A. Paracchino, J. C. Brauer, J.-E. Moser, E. Thimsen and M. Graetzel, *J. Phys. Chem. C* (2012), 116, 7341—7350;
[20] A. Paracchino, V. Laporte, K. Sivula, M. Grätzel and E. Thimsen, *Nat. Mat.* (2011), 10, 456—461;
[21] C. K. Prout, R. A. Armstrong, J. R. Carruthers, J. G. Forrest, P. Murray-Rust and F. J. C. Rossotti, *J. Chem. Soc.* (1968), 2791—2813;
[22] O. Lugaresi, H. Encontre, C. Locatelli, A. Minguzzi, A. Vertova, S. Rondinini and Ch. Comninellis, *Electrochem. Commun.* (2014), 44C, 63–65;
[23] A. Minguzzi, O. Lugaresi, G. Aricci, S. Rondinini and A. Vertova, *Electrochem. Commun.* (2012), 22, 25–28;
[24] J. Simonet, M. Stratmann (Ed.), Electrochemistry applied to organic synthesis: principles and main achievements, encyclopedia of electrochemistry (2007), 5, 317–376;
[25] S. Rondinini, P.R. Mussini, G. Sello and E. Vismara, *J. Electrochem. Soc.* (1998), 145, 1108–1112;
[26] A. Wang, Y.-F. Huang, U.K. Sur, D.-Y. Wu, B. Ren, S. Rondinini, C. Amatore and Z.-Q. Tian, *J. Am. Chem. Soc.* (2010), 132, 9534–9536;
[27] C.M. Sánchez-Sánchez, F.J. Vidal-Iglesias, J. Solla-Gullon, V. Montiel, A. Aldaz, J.M. Feliu and E. Herrero, *Electrochim. Acta* (2010), 55, 8252–8257;
[28] O. Lugaresi, J.V. Perales-Rondón, A. Minguzzi, J. Solla-Gullón, S. Rondinini, J.M. Feliu and C.M. Sanchez-Sanchez, *Appl. Catal. B Environ.* (2015), 163, 554–563.

4. XAFS SPECTROSCOPY AND THE SHORT RANGE INVESTIGATION

Since great part of the materials investigated are in an amorphous state and the structure is interrupted after a few unit cells, a local structure probe is the best tool to study the variations in the structure of the electrodic systems in their working conditions. The techniques presented in this thesis are based on X-ray Absorption Spectroscopy.

XAFS acronym stands for "X-ray Absorption Fine Structure" and refers to the modulations assumed by the X-ray absorption coefficient near and above the absorption edge. Thanks to the advent of the synchrotron radiation sources, a great development of XAFS technique was possible, thus allowing detailed studies of the geometric and electronic properties of materials[1].

This technique, often defined also XAS (X-ray Absorption Spectroscopy), can be divided into two regimes:

(i) XANES (X-ray Absorption Near Edge Spectroscopy), which refers to the absorption coefficient up to 30÷50 eV above the absorption edge, and

(ii) EXAFS (Extended X-ray Absorption Fine Structure), which refers to the energy interval within the XANES region and about 1000 eV above the edge.

4.1 X-RAY ABSORPTION

If a collimated beam of monochromatic X-rays travels trough matter, it loses intensity proportionally to the original intensity and the thickness *x*:

$$dI = -\mu I dx \tag{4,1}$$

The *linear absorption coefficient* μ represents the proportionality constant. Integrating Eq. (4,1) we obtain:

$$\frac{I}{I_0} = e^{-\mu x} \tag{4,2}$$

where I_0 and I are the incident and the transmitted X-ray intensities referred to the passage through the homogeneous sample of thickness x [1]. As the X-ray energy is gradually increased, the *absorption coefficient* μ decreases. This trend is interrupted by discontinuities which correspond to the *absorption edges* and are generated when the photon energy is large enough to extract an electron from the core levels. Its kinetic energy corresponds to the difference between the initial energy and the binding energy. The ejected *photo-electron* can be described as a spherical wave: its wave-lenght decreases as the energy increases. If the *photo-absorber* is isolated, the absorption coefficient would be characterized by a very simple and smooth behaviour. In this case the final states are a continuum of free-electron states and the absorption coefficient has no fine structure. For molecules and condensed systems, when the photo-absorber is not isolated, the *photo-ionization* process is more complicated. The ejected photo-electron can be *back-scattered* by the surrounding atoms generating an ingoing spherical wave (Fig. 4.1). The phase relationship between the outgoing and the incoming wave depends on the photo-electron wavelength and on the inter-atomic

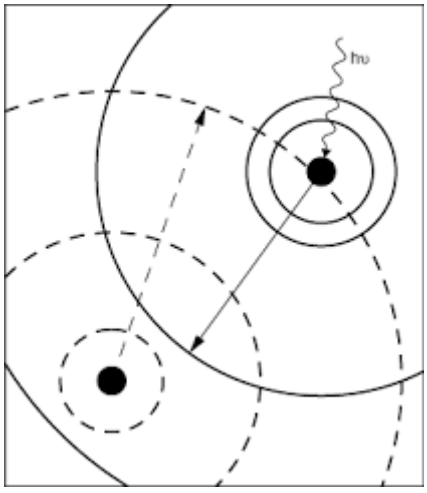

Figure 4.1. Outgoing (full line) and backscattered (dashed line) spherical waves.

distance. As a consequence, the final photoelectron stationary state is the superposition of the outgoing and the incoming spherical waves. The variation of phase relationship as a function of the photon energy affects the final state amplitude at the core site, generating an interference phenomenon, responsible for the modulation in the absorption coefficient. The distance between absorber and *back-scatterer* atoms is related to the frequency of EXAFS oscillations. Their amplitude is proportional to the number of back-scattering atoms.

4.2 X-RAY FLUORESCENT RADIATION

The absorption of a photon determines the excitation of an atom. This can relax through several mechanisms, such as the emission of X -rays, *Auger* electrons or *secondary electrons*. For core levels with energies ≥ 10 kev and elements with high atomic number Z the radiation emission is the most important phenomenon. When an inner shell vacancy is filled by an outer shell electron, X-rays are generated and their energy corresponds to the difference of the two shells. Conventionally, the energy level in which the core hole is generated determines the name of the fluorescence line, which can be K, L and M. The K_α, K_β, and K_γ lines, in descending order of intensity, correspond to electronic transitions from the L, M, and N shells to the K shell. The radiative probability, defined as ε_f, represents the ratio of emitted X-rays to the number of primary vacancies created. It's a monotonically increasing function of the atomic number Z. The total de-excitation probability per unit time determines the core-hole lifetime. The deeper the core hole and the larger the atomic number Z, the larger is the number of upper levels from which an electron can come to fill the hole and thus the shorter is the core hole lifetime. This is typically situated in the range $10^{-15} \div 10^{-16}$ s.

4.3 THE EXAFS FUNCTION

The fine structure of the absorption coefficient $\mu_{el}(\omega)$ reflects the variation of the final photo-electron stationary state $|\psi_f>$ evaluated at the core site of the initial state $|\varphi_i>$, as a function of the photo-electron energy $\hbar\omega$. The final state $|\varphi_f>$ contains structural information and the absorption coefficient becomes:

$$\mu(\omega) \propto \left|\langle\varphi_i|\widehat{\eta\cdot\bar{r}}|\varphi_f\rangle\right|^2 \tag{4,3}$$

EXAFS can be considered as the modulation of the absorption rate, normalized to the background absorption $\mu_0(E)$ and is given by:

$$\chi(E) = \frac{\mu(E) - \mu_0(E)}{\mu_0(E)} \tag{4,4}$$

$\chi(E)$ can be related to the structural parameters converting the energy E into the photoelectron wavevector k by:

$$k = \sqrt{\frac{2m}{\hbar^2}(E - E_0)} \tag{4,5}$$

This transformation of $\chi(E)$ in E space generates $\chi(k)$ in k space.
Considering a system of two atoms, an absorber i and a back-scatterer j, and assuming the muffin tin[1] approximation for the potential experienced, EXAFS signal can be described by Eq. (4,6):

$$\chi(k) = \left(\frac{1}{kr_j^2}\right)|f(k,\pi)|\sin\left[2kr_j + \phi(k)\right] \tag{4,6}$$

Where r_j is the vector joining the two atomic positions, f the backscattering amplitude and $\phi(k)$the phase-shift.

If the systems is composed of a larger number of atoms, EXAFS equation can be obtained by summing each bi-atomic contribution. Neglecting the multiple-scattering contribution and thus assuming the single scattering approximation we obtain:

$$\chi(k) = \left(\frac{1}{k}\right)\sum_j \left(\frac{1}{r_j^2}\right) Im\left\{f_j(k,\pi)e^{2i\delta_1}e^{2ikr_j}\right\} \tag{4,7}$$

Intrinsic and extrinsic inelastic effects are now taken into account and EXAFS equation becomes:

$$\chi(k) = \left(\frac{S_0^2}{k}\right)\sum_j \left(\frac{e^{-\frac{2r_j}{\lambda}}}{r_j^2}\right) Im\left\{f_i(k,\pi)e^{2i\delta_1}e^{2kr_j}\right\} \tag{4,8}$$

Furthermore, if atoms can be grouped into different coordination shells (N_s atoms of the same species at distance R_s) this form of the equation is obtained, in which the contribution of each coordination shell is separated:

$$\chi(k) = \left(\frac{S_0^2}{k}\right)\sum_s N_s Im\left\{f_s(k,\pi)e^{2i\delta_1}\left(e^{-2r_s/\lambda}/r_s^2\right)e^{2ikr_s}\right\} \tag{4,9}$$

This form of the EXAFS function evidences the parameter N_s, representing the coordination number of a specific shell.

It is important to point out that the thermal motion of atoms and the structural disorder affect every real physical system. Taking into account this phenomenon Eq. (4,10) is obtained:

$$\chi_s(k) = \left(\frac{S_0^2}{k}\right) N_s Im\left\{ f_s(k,\pi) e^{2i\delta_l} \int \rho(r) \left(\frac{e^{-\frac{2r}{\lambda}}}{r^2}\right) e^{2ikr} dr \right\} \tag{4,10}$$

This form of the equation corresponds to the Fourier Transform of the $\rho(r)$ function.

The main purpose in EXAFS data analysis is to recover the distribution function $\rho(r)$ from the experimental signal in order to get the structural parameters

$$\chi(k) = \sum_j N_j S_i(k)\, F_j(k) e^{-2\sigma_j^2 k^2} e^{\frac{-2r_j}{\lambda_i(k)}} \frac{\sin\left(2kr_j + \phi_{ij}(k)\right)}{kr_j^2} \tag{4,11}$$

$F_j(k)$ represents the backscattering amplitude from each of the N_j neighbouring atoms of the j type, marked by the Debye-Waller factor σ_j^2. This accounts both for the thermal vibration (harmonic vibration is assumed) and for the static disorder (Gaussian pair distribution) at a distance r_j. Since the electronic phenomenon involved takes place in a time interval of the order of 10^{-23} s, it is not possible to distinguish between static distortions and thermal vibration (10^{-8} – 10^{-12} s). The term e^{-2r_j/λ_j} is due to inelastic losses in the scattering process due to the neighbouring atoms and the medium in between, being λ_j the

medium free path. $S_i(k)$ represents the amplitude reduction factor caused by the shake up/off processes at the central atom. EXAFS modulations are determined by : (*i*) the backscattering amplitude ($N_j F_j(k)$), modified by the reduction factors and the distance dependence, (*ii*) the sinusoidal oscillation, which is a function of the interatomic distances ($2kr_j$) and the phase shift ($\phi_{ij}(k)$). The larger the distance *r*, the higher will be the frequency oscillation.

4.4 THE XAFS EXPERIMENT

In a standard XAFS experiment the absorption coefficient μ is recorded as a function of the photon energy [1,2]. The experimental setup is made up of three parts (Fig. 4.2): an optical part, composed of a monochromator and several mirrors, an apparatus for the sample holder and a detector for measuring the absorption coefficient.

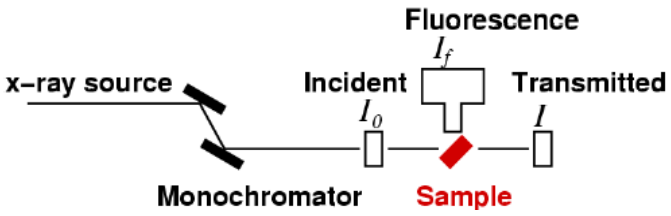

Figure 4.2 Experimental setup in a standard XAFS experiment.

The X-ray absorption signal can be measured by means of two different instrumental configurations corresponding to two different modes: *(i)* the *transmission mode* and *(ii)* the *fluorescence mode*. In a transmission experiment, the intensity of the X-ray beam is measured before and after the sample absorption and the absorption coefficient can be obtained from Eq. (4,2). This method is applicable when the intensity of the transmitted beam (I_t) is sufficiently different from that of the incident beam (I_o), in other words when

the sample concentration should be sufficiently large. The fluorescence mode is employed if the absorbing species is a very tiny fraction of the entire sample (for concentrations lower than 1 %) so that its contribution to the total absorption is negligible. In this case the detector is placed at 90° with respect to the direction of the incident beam and the intensity I_f of the fluorescence emitted at a frequency ω_f is measured as a function of the incident energy $\hbar\omega$. On the basis of the hypothesis that the incident beam and the fluorescent beam are separated by an angle of 45°, for a thick sample it is possible to demonstrate that[2]:

$$I_f(\omega) = I_o(\omega)\left(\frac{\Omega}{4\pi}\right)\eta\frac{\mu_A(\omega)}{\left[\mu_{tot}(\omega) + \mu_{tot}(\omega_f)\right]} \qquad (4,12)$$

This relationship shows that the intensity of the fluorescent beam I_f is proportional to: *(i)* the intensity of the incident beam ($I_o(\omega)$), *(ii)* the solid angle due to the detector acceptance ($\frac{\Omega}{4\pi}$), *(iii)* the fluorescent yeld (η) and *(iv)* the fraction of the incident beam absorbed by the species A (μ_A/μ_{tot}).
In the present thesis, both the transmission and the fluorescence mode are discussed for the investigation of the local chemical and electronic environment of the electrocatalysts.

4.5 *IN SITU* AND *IN OPERANDO* XAFS

One of the main issues associated to the investigation of electrocatalytic and photo-electrocatalytic processes by means of synchrotron radiation lies in the adaptation of the beamlines to the different experimental needs. In many cases, it is difficult to create adequate setups to monitor and control the physicochemical conditions of the sample. Furthermore, a detailed study of the

systems in their real working conditions is needed[3]. In the experiments described in this thesis different kinds of spectroelectrochemical and photo-spectroelectrochemical devices were designed and build in order to perform XAS measurements both *in situ* and *in operando*[4]. These devices allow electric contact in a three-electrodes assembly composed of: *(i)* a working electrode, onto which the electrocatalytic material is deposited, *(ii)* a Pt counter electrode and *(iii)* a Ag/AgCl reference electrode.

4.5.1. Conventional Spectroelectrichemical Devices

The simplest electrochemical cells used were created manually with conventional tools[5]. An example, shown in Fig. 4.3, consists of a PTFE cell that contains the electrolyte solution (0.5 M aqueous H_2SO_4), a Pt foil counter electrode and the reference electrode (AgCl/Ag in 0.1 M KCl). The reference electrode is separated from the solution by a salt bridge consisting in a glass pipette filled with agar containing 0.2 M aqueous $KClO_4$. One side of the cell includes a hole that matches with the working electrode area. The working electrode is held between the PTFE cell and a polypropylene plate that also includes a hole for the X-rays beam.

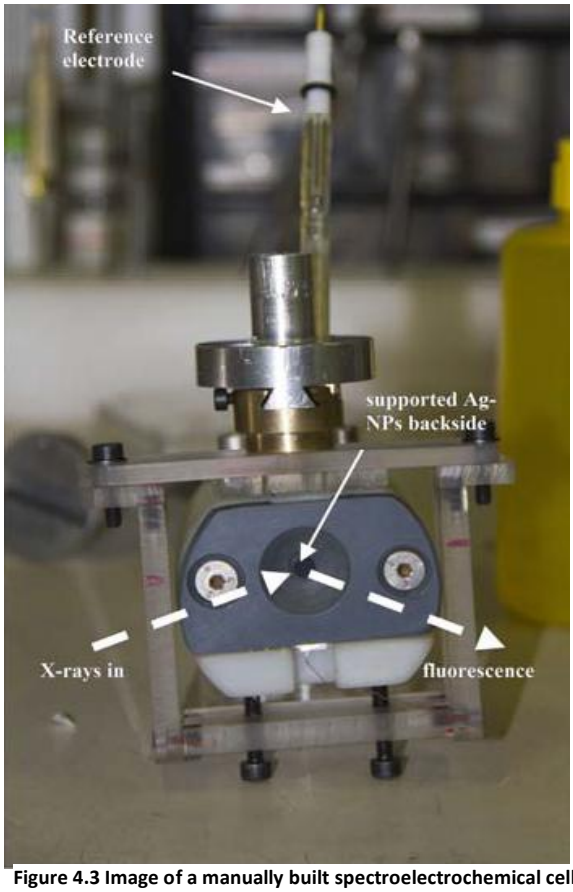

Figure 4.3 Image of a manually built spectroelectrochemical cell with the three-electrode setup.

This is ideal when combining

electrocatlysis to spectroscopy and was employed in the investigation of the electrocatalytic process of water splitting by IrO_x films[6].

4.5.2. 3D-Printed Photo-Spectroelectrochemical Devices

More complications arise when the electrocatalyst is coupled to a semiconductor in photoelectrochemical architectures. In this case, the experiments are carried out in presence of both UV-Vis illumination (acting as a "pump") and X-ray illumination (acting as a "probe"). As a consequence, the interference of the all the materials present should be taken into consideration and the electrochemical devices should be compact and small enough to guarantee an easy and fast experimental setup in the beamline hutch.

The employment of a 3D printer based on the use of photopolymers represents the easiest and fastest way to produce efficient photo-spectroelectrochemical devices characterized by details that would be difficult to obtain by means of a standard subtractive manufacturing technologies. For example, it is possible to control the thickness of the electrolytic solution avoiding problems associated to X-ray attenuation coefficient by water. Furthermore, we can obtain small and curved canals for the counter and reference electrodes ensuring electric contact between the different parts of the cell. In the photo-electrochemical experiments described in this thesis, a photopolymer based printer (Objet 30 Pro, Objet-Stratasys) was employed in order to create adequate electrochemical devices. The printer is based on the use of photopolymeric resins that are laid down on the printing bed in a liquid form and polymerized using a UV lamp. The devices were printed at a layer resolution of 28 μm, that is the height of each deployed layer, while the in-plane printing error was about 1 μm/1 mm. The devices were obtained using the VeroWhite material[7], an opaque rigid photopolymeric polyacrilic resin characterised by an adequate stiffness and resistance to

chemicals. This material is characterized by high resistance to temperatures and mechanical stresses forced: the resin has a softening temperature of 52-54 °C (measured with ASTM standard DMA) and has a Heat Deflection Temperature (HDT) of about 45-50 °C (measured with ASTM standard D-648-06 and D-648-07). Furthermore, the prototyped object is marked by a little porosity and the water absorption parameter ranges from 1.1% - 1.5 % within 24 hours. These characteristics make the 3D printed devices adequate for the experimental conditions required.

Thanks to this electrochemical cells it was possible to combine synchrotron based methods to complementary techniques in order to study the mechanism of the photo-electrocatalytic processes under investigation. Fig. 4.4 shows one of the different types of 3D-printed devices employed. One of the most important features of this cell is represented by the thickness of the electrolyte chamber, limited to 1 mm because of the X-ray absorption of water.

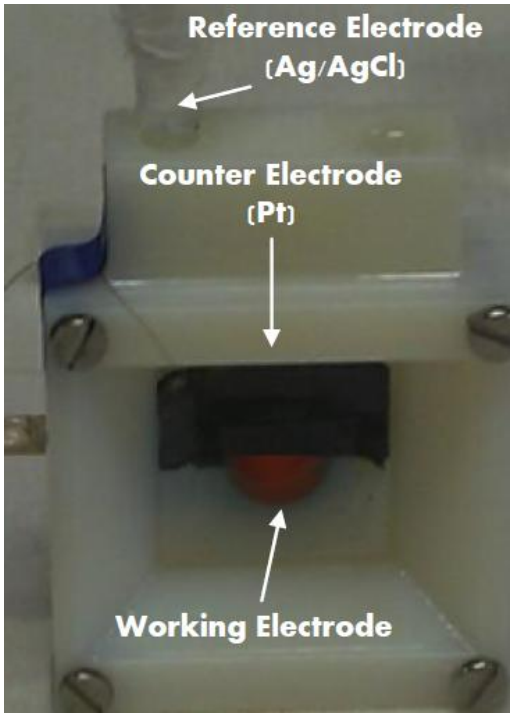

Figure 4.4. Image of a 3D printed photo-spectroelectrochemical cell mounted with the three-electrode setup.

The other 3D-printed cell schematized in Fig. 4.5 represents a modified version of the previous one. The main differences are two: *(i)* the presence of an additional recevoir in the main body of the device and *(ii)* the circular hole generated in the rectangular cover. The recervoir is open at the upper side and electrically connected by the electrolyte. The advantages of this new feature lie in the room devoted to the lodging of the counter electrode (in electric contact with the photoanode) and in the presence of a static place for the electrolyte in

order to overcome problems due to possible radiation damages such as local heating or radical formations, induced by the X-ray irradiation.

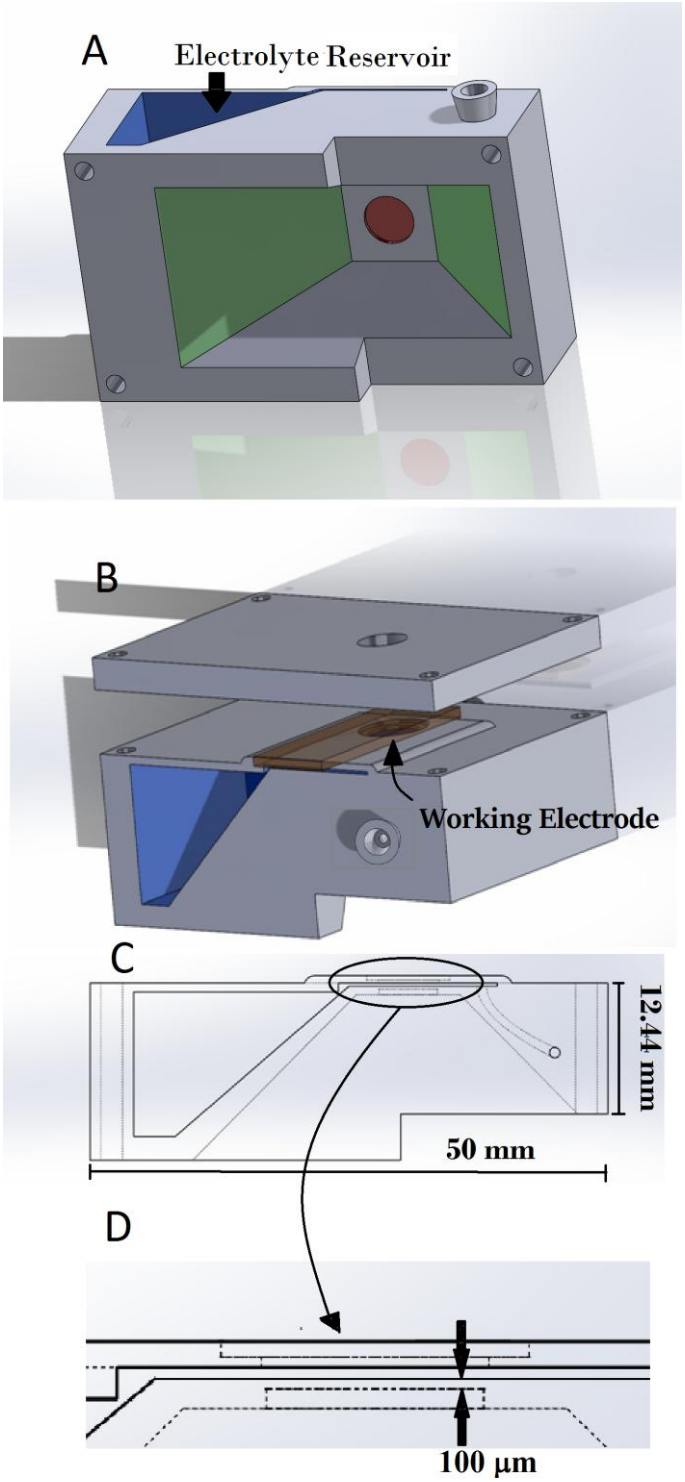

Figure 4.5. Scheme of the "modified" 3D-printed photo-spectroelectrochemical cell showing the electrolyte recervoir (A), the rectangular cover with circular hole (B), the curved canal connecting the reference electrode to the inner part of the cell (C) and the working electrode lodging (D)

The circular hole generated in the rectangular hole, representing the second important characteristic of the device, presents a window in correspondence of the working electrode thus allowing to carry out UV-Vis illumination at the back side of the hematite. Thanks to this shrewdness we avoid absorption in the visible region by the IrO_x layer. Crews and bolts held together the main body of the device and the rectangular cover and an O-ring is present in order to ensure tightness and avoid solution leakage.

The insertion of a Pt counter electrode is possible through an upper slot present in the rectangular electrolyte chamber. The reference electrode can be inserted in the device from a hole generated in the upper part. The connection to the electrolyte chamber is made possible by a curved canal characterized by a diameter of 500 μm (Fig. 4.5.C). Finally, this modified cell presents a 100 μm window printed on the front side for the X-ray irradiation (sealing versus the back pressure of the electrolyte is ensured).

4.6. DATA ANALYSIS AND EXAFS FIT STRATEGY

The first step of data analysis consists in converting the measured intensities I to the absorption coefficients μ(E), necessary in order to extract the EXAFS signal χ(k) and perform the Fourier Transform, operation which allows to pass from the k (wave number, Å^{-1}) space to the r (distance, Å) space. The softwares employed for this first part of data analysis are ATHENA[8] (belonging to the set of interactive programs IFEFFIT[9]), VIPER[10], PyMCA[11] and PRESTOPRONTO[12] (in presence of dispersive-XAS data).

4.6.1. EXAFS SIGNAL EXTRACTION

The extraction of the EXAFS signal is carried out through the following steps.

(i) Calculation and subtraction of the *pre-edge* function

This is a smooth function from μ(E) which is subtracted to the experimental signal. It reproduces any instrumental background and other absorption edges of the same element or of any other element present in the sample. The *pre-edge* function is modeled with a straight line obtained by interpolating the pre-edge data, and then extrapolated to the after-edge signal.

(ii) Identification of E_o

E_o represents the threshold energy and is usually chosen in correspondence of the maximum derivative of μ(E).

(iii) Calculation and removal of the *post-edge* function

This function represents the absorption profile due to an isolated photo-absorber ($\mu_0(E)$) and is modeled with a spline of order *n* using the first point of inflection as E_o.

(iv) Normalization

This is a procedure carried out to obtain a signal referred to an absorption of 1 X-ray. After this operation μ(E) ranges from 0 to 1. Fig. 4.6 shows an example of raw XAS spectrum with the *pre-edge* and *post-edge* functions and the result of the normalization procedure.

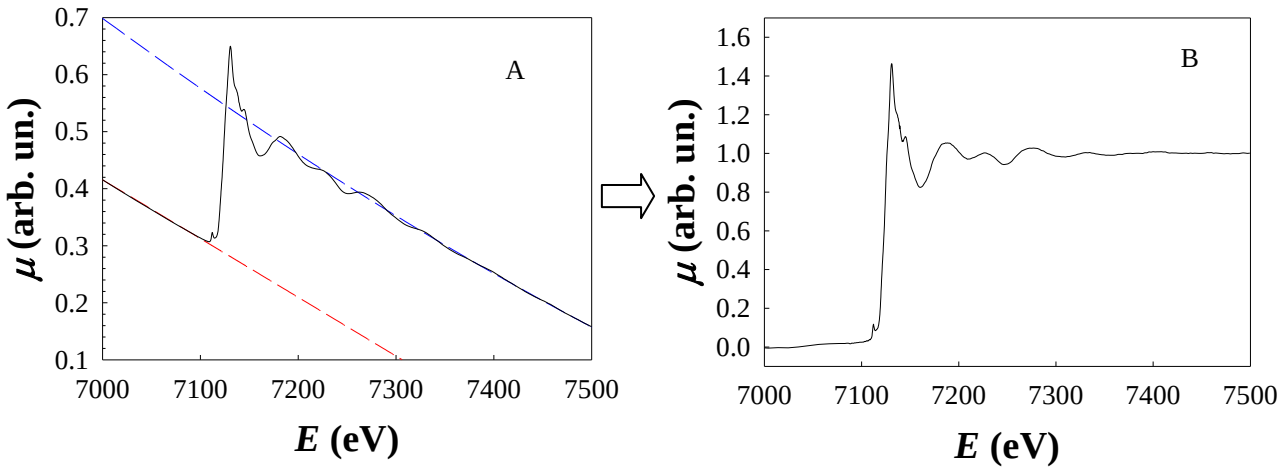

Figure 4.6. A) Example of raw XAS signal and calculated *pre-edge* function (red line) and *post-edge* function (blue line). B) corresponding normalized XAS spectrum.

(v) Passage from E to k

The conversion of the x axis from the energy E to the wavenumber k is necessary to extract the EXAFS signal χ(k) and is achieved by means of the equation (4,5).

(vi) k Weighting

The amplitude of EXAFS oscillations decreases with the increase in energy. Therefore, EXAFS spectra are usually multiplied by k raised to the power of 1, 2, or 3. The power of k is called the k weight (kw). By increasing the k weight, the data at higher k gain more importance, and the Fourier Transform will have larger amplitude for the Fourier components that have a larger contribution at higher k values. Obtaining Fourier Transforms by k weights of 1, 2, and 3 is very useful to distinguish between the atoms in the first and second shell.

Fig. 4.7 illustrates the extracted EXAFS signal weighted by k raised to the power of 2.

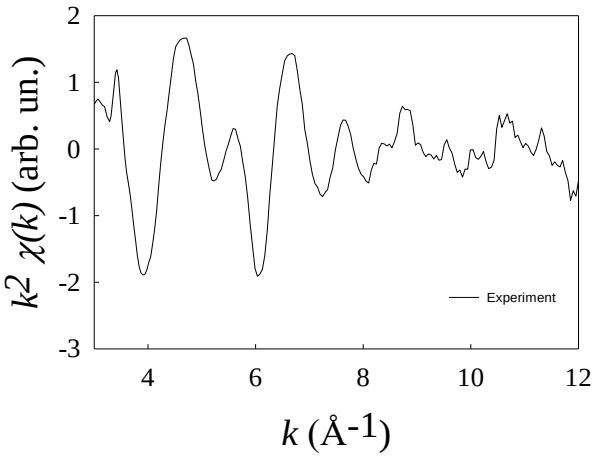

Figure 4.7. Example of extracted EXAFs signal.

4.6.2. FOURIER TRANSFORM AND SPACE *r*

Fourier Transform (FT) is a mathematical operation which allows the transition from one space to its reciprocal. In EXAFS analysis the procedure is employed to pass from the k (wave number, Å^{-1}) space to the r (distance, Å) space:
The equation employed is:

$$F(r) = \int_{k_{min}}^{k_{max}} \chi(k) W(k)\, k^n e^{2ikr} dk \qquad (4,13)$$

Where $\chi(k)k^n$ is the k-weighted EXAFS signal while $W(k)$ represents the so called *window function*, which identifies the k range in which the integral is performed. For values below k_{min} the signal is not reliable and for values above k_{max} the signal-to-noise ratio is too low. By applying the Fourier Transform, in any signal that is a sum of sine waves, it is possible to separate each frequency component in distance r. Fig. 4.8. shows the FT spectrum obtained for the EXAFS signal reported in Fig. 4.7.

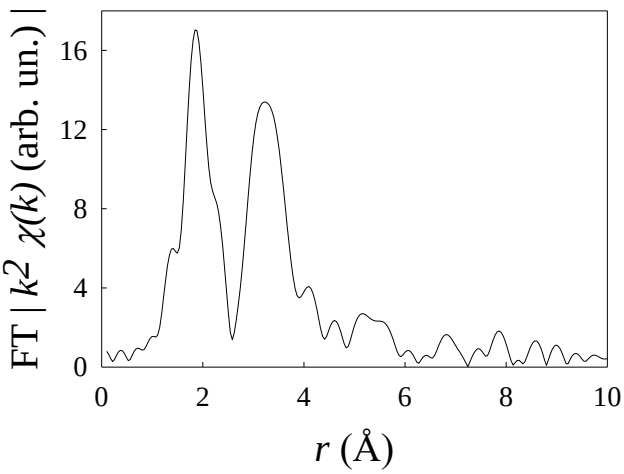

Figure 4.8. Example Fourier Transform of the EXAFS signal.

4.6.3. FIT OF THE EXAFS SIGNAL AND THE FT SPECTRUM

The fit of the EXAFS spectra and the corresponding FT signals is carried out by means of EXCURVE code[13]. The calculation of the atomic scattering parameters (phases and amplitudes) is based on the muffin-tin approximation, in the framework of the Hedin-Lundquist and Von Bart approximations for the exchange and ground state potentials, respectively[14]. This includes the effects of losses due to the electron inelastic scattering. The fittings were made in the k space, using a k^2 weighting scheme and full multiple scattering calculation within the assumed clusters. Thanks to this procedure it is possible to gain information about the population and distance of the coordination *shells* and the disorder in terms of Debye-Waller factor (σ^2). The maximum number of parameters that can be fitted is determined on the basis of the independent points (N_{IDP}, given by the Nyquist theorem):

$$n\ parameters\ \leq N_{IDP} = \frac{2}{\pi}\Delta k \Delta r + 1 \qquad (4,14)$$

whereΔk is the Fourier transformed data range and Δr the region used in the EXAFS analysis. The starting parameters employed in the analysis refer to a cluster constructed on the basis of information present in literature by means of ATOMS[15] and VESTA[16] softwares.

REFERENCES

[1] B. K. Teo, "EXAFS: basic principles and data analysis", Springer-Verlag, 1986;

[2] S. Mobilio, F. Boscherini. "Synchrotron Radiation Basic, methods and Applications", Springer 2015;

[3] A.I. Frenkel, J.A. Rodriguez and J.G . Chen, *ACS Catal.* (2012), 2, 2269—2280;

[4] E. Achilli, A. Minguzzi, A. Visibile, C. Locatelli, A. Vertova, A. Naldoni, S. Rondinini, F. Auricchio, S. Marconi, M. Fracchia, and Paolo Ghigna, *J. Synchrotron Radiat.* (2016), 23, 622—628;

[5] A. Minguzzi, O. Lugaresi, C. Locatelli, S. Rondinini, F. D'Acapito, E. Achilli and P. Ghigna, *Anal. Chem.* (2013), 85, 7009−7013;

[6] A. Minguzzi, O. Lugaresi, E. Achilli, C. Locatelli, A. Vertova, P. Ghigna and S. Rondinini, *Chem. Sci.* (2014), 5, 3591−3597;

[7] http://usglobalimages.stratasys.com;

[8] B. Ravel, and M. Newville, *J. Synchrotron Radiat.* (2005), 12, 537− 541;.

[9] M. Newille, *J. Synchrotron Radiat.* (2001), 8, 322−324;

[10] https://intranet.cells.es/Beamlines/CLAESS/software/viper.html;

[11] http://pymca.sourceforge.net/;

[12] S. J. A. Figueroa, and C. Prestipino, J. Phys.:Conf. Ser. (2016), 712, 012012;

[13] N. Binsted, and S. S. Hasnain, *J. Synchrotron Radiat.* (1996), 3, 185− 196;

[14] S. J. Gurman, N. Binsted, and I. Ross, *J. Phys. C: Solid State Phys.* (1984), 17, 143−152;

[15] http://www.shapesoftware.com/00_Website_Homepage/#anchor_atoms;

[16] http://jp-minerals.org/vesta/en/.

5. IrO_X ELECTROCATALYST AND THE WATER SPLITTING REACTION

The purpose of the work described in this chapter is to shed light on the mechanism of IrO_x acting as a heterogeneous catalyst in the electrochemical reaction of water oxidation and the kinetics associated to chronoamperometric programs. All the experiments have been carried out *in situ* and *in operando* at the E.S.R.F (European Synchrotron Radiation Facility in Grenoble, France) and several techniques have been employed in order to investigate different mechanistic and kinetic aspects associated to the electrochemical processes investigated.

5.1. Ir OXIDATION STATE TURNOVER IN THE ELECTROCHEMICATALYTIC WATER OXIDATION

The most important mechanistic aspect of water oxidation catalysis is related to how the catalyst enters the reaction mechanism[1]. One of the key point in understanding this phenomenon is the evaluation of the oxidation states of the elements involved depending on their chemical surroundings and physicochemical conditions. This is a crucial information since most catalytic cycles imply a continuous, periodic transition between two or more oxidation states of the catalytic center. All measurements were performed on IrO_x film, whose preparation was illustrated in section 3.1.2.

5.1.1. FEXRAV: FAST PRELIMINARY CHARACTERIZATION

Before the acquisition of entire XAFS spectra, Fixed Energy X-ray Absorption Voltammetry (FEXRAV)[2] was performed. This represents a novel, *in situ* X-ray absorption technique for easy and fast preliminary characterization of electrode materials. It consists in recording the X-ray absorption coefficient μ at a fixed energy while varying the electrode potential according to a specific time function. The most used is the triangular-shaped profile, commonly known as cyclic voltammetry (CV).

Measurements were performed at LISA[5] (Linea Italiana di Spettroscopia di Assorbimento, ESRF) at the Ir-L_{III} edge (11215 eV). The ring energy is 6.0 GeV and the current 150-200 mA. A Si(311) double crystal monochromator was used; the harmonic rejection was realized by Pd mirrors, having a cutoff energy of 20 keV, and a 13 element Ge fluorescence detector. All measurements were carried out at room temperature. Data were collected *in situ* by means of the spectroelectrochemical cell described in section 4.5.1. The fixed energy value was chosen equal to 11221.0 eV, in correspondence of the absorption maximum of IrO_2 standard (Fig. 5.1). This choice was done in order to give the maximum contrast between the different oxidation states so that any shift

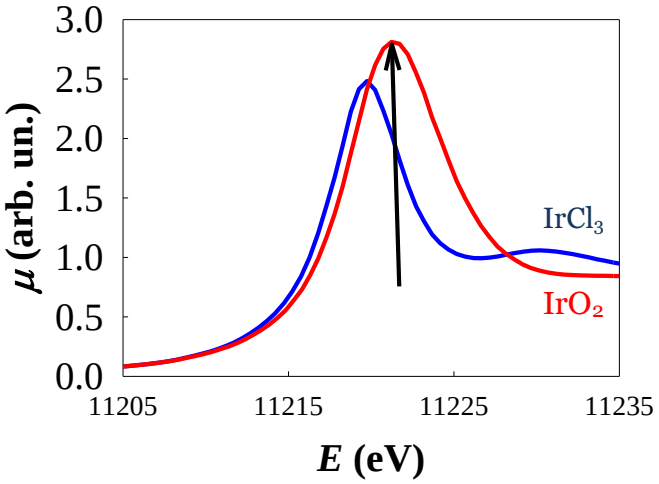

Figure 5.1 Normalized XANES spectra of IrO_2 and $IrCl_3$. The arrow marks the energy chosen for the FEXRAV measurements (11221.0 eV).

from the original oxidation state determines a variation in the absorption coefficient. As we can see from Fig. 5.1, Ir^{3+} and Ir^{4+} standards are characterized by a very similar spectral shape but by a marked shift in the absorption energy. Fig. 5.2 gives the outlook of the white line peak energy and thus the average oxidation state of iridium. Taking into account that the X-ray energy was kept fixed at 11211.0 eV, it is evident that, in the considered potential window, the mean oxidation state of Ir passes across at least three oxidation states.

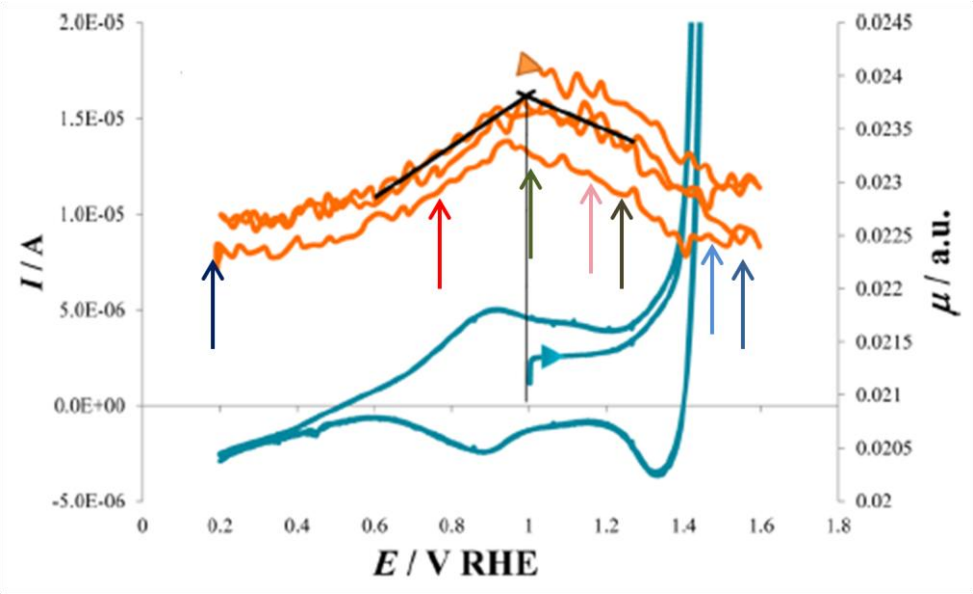

Figure 5.2 FEXRAV spectra (orange lines) and CV (blue lines) of IrO_x film recorded at 11221.0 eV and at 1 mV s^{-1}, both recorded between 0.2 and 1.6 V.

In fact, the maximum of μ is located at about 1 V (RHE), which corresponds to a prevalence of Ir^{4+}. For lower potentials, the decreasing of μ is ascribed to a change in the charge state, likely toward a lower value: Ir^{3+}. Then the absorption coefficient is constant in the 0.2–0.3 V potential range. The $Ir^{3+/4+}$ transition is a well-known feature of IrO_2 in this potential window, already proven and discussed in literature[3,4] and, in terms of I/E characteristics, is indicated by the peaks located at about 0.9 V. When increasing the potential, for E > 1.0 V, the

decrease in the X-ray absorption accounts for an increase in the average oxidation state of Ir. Considering that this decrease is of the same magnitude as the one due to the $Ir^{3+/4+}$ couple, it is safe to assign the higher oxidation state to Ir^{5+}. It is important to note that the formation of Ir^{5+} seems to proceed until 1.4 V, which corresponds to the onset of water oxidation to oxygen:

$$2H_2O \rightarrow O_2 + 4e^- + 4H^+ \qquad (5,1)$$

For larger applied potentials, the absorption coefficient remains constant, likely indicating that the electron withdraw drives reaction (5,1) instead of the Ir charge state. The coloured arrows indicated in Fig. 5.2 show the potential values chosen for the subsequent collection of full XAS spectra for a more detailed investigation.

5.1.2. XANES: THE LOCAL GEOMETRIC AND ELECTRONIC ENVIRONMENT

Ir-L_{III} X-ray Absorption Near Edge Structure (XANES) spectra acquired under different potential values are shown in Fig. 5.3. At first sight it is possible to note variations both in the spectral shapes and in the peaks positions.

2p → 5d electronic transitions give rise to peaks (also called White Lines), which can be modelled by means of Lorentzian functions, whereas electronic transitions towards continuum give rise to steps, which can be simulated by arctangents functions[6]. For both functions the widths are controlled by the core-hole lifetime via an indetermination relationship[7]. Among the other effects contributing to the broadening of the spectral shape, the most important are

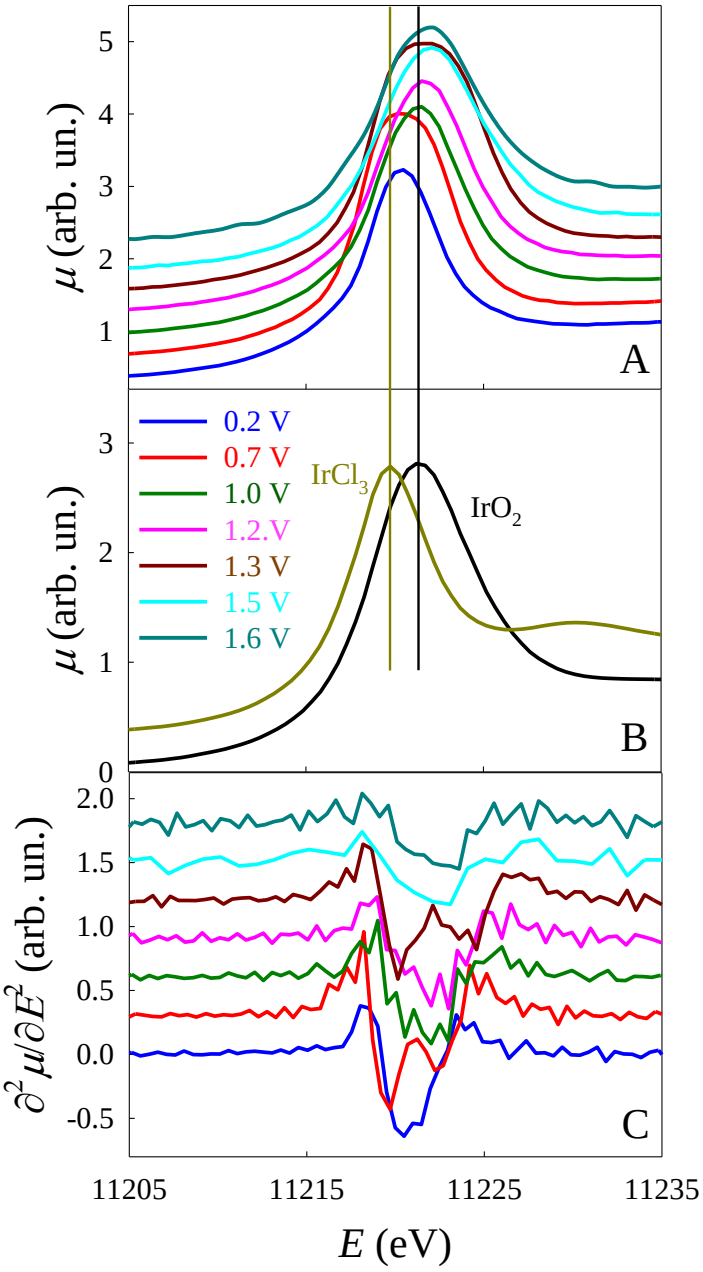

Figure 5.3 A) Normalized Ir-L_{III} edge XANES spectra of the electrodic material under different applied potentials. B) The spectra of bulk IrO_2 and $IrCl_3$ are shown as references. C) The second derivatives are also shown. Vertical lines mark the energies of the WL of $IrCl_3$ and IrO_2.

represented by the spread of the *5d* orbitals into a band and the crystal field splitting. This last effect is expected when isolated $[IrO_6]^{n-}$ octahedral units are present. If these octahedral units interact, the band width of Ir *5d* states is larger and crystal field splitting is no longer observed. Taking into account these assumptions and considering a single charge state of Ir, two are the possible White Lines (WL): *(i)* "narrow", in case of non interacting octahedra or partially filled *5d* orbitals (for example when t_{2g} states are fully occupied) and *(ii)* "broad" in which the transition from the Ir *2p* levels and to the split (t_{2g} + e_g) *5d* states is evident.

As we can see from Fig. 5.3A, for an applied potential of 0.2 V, the WL is very close to that of Ir(III) standard. If the potential is increased up to 1 V, the WL gradually shifts to higher energy values thus indicating a progressive oxidation of Ir. When the applied potential is 1 V the spectrum obtained is almost identical to that of Ir(IV) standard. For applied potentials > 1

V, the WL gradually shifts towards even larger energy values: *(i)* when the potential is 1.2 V a small shift is observed, *(ii)* at 1.3 V the WL is marked by the maximum amplitude and the peak seems to be replaced by a plateau like structure, *(iii)* at 1.5 V the WL is characterized by a broad maximum at *ca.* 11222.1 eV, (iv) at 1.6 V the maximum at ca. 11222.1 eV shows a well clear tail at lower energies. These experimental results confirm what had previously been assumed on the basis of FEXRAV data.

In addition to the variations in the energy positions, XANES spectra of Fig. 5.3 are characterized by differences also in the amplitude and width of the WLs. This can be better noticed if we look at the second derivatives of the spectra (Fig. 5.3.c). For all the applied potentials, excluding 0.7 and 1.3 V, a single peak is observed, thus indicating that crystal field split transitions do not occur. Two remarks should be taken into account: *(i)* Ir(III) in its low spin state (the most stable one) has the t_{2g}^6 electronic configuration and only the transition to e_g state takes place and *(ii)* solid state effects can mask the crystal field splitting via band formation, as in the case of pure IrO_2[8]. Furthermore, distortions of the $[IrO_6]^{n-}$ octahedra result in degeneracy removal, the last effect being expected to be larger for the e_g than for the t_{2g} states. At 0.7 and 1.3 V, two negative peaks are present: this feature corresponds to the transitions to t_{2g} and e_g states and is due to a perfect octahedral environment. It is important to point out that the intensity of these transitions does not reflect directly the statistical count of holes in the t_{2g} and e_g states, as solid state effects like phonon coupling and covalency of the Ir-O bonds should be taken in consideration[8]. According to previous results, the splitting observed at 0.7 and 1.3 V, which is 3.1 and 4.0 eV , is consistent with the presence of Ir(IV) and Ir(V) respectively[8,9]. This result clearly indicates that at 0.7 V Ir(IV) is already formed, at least partially, but with a structure composed of non-interacting octahedra (a sort of "pre-rutile" structure). Similarly, at 1.3 V, Ir assumes the highest oxidation state (V) and also in this case the structure is characterized by non-interacting octahedra.

At larger potential values, 1.5 and 1.6 V, the single peak structure in the second derivative and the presence of a shoulder in the WL evidences that the WL broadening cannot be attributed to the crystal field splitting. The only reasonable explanation to this experimental evidence lies in the co-existence of more than one oxidation state of Ir.

In order to validate rationally what we have said so far, XANES spectra were fitted by means of a combination of Lorentzian and arctangent functions[10] (Fig. 5.4). In detail: *(i)* a single arctangent and a Lorentzian function when a single oxidation state is present and crystal field splitting is not observed (0.2, 1.0 and 1.2 V), *(ii)* two actangent and Lorentzian couples when the WL is too large to account for a single oxidation state and crystal field splitting is not observed (1.5 and 1.6 V); *(iii)* a single arctangent and two Lorentzian functions in the cases in which crystal field splitting is observed (0.7 and 1.3 V). Fig. 5.3 shows the fits obtained for the spectra recorded at 0.2, 1.3 and 1.6 V taken as examples for the three different cases. The energy position of the Lorentzian peak, which provides the maximum in the absorption coefficient μ, is a measure of the oxidation state of Ir at the different working conditions of the electrode material. Assuming an energy shift of 1.3 eV per unit charge of

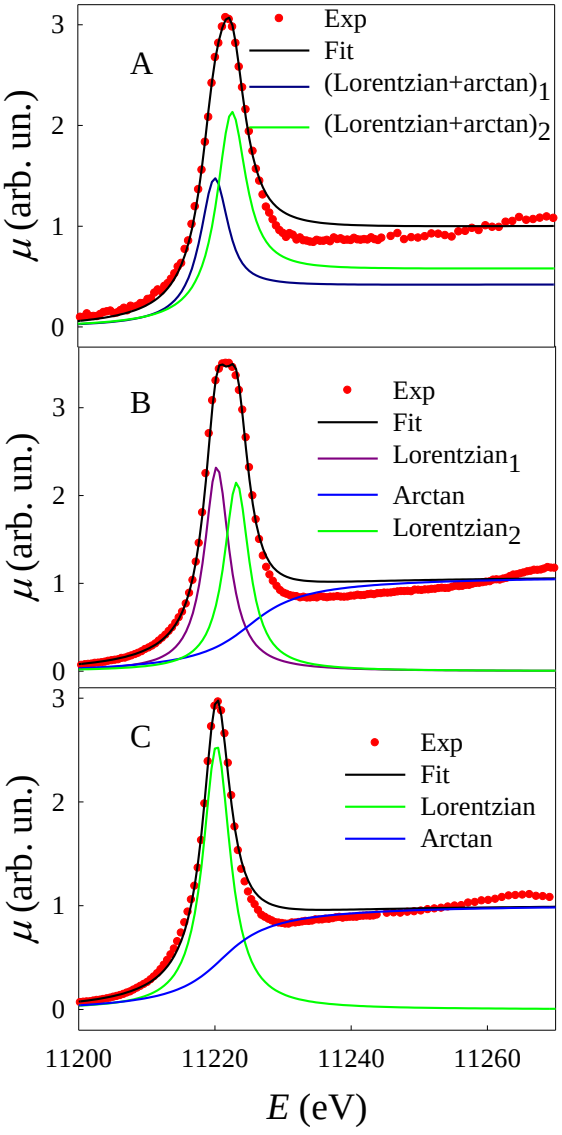

Figure 5.4 Fits of the normalized Ir-L_{III} edge XANES spectra of the electrode material under two applied potentials; A: 1.6 V; B: 1.3 V; C: 0.2 V.

oxidation state[11] (in agreement with the absorption maxima of $IrCl_3$ and IrO_2), it was possible to obtain a relationship between the absorption maximum and the oxidation state of Ir (Fig. 5.5).

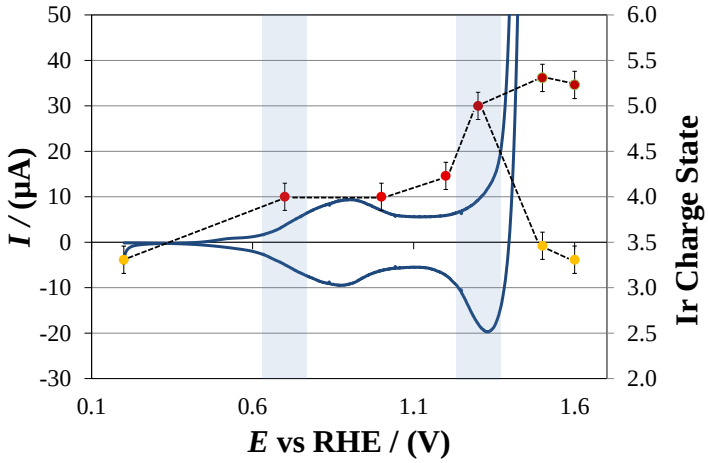

Figure 5.5. Cyclic Voltammetry (blue line, left axis) recorded at 2 mV/s in aqueous 0.5 M H_2SO_4 superimposed to the Ir oxidation state values obtained from the fitting of XANES spectra (yellow to magenta dots, right axes). The light blue areas indicate the potential regions in which the crystal field split was observed.

We can observe that, for applied potentials larger than 1.3 V, two oxidation states of Ir are indicated. This is supported by the larger FWHM of the WL obtained in these electrochemical conditions. It is also important to point out that the integrated area of the WLs are in principle proportional to the number of holes in the Ir *d* states. However, the correlation is not linear because of the fact that Ir presents multiple oxidation states and electronic configurations in different amounts for different potentials. When the applied potential reaches values further than 1.4 V, the formation of gaseous oxygen bubbles at the interface between the electrode and the electrolyte prevents some Ir atoms in the electrode from participating in the reaction. In particular, band formation broadens the *d* states and reduces the amplitude of the WL[12].

5.1.3. A MODEL FOR THE CATALYTIC CYCLE

On the basis of the XANES results obtained, the mechanism proposed for Ir acting as a single site catalyst in the oxygen evolution reaction is schematized in Fig. 5.6.

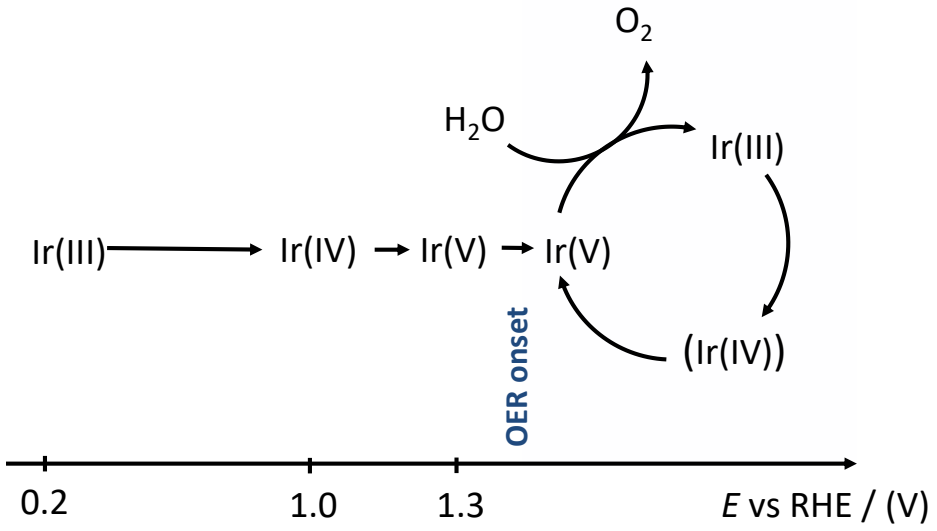

Figure 5.6. Scheme of Ir oxidation states in the considered potential window up to the water oxidation conditions according to the XANES spectra fittings.

At applied potential equal to 0.2 V, results indicate that Ir is present with oxidation state (III). When the potential is 1.0 V, the XANES spectrum recorded is very similar to that of IrO_2 standard thus accounting for Ir present with oxidation state (IV). An increase in the potential to 1.3 V determines an increase in the Ir average oxidation state up to (V). For larger potential values, in oxygen evolution conditions, results obtained clearly show that Ir is present in more than one oxidation state: (III) and (IV).

5.2. IrO_x ELECTROCATALYST IN THE FORM OF NANOPARTICLES WITH DIFFERENT HYDRATION DEGREE

In this section Ir/IrO_x nanoparticles electrodes, made of an Ir core and IrO_2 outer shell, will be taken into account. As described previously in section 3.1.3., two kinds of nano-particles were prepared: P1 and P2 (which was obtained from calcinations of P1) to give el_1 and el_2 respectively. Their purpose lies in providing a higher surface/bulk ratio of Ir-active centers.

Measurements performed onto these samples were carried out at LISA[5] beamline in the same conditions adopted before for the IrO_x films.

Fig. 5.7 illustrates Ir-L_{III} EXAFS signals for the two type of samples recorded at 1.0 V (at which almost all Ir is expected to be present with oxidation state (IV)).

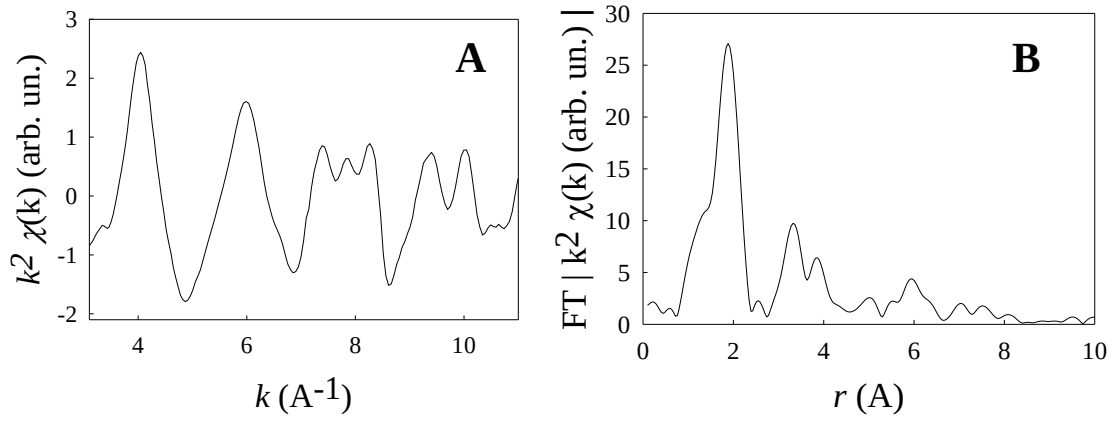

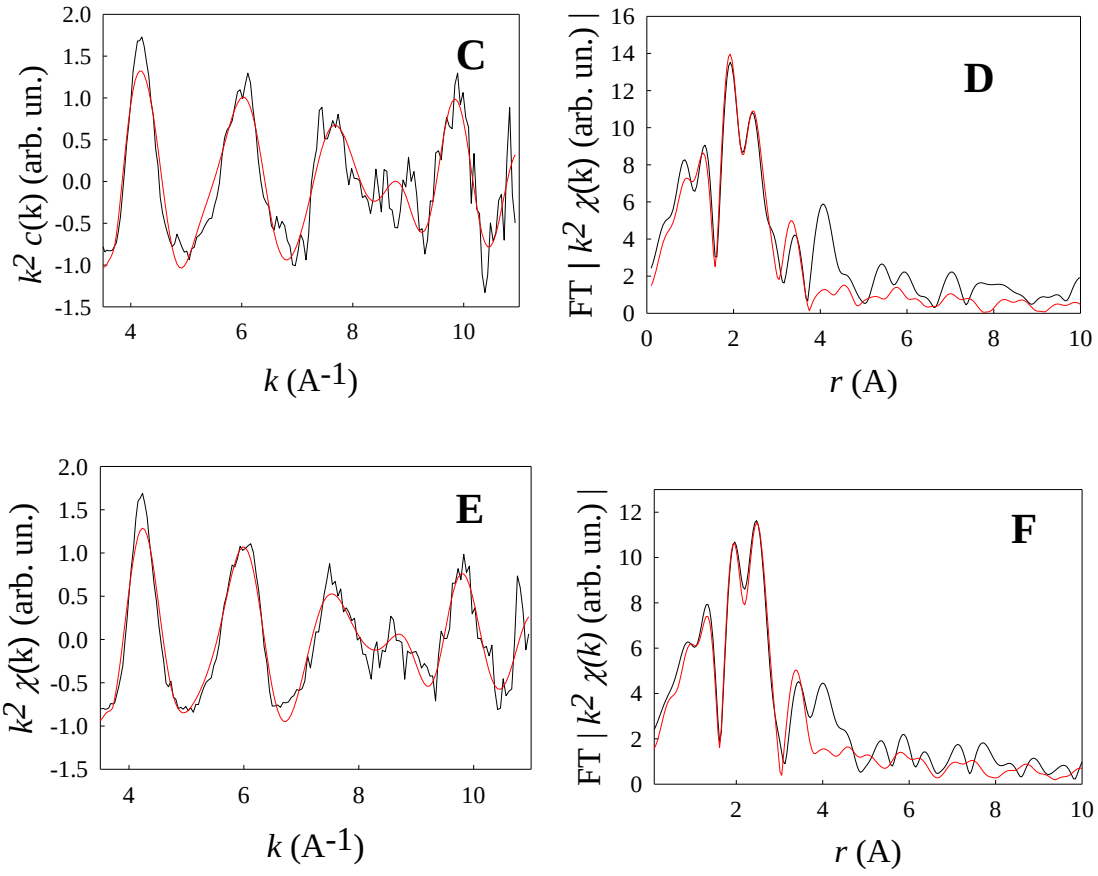

Figure 5.7. Ir-L_{III} edge EXAFS signals and corresponding FT of IrO_2 (A,B) and of sample (el_1) (C, D) and sample (el_2) (E,F). The experimental signal is the black line, whereas the fit according to the model described in the text is represented by the red line.

Oscillations are well visible up to k=11 Å^{-1} and the EXAFS spectrum if IrO_2 standard is shown for reference. This is characterized by a well defined peak at ca. 2 Å, which corresponds to the six O neighbours in the rutile structure, while the peaks between 3.4 and 3.8 Å are mainly due to Ir and O atoms corresponding to the next-nearest neighbours (NNN) of the photo-absorber.

If we compare this spectrum to those of the two samples considered, some differences can be noted. Starting from the EXAFS FT, we can attribute the peak situated at distances around 1.8 Å to the 2 + 4 oxygen atoms surrounding Ir in a distorted octahedral arrangement. The peak observed between 2.8 and 3 Å is due to the presence of an Ir coordination shell, and the peak at ca. 3.5 Å can be explained by the presence of 4 oxygen atoms in the third shell surrounding Ir in

iridium oxide. Furthermore, the observation of peaks at smaller distances (r < 1.8 Å) suggest the presence of heavy atoms as NN (nearest neighbours). Indeed, backscattering functions of heavy atoms are characterized by nonmonotonous trends that result in low frequencies in the EXAFS spectra, thus yielding peaks at small distance values in the EXAFS FT. According to these observations, and on the basis of complementary XRD investigation[13], the structural model used is composed of two clusters: one referred to a IrO_x phase and the other to metallic Ir. The energy shift between the origins of the EXAFS referred to the two different phases, reflecting in turn the different screening of the core electron by the valence electrons, was set at 2 eV. The IrO_x cluster is made up of four coordination shells, whereas the metallic Ir cluster is made up of one shell, as presented in Tab. 5.1.

a) SAMPLE el_1 1.0 V

CLUSTER 1 IrOx, multiplicity: 0.75				
Shell	**N**	**Atom**	**r(Å)**	**σ^2(Å^2)**
1	2	O	1.72(6)	4(2) x10^{-2}
2	4	O	1.96(1)	1(1)x10^{-3}
3	2	Ir	2.97(4)	1(4)x10^{-3}
4	4	O	3.52(4)	0(5) x10^{-3}
CLIUSTER 2 Metallic Ir, multiplicity: 0.25				
Shell	**N**	**Atom**	**r(Å)**	**σ^2(Å^2)**
1	12	Ir	2.63(2)	6(3) x10^{-3}
F: 11.1 %				

b) SAMPLE el_2 1.0 V

CLUSTER 1 IrOx, multiplicity: 0.75				
Shell	**N**	**Atom**	**r(Å)**	**σ^2(Å^2)**
1	2	O	1.72(5)	4(1) x10^{-2}
2	4	O	1.98(1)	3(1)x10^{-3}
3	2	Ir	2.8(2)	2(4)x10^{-2}
4	4	O	3.56(2)	0(1) x10^{-3}
CLUSTER 2 Metallic Ir, multiplicity: 0.25				
Shell	**N**	**Atom**	**r(Å)**	**σ^2(Å^2)**
1	12	Ir	2.64(1)	4(1) x10^{-3}
F: 7.5 %				

Table 5.1. EXAFS Fitting Parameters for Spectra Shown in Fig. 5.7 ((a): Sample el_1, (b): Sample el_2), r: Distances; σ^2: Distance Variances; Coordination Numbers N have been kept constant to their crystallographic values

Quite interestingly, fitting parameters for the two electrodes kept at lower (< 1.0 V) or higher (> 1.0 V) potential values are quite similar to each other and do not

show any significant difference to results obtained for applied potential equal to 1.0 V[13]. In all cases, the IrO_x cluster is marked by a distorted octahedral geometry because the two apical oxygen atoms are situated at a smaller distance if compared to the four equatorial ones. This is usual for iridium oxide films in acidic environment. Because of the highly hydrated form of the IrO_x shell, it is quite straightforward to assign the short Ir—O distance to the coordination with oxide ions, whereas the long Ir—O distance is attributed to the coordination with OH^- (or H_2O). It is also worth pointing out that in our model, keeping the coordination numbers constant, both the short and the long Ir—O distance do not show a sensible variation with the applied potential and the corresponding Debye-Waller factors do not vary (within the experimental error) and are also quite small. A reasonable explanation to this is that increasing the applied potential determines a local reorganization in the film by increasing (decreasing) the number of short (long) distances (which is hardly directly visible by EXAFS due to the intrinsic poor sensitivity to coordination numbers), rather than a simple contraction of the whole coordination IrO_x polyhedral. The iridium capacity to accommodate different bonds with different ligands (oxide and hydroxide ions) at a single Ir site is one of the main reasons for which the hosting of Ir in different oxidation states is very simple in electrodeposited iridium films and nanoparticles. This feature makes these electrodes a very challenging topic in material science. Finally, we should underline that the amount of iridium oxide is larger than the metallic Ir and remains almost the same in all the potential range investigated and for both electrodes.

In Fig. 5.8 the XANES spectra of samples el_1 and el_2 are presented. At reducing potentials (0.3 V), a shift of the main peak toward lower energies accounts for a reduction of Ir (possibly to a state close to Ir(III)). As said before, at 1.0 V, beside the presence of metallic Ir, the position of the WL indicates that Ir is present mainly as Ir(IV). For more oxidizing electrochemical conditions (1.3 and 1.5 V), the shift of the main WL to energy values larger than 11221.3 eV

and the significant spectral weight at lower energies can be explained with the presence of both Ir(III) and Ir(V) (in agreement with the experiment reported in section 5.1.2).

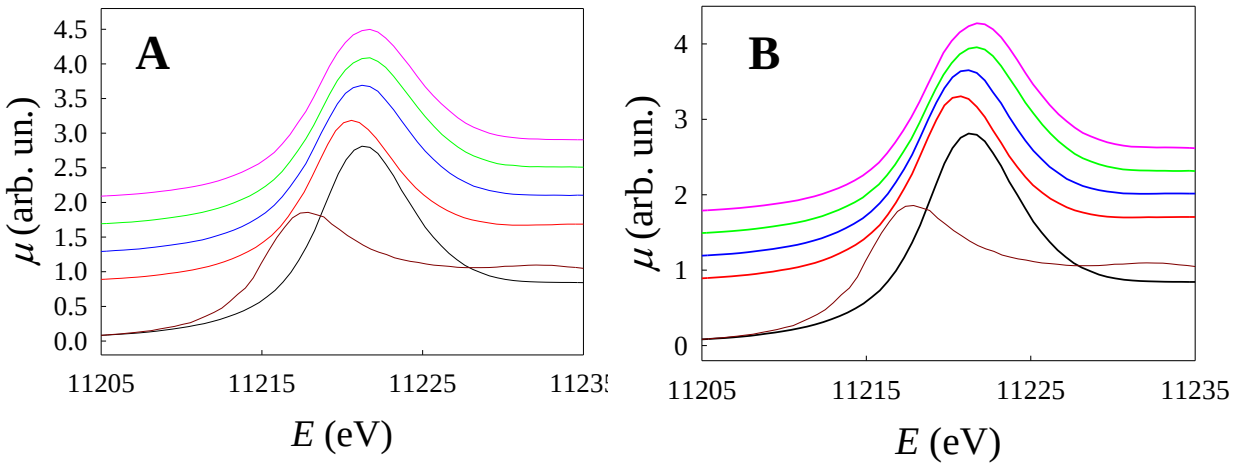

Figure 5.8. Ir L_{III} edge XANES spectra of el_1 (A) and el_2 (B). Spectra were acquired at 0.2 V (red line), 1.0 V (blue line), 1.3 V (green line), and 1.5 V (pink line). The brown line is the spectrum of metallic Ir, and the black line is the spectrum of bulk IrO_2, shown for reference.

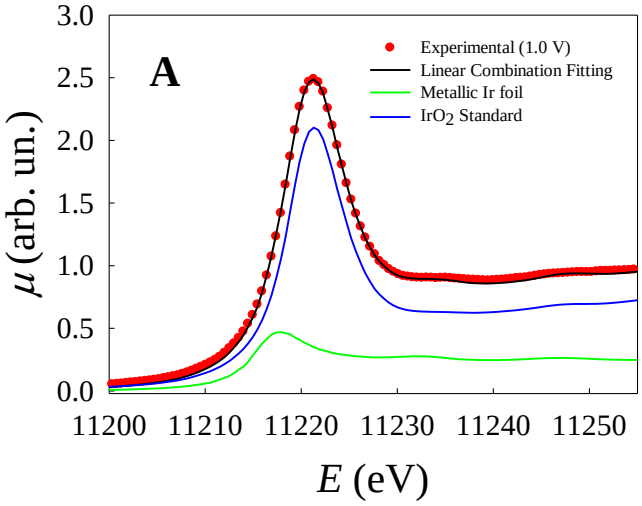

XANES spectra acquired at 1 V can be fitted as linear combinations of the spectra of metallic Ir and IrO_2 standard (Fig. 5.9) with weights 25 % and 75 % respectively that are in perfect agreement with those obtained by EXAFS. This result suggests that Ir and IrO_x shell do not interact: the presence of the metallic Ir core has no relevance on the catalytic mechanisms, which can be more effectively discussed

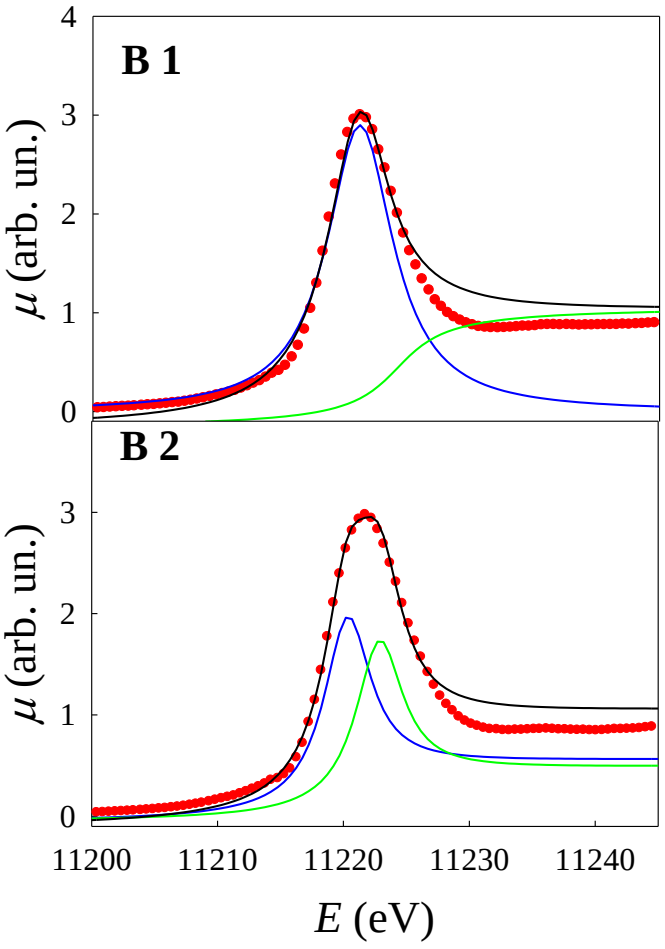

Figure 5.9. A) Fitting of XANES spectrum recorded at 1.0 V by means of a linear combination of Metallic Ir Standard (25 %) and IrO_2 standard (75 %) spectra. B) Fitting of XANES spectra after the subtraction of metallic iridium contribution for applied potential < 1.0 V (1) and for applied potential > 1.0 V (2).

analysing the difference spectra obtained as

$\mu_{sample} - \mu_{Metalli\ Ir} x\ 0.25.$

Normalized XANES spectra obtained from these differences, along with the corresponding second derivatives, are shown in Fig. 5.10. The main evidence is that the increase in the applied potential determines a shift of the WL to larger energy values (from 0.3 to 1.0 V) and a large increase in the FWHM (for applied potential larger than 1.0 V). So, this is in nice agreement with the results obtained for iridium oxide films, except that the crystal field splitting at 1.3 V was not observed. This can be explained with the assumption that in these materials the IrO_6 octahedra are more interacting. The XANES spectra obtained after the subtraction of Metallic Ir contribution were fitted with a proper combination of Lorentzian and arctangent functions (Fig. 5.9). This step allowed to access Ir oxidation states (Fig. 5.11) and therefore to demonstrate that for potentials larger than 1.3 V, both Ir(III) and Ir(V) are present.

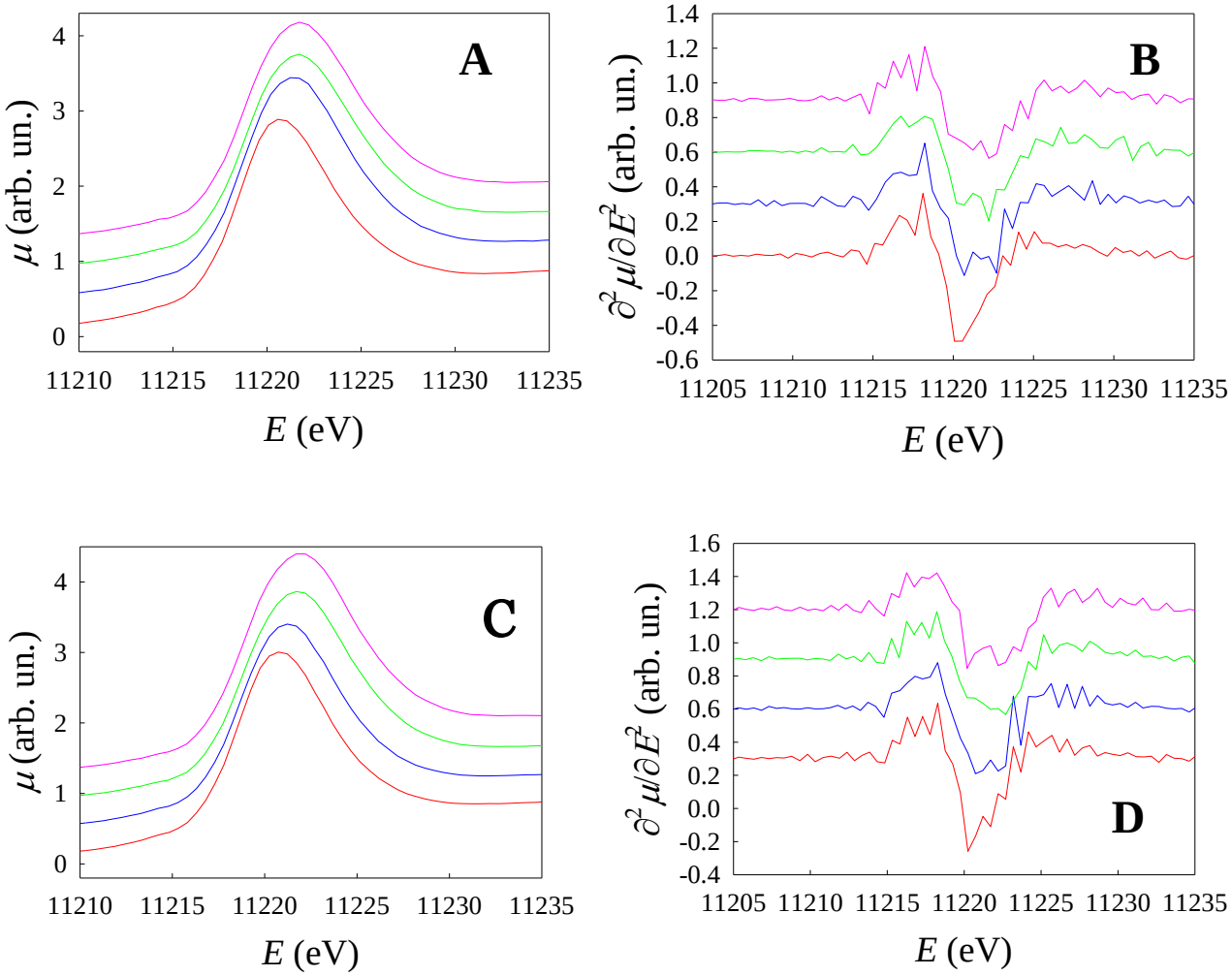

Figure 5.10. XANES spectra (A,C) and their second derivatives (B,D) of el_1 (A,B) and el_2 (C,D) after the subtraction of metallic iridium contribution. Spectra were acquired at 0.2 V (red line), 1.0 V (blue line), 1.3 V (green line) and 1.5 V (pink line).

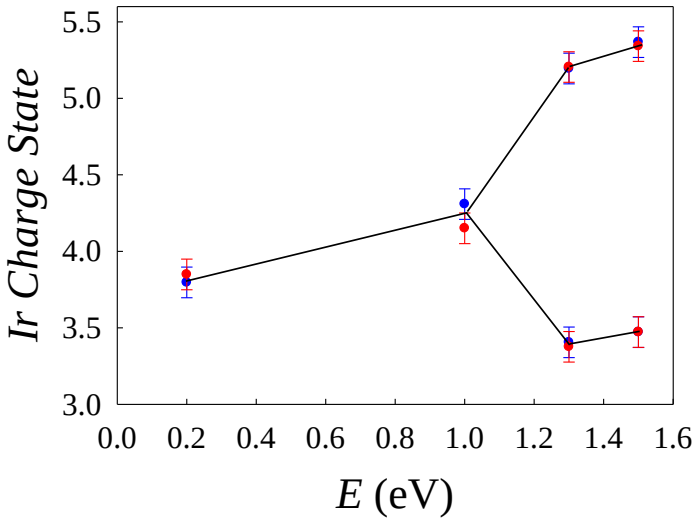

Figure 5.11. Ir oxidation state values obtained from the fitting of XANES spectra for el_1 (blue dots) and for el_2 (red dots).

On the basis of the results obtained it is possible to affirm that the catalytic cycle is present. Furthermore, we can conclude that the IrO_x/Ir ratio is not modified by the step of calcinations nor by the application of different potentials and the local environment of Ir does not change appreciably in oxygen evolution conditions.

5.3. Mechanism and Kinetics of Ion Diffusion in IrO_x in Different Chronoamperometric Conditions

When dealing with electro-catalytic systems, like EIROF samples, complications arise from the need of realizing a mounting, where the catalyst is deposited or chemically bound, and from the presence of an heterogeneous system (electrode/interface/electrolyte) which strongly influences the kinetics of the processes under investigation.

The current itself carries in principle the most important information on the kinetics of the electrochemical reaction. However, if the investigation is limited to current measurements, a severe limitation arises from non-faradic phenomena. As a consequence an independent determination is necessary in order to obtain reliable mechanistic insights.

The study of the variations in the oxidation state or in the local structure of Ir provides a very powerful tool to understand mechanistic insights lying under the electrochemical processes. One of the main downsides associated to XAS spectroscopy, is the time needed for the monochromator to scan over a desired energy range and to settle between movements. A strategy to overcome this limitation is represented by the so called QUICK-XAS[14] technique, in which the angle of the monochromator is continuously varied. This setup allows to acquire

a XAS spectrum in seconds or fractions of seconds. Nevertheless, the time resolution needed to investigate the kinetics and the mechanism of electrocatalytic systems is much higher. The achievement of a finer time resolution and highly focused beams (of dimensions of less than 20 μm) has become possible after the advent of the 3rd generation synchrotron radiation sources and the introduction of time-resolved-XAS experiments. In a Dispersive-XAS experiment the standard monochromator is replaced by a polychromator so that the sample is crossed by a polychromatic beam which is subsequently dispersed onto a detector (Fig. 5.12). This technique allows to acquire spectra with a time resolution up to less than a millisecond.

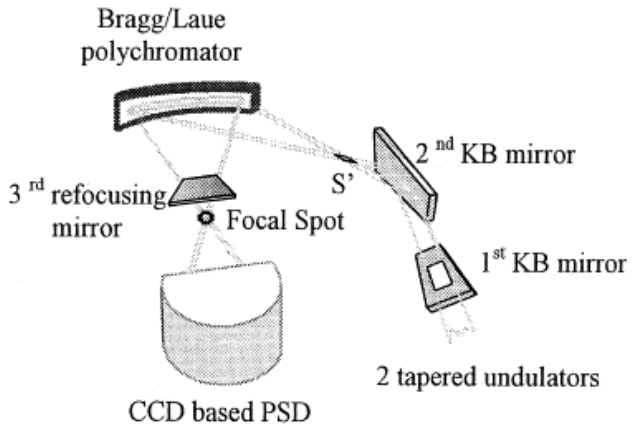

Figure 5.12. Scheme of a Dispersive-XAS setup.

The following part illustrates a dispersive-XAS experiment performed *in situ* on EIROF samples (Section 3.1.2) while applying specific chronoamperometric programs in order to shed light on the kinetics of processes involved.

5.3.1. BEAMLINE ID24 AND THE DISPERSIVE-XAS EXPERIMENT

Dispersive-XAS data were collected on ID24 beamline[15,16] at ESRF. The X-ray source consisted of two ondulators whose gaps were adjusted to tune constant counts of the first harmonic for energies around the Ir L_{III}-edge along the spectra. The beam was focused horizontally by a curved polychromator (Si 111) crystal in Bragg geometry and vertically with a bent Si mirror at a glancing angle of 2.5 mrad with respect to the direct beam. The beam size at the sample was 8 mm FWHM horizontally and 80 mm FWHM vertically in order to decrease the photon density in order to preserve the samples.

Spectra were recorded in transmission mode by means of a FreLonCCD camera detector[17]. The energy calibration was made by measuring the absorption spectrum of a Pt foil (Pt-L_{III}: 11564 eV; Ir-L_{III}: 11215 eV).

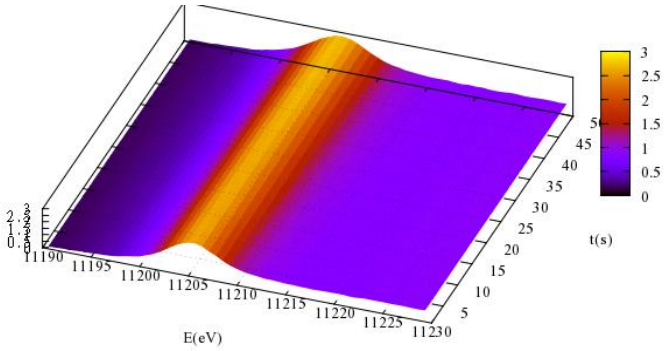

Figure 5.14. 3D graph showing an example of sequence of Dispersive- XAS spectra acquired the first 50 seconds.

Sequences of spectra (Fig. 5.13) were acquired while applying different chronoamperometrc programs corresponding to different potential jumps. Series of 10000 and 20000 spectra were acquired in 116 and 232 seconds respectively (each single spectrum is registered every 0.0116 s). Averages were

calculated every 10 spectra in order to obtain a better signal to noise ratio: this gives a final time resolution equal to 0.116 s. The experiment was repeated with two different kinds of electrolyte (0.5 M aqueous H_2SO_4 and 1 M aqueous NaOH) with the application of different potential steps, corresponding both to oxidation and reduction processes. Each step was carried out after a prolongued (≥ 180 s) of pre-conditioning at the initial condition (starting potential). The contour plots presented in Fig. 5.15 show data referred to the Ir(III) – Ir(IV) oxidation range both in acidic and in alkaline medium.

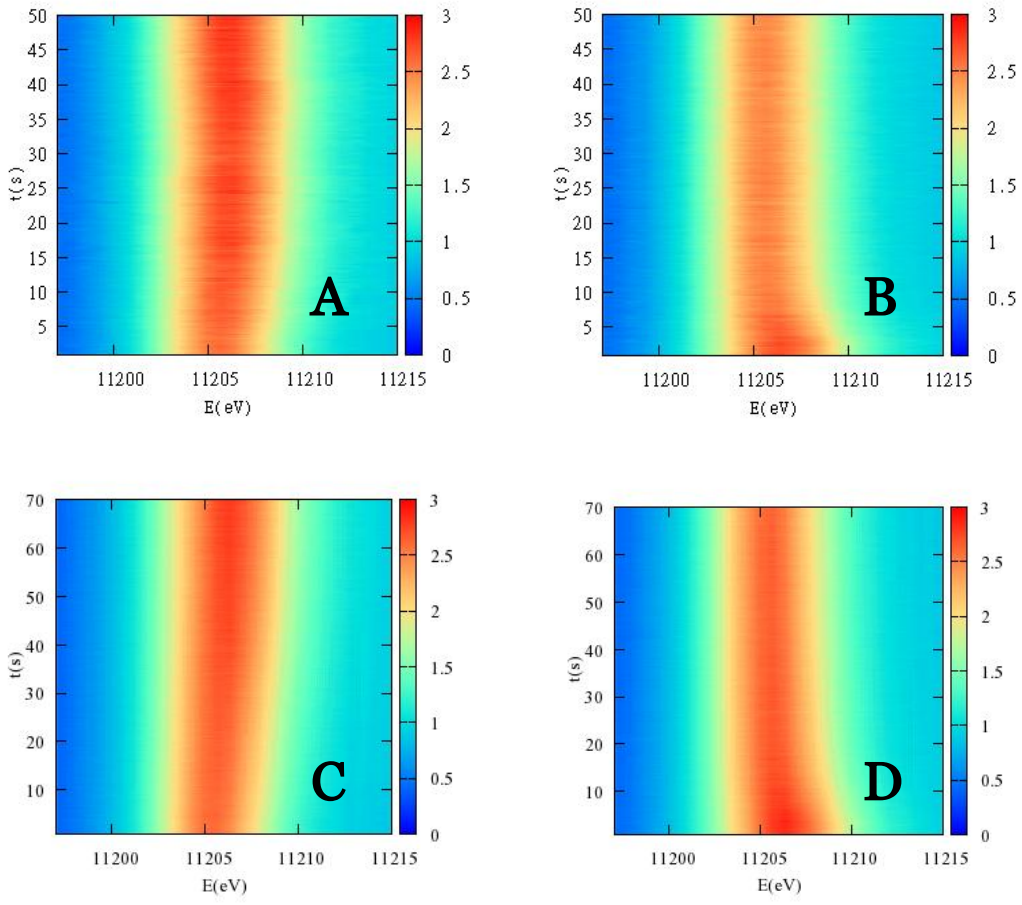

Figure 5.15. 2D maps showing data referred to the Ir(III) -- Ir(IV) oxidation range for both the acidic (A,B) and alkaline (C,D) medium. The potential steps applied are 0.2 → 1.05 V (A), 1.05 → 0.2 V (B), 0.2 → 0.9 V (C) and 0.9 → 0.2 V (D). The maps refer to the first 50 s.

At first sight we note variations both in the position and the width of the white line (enlargement and shift towards larger energy values for the oxidation, narrowing and shift to lower energy values for the reduction). Ir(III) – Ir(IV) oxidation range was not the only one investigated: as for example, Fig. 5.16 shows two contour plots obtained applying larger potentials, where Ir(V) is expected to appear.

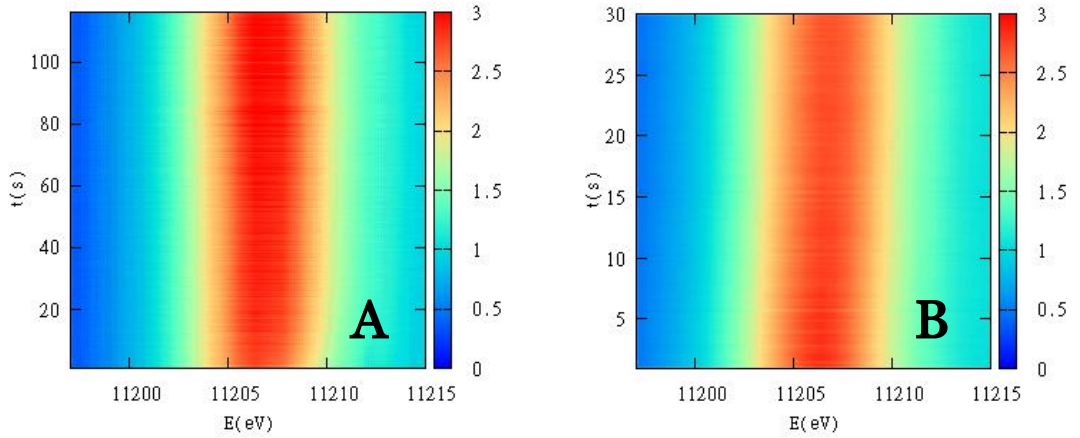

Figure 5.16. 2D maps showing data referred to the Ir(IV) -- Ir(V) oxidation range for both the acidic (A) and alkaline (B) medium. The potential steps applied are 1.05 → 1.3 V and 0.9 → 1.4 V respectively. The sequence of spectra obtained with alkaline medium is shown for the first 30 s.

The potential steps were triggered by the spectra acquisition system through the trigger option of the potentiostat (a CH Instrument 630D). The choice of potential steps to be applied was made on the basis of cyclic voltammetry (CV) runs recorded in acidic media on the same electrodes (Fig. 5.17).

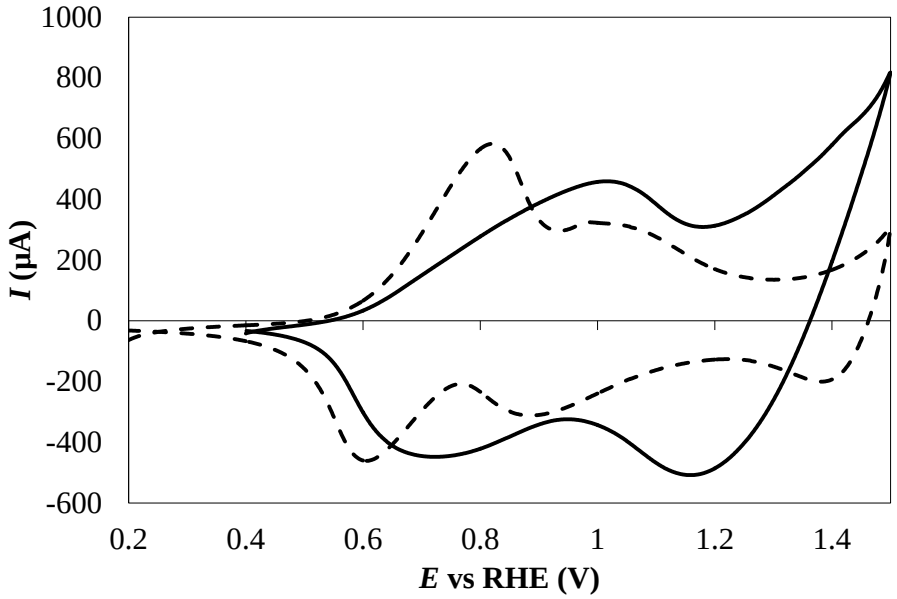

Figure 5.17. CV for IrO_x recorded at 2 mV/s in 0.5 M H_2SO_4 (full line) and CV for IrO_x recorded at 2 mV/s in 1 M NaOH (dashed line).

The manually-built spectroelectrochemical cell is made of PTFE and contains a Pt foil counter-electrode and a reference electrode (AgCl/Ag in 0.1 M KCl). All measurements were carried out at room temperature.

5.3.2. DATA PROCESSING AND ANALYSIS

Data processing consisted of four steps: *(i)* preliminary analysis that includes the normalization procedure and the extraction of XAFS signal, *(ii)* fit of dispersive-EXAFS signals in order to monitor possible variations in the local surrounding, *(iii)* fit of the XANES spectra to get the parameters for characterizing the time dependence of the process and *(iv)* assessment of a kinetic law from the time evaluation of the *DoR* (Degree Of Reaction) along the sequence.

EXAFS data extraction, carried out by means of PRESTOPRONTO software[18], began with the evaluation a *pre-edge* and a *post-edge* baseline function (Fig. 5.

18) that were then applied to the row signal. The first function reproduces additional excitations of the photo-absorber or possible excitations of any other element present ($\mu_n x$) and was modeled with a straight line obtained by interpolating the *pre-edge* data, and then extrapolated to the after-edge signal. The latter function represents the absorption profile due to an isolated photo-absorber (indicated as $\mu_0(E)$) and was modeled with a 3rd order spline using first point of inflection as E_o. The interval for the pre-edge fitting, E_o, and the interval for the post-edge fitting employed were the same for an entire sequence of measurements but only some representative spectra were chosen for the subsequent EXAFS analysis and fitting.

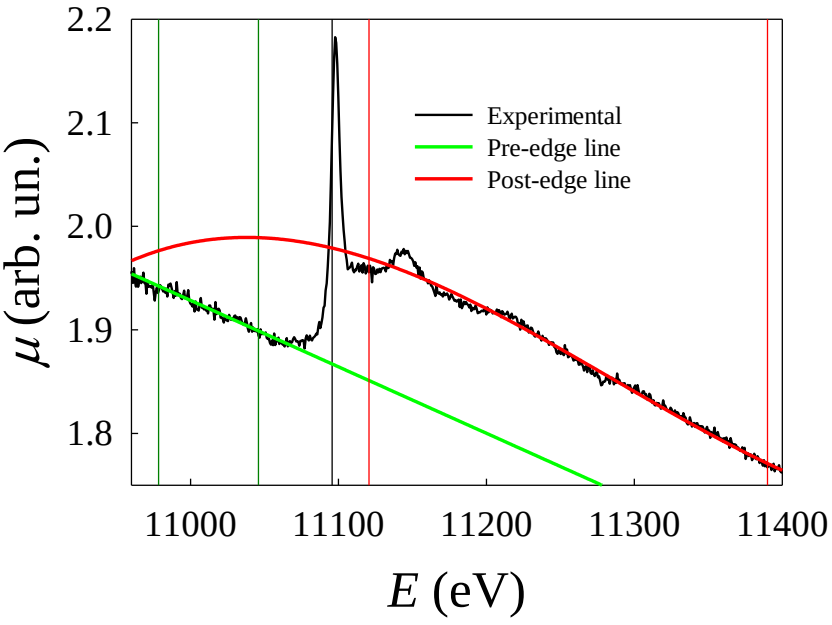

Figure 5.18. EXAFS signal extraction: the experimental XAS spectrum is the black line, the *pre-edge* function is represented as a green line, the *post-edge* function is represented as a red line.

The extracted EXAFS signal was then fitted to an appropriate structural model with the EXCURVE code[19]. The calculation of the atomic scattering parameters (phases and amplitudes) were based on the muffin-tin approximation, in the framework of the Hedin-Lundquist and Von Bart approximations for the

exchange and ground state potentials, respectively[19]. This includes the effects of losses due to the electron inelastic scattering. The fittings were made in the k space, using a k^2 weighting scheme and full multiple scattering calculation within the assumed clusters. As goodness of fit (GOF) we used the F-factor:

$$F = 100 \sum_{i}^{N} \frac{\left[\chi_{i,exp} - \chi_{i,calc}\right]^2}{\sigma_i} \tag{5,2}$$

The XANES fitting stage was performed by a linear combination of one arctangent and one Lorentzian function for each spectrum of a sequence (Fig. 5.19). This step of data analysis was carried out automatically by means of MINUIT program[20], a well-known tool for function minimization and error analysis, writing a subroutine for a multi-parameter function to be optimized. This is the χ^2 of the fit of the experimental data $y_{exp,i}$ to the model:

$$\sum_i \left\{ y_{exp,i} - \frac{I}{\left(1 - \left[\frac{(x_i - x_0)}{b}\right]^2\right)} - g\left[\frac{1}{2} + \frac{1}{\pi}\arctan\left(\frac{x_i - x_1}{h}\right)\right] \right\}^2 \tag{5,3}$$

where x_0 is the Lorentzian position, b the Lorentzian width, I the Lorentzian intensity, x_1 the arctangent position, h the arctangent width, g the arctangent intensity, and the index i runs over all energy scan steps of a single spectrum. To explore the parameter space and to gain assurance that the real minimum has been reached, we employed a preliminary Monte Carlo search, as the Minuit package features a Metropolis algorithm for jumping out of a previous minimum through function barriers. As a rule, 3 x 10^6 Monte Carlo steps were applied to some selected spectra of a sequence. The consistency of these results

was checked along the whole data set, and finally they were used as starting values of the parameters for the final fits of all spectra of the sequence. The refined fits were done using a combination of a simplex minimization followed by a variable-metric gradient method[22], which also determines the parabolic errors. As an example, Fig. 19.B illustrates a series of measurements performed in acidic medium and with the potential jump 0.2 → 1.05 V. After the application of the potential step, the WLs of the spectra move towards larger energy values, thus indicating an overall oxidation from Ir(III) to Ir(IV), and show an increase in the FWHM. The time dependence of these features can be monitored thanks to the parameters obtained by the XANES fitting procedure.

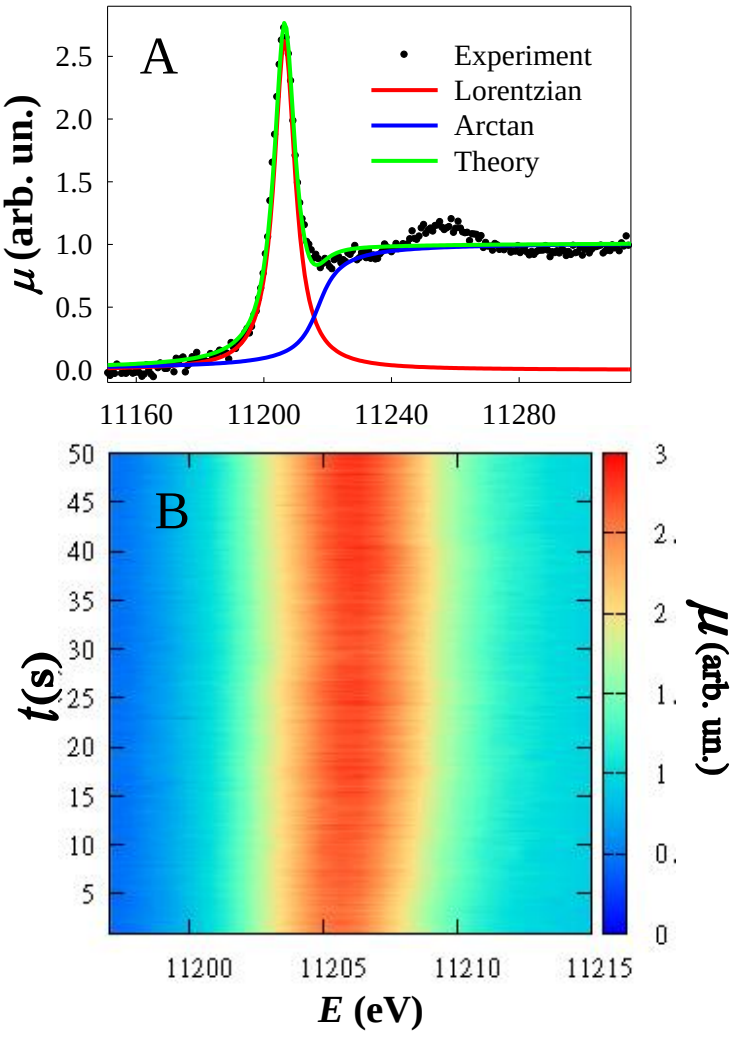

Figure 5.19. XAS at the Ir-L_{III} edge. A): raw spectrum and fit according to the model described in the text. B): time evolution of the spectra. This sequence is referred to an oxidation process from Ir(III) to Ir(IV) and is shown for the first 50 s.

For each parameter (here indicated by x) showing a sensible variation with time, a *DoR* (ξ) can be calculated from the set of values along the whole sequence according to the equation:

$$\xi = \frac{[x - x_i]}{[x_f - x_i]} \tag{5,4}$$

where x is the parameter value at current time t, x_i is the parameter value at the initial time t_i, and x_f is the parameter value at the final time t_f. The most suitable parameters for the determination of the *DoR* are the Lorentzian position (x_o in Eq. (5,3)) and the Lorentzian width (b in eEq. (5,3)).

The overall procedure for extracting a *DoR* from the features of a XAS spectrum has been selected particularly for its simplicity and ease of implementation on sequences of a large number of spectra. Before its routine application to the whole set of experimental data, its reliability has been assessed by the excellent agreement with the *DoR* obtained on random sets of XAS spectra using the more conventional approach based on the best fit of a linear combination of suitably selected initial and final spectra.

The final step of data analysis deals with the estimation of a kinetic law and of its underlying coefficients.

5.3.3. DISPERSIVE-XAS RESULTS OBTAINED

EXAFS fitting procedure was carried out only for some selected spectra of an entire sequence, in order to gain structural information about the initial and final stages of the process and some intermediate advancement degrees. Fig.

5.20 shows the IrO_x film response during the application of the electrochemical program corresponding to the oxidation process from Ir(III) to Ir(IV) in acidic (A,B) and in basic (C,D) medium. In the former case the potential jump applied is 0.2 –> 1.05 V and in the latter the potential jump is 0.2 → 0.9 V. The EXAFS spectra illustrated (with the corresponding FTs) are separated by time intervals of ca. 6 s within the first 40 s, when the chronoamperometric signal shows zero current thus indicating that the oxidation process is concluded. Fig 5.18 shows that EXAFS oscillations are well visible up to 8 $Å^{-1}$: this allows the structural characterization up to the second shell. The similarity that can be observed between the spectra at different times clearly demonstrates that local structure, at least within the first two shells, is maintained during the reaction. Furthermore, a comparison with the signal of the standard (black lines) is a clear demonstration that the local structure of Ir is very similar to that present in rutile-type IrO_2 both in acidic and basic medium. The peak in the FT situated at 1.5 Å is due to the 6 O atoms in the rutile structure. The peaks between 3.4 and 3.8 Å are mainly due to Ir and O atoms that are the Next Nearest Neighbors (NNN) around Ir of IrO_2. We should remember that the beginning of the reaction Ir is present as Ir(III), and this experimental evidence demonstrated the flexibility of the EIROF matrix in accommodating different oxidation states.

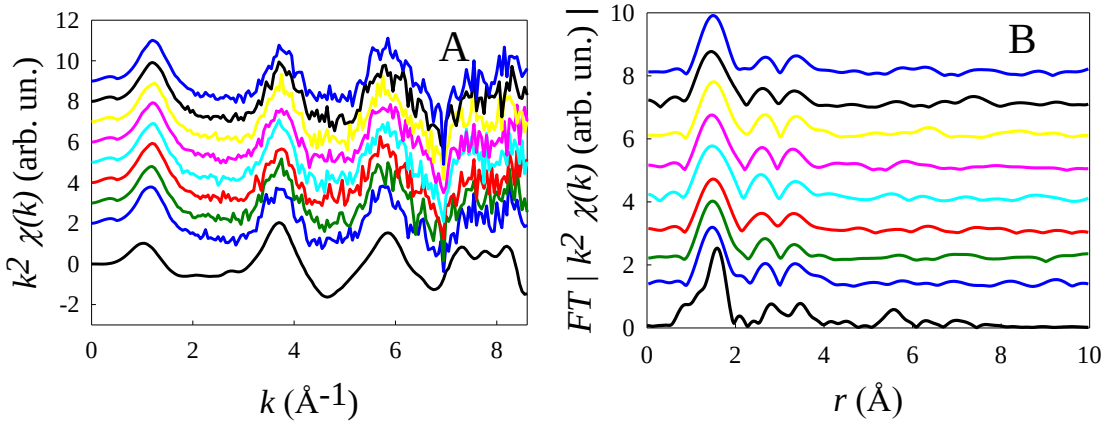

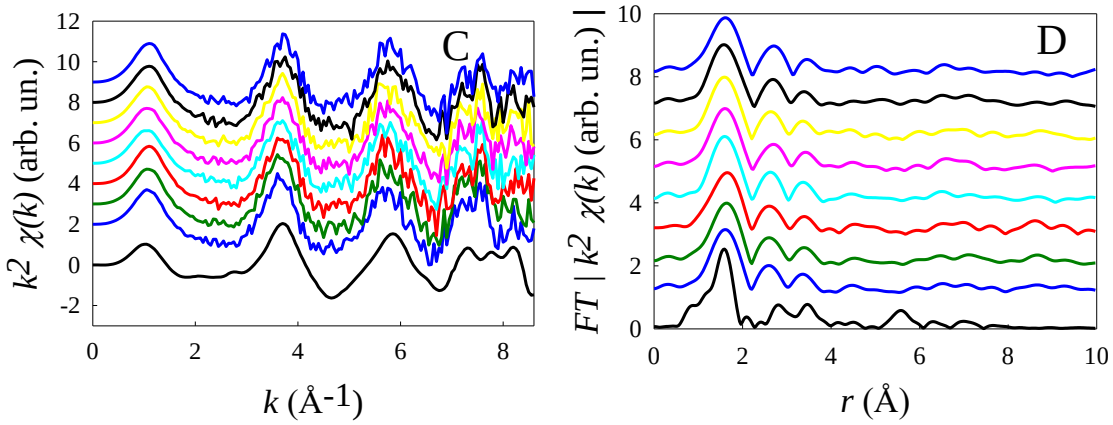

Figure 5.20. EXAFS (A, C) and FT (B, D) spectra of sequences recorded within the first 40 seconds illustrated from the bottom to the top, separated by a time interval of ca. 6 seconds. The IrO_2 standard EXAFS and FT signals are represented as black lines. A, B: measurements were carried out in acidic medium for the potential step 0.2–1.05 V. C, D: measurements were carried out in basic medium for the potential step 0.2-0.9 V.

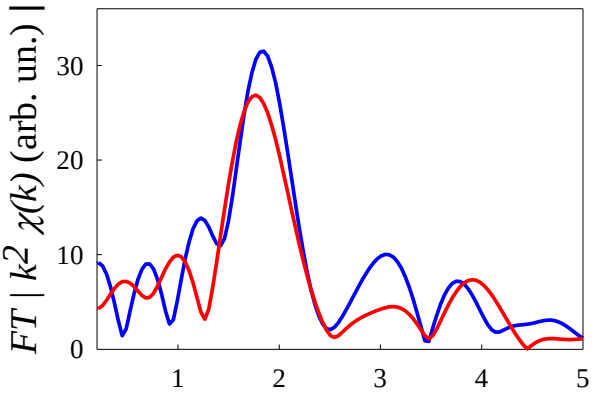

Figure 5.21. Comparison of the first peak of the FTs recorded in acidic medium (red line) and in alkaline medium (blue line).

Interestingly, if we compare the FTs of the spectra acquired in acidic and basic media (Fig. 5.21), a difference in the first coordination peak can be detected. The signal acquired in acidic medium, indicated by a red line, is characterized by an additional shoulder towards lower distance values. The results clearly accounts for the presence of a smaller Ir—O bond distance. By comparison, the blue line, which represents the measurements in basic medium, is marked by a narrower peak for the first coordination shell with a maximum situated at larger distances. The only reasonable explanation to this feature is the presence of six equal Ir—O bond distances. This effect can be better investigated and quantified by fitting the EXAFS signal with a structural model based on rutile-type IrO_2 as suggested by the experimental evidence. As far as the acidic medium is concerned, the fit model consists of iridium in a compressed octahedral site, in which two axial

oxygen atoms are placed at a shorter distance than the equatorial ones. The third shell consists of four oxygen atoms and the fourth one consists of four oxygen atoms. The fitting was performed employing full multiple scattering calculations and the exact curve wave theory. The best fit results are shown in Fig. 5.22 A and B as red lines while the experimental data are indicated by the black lines.

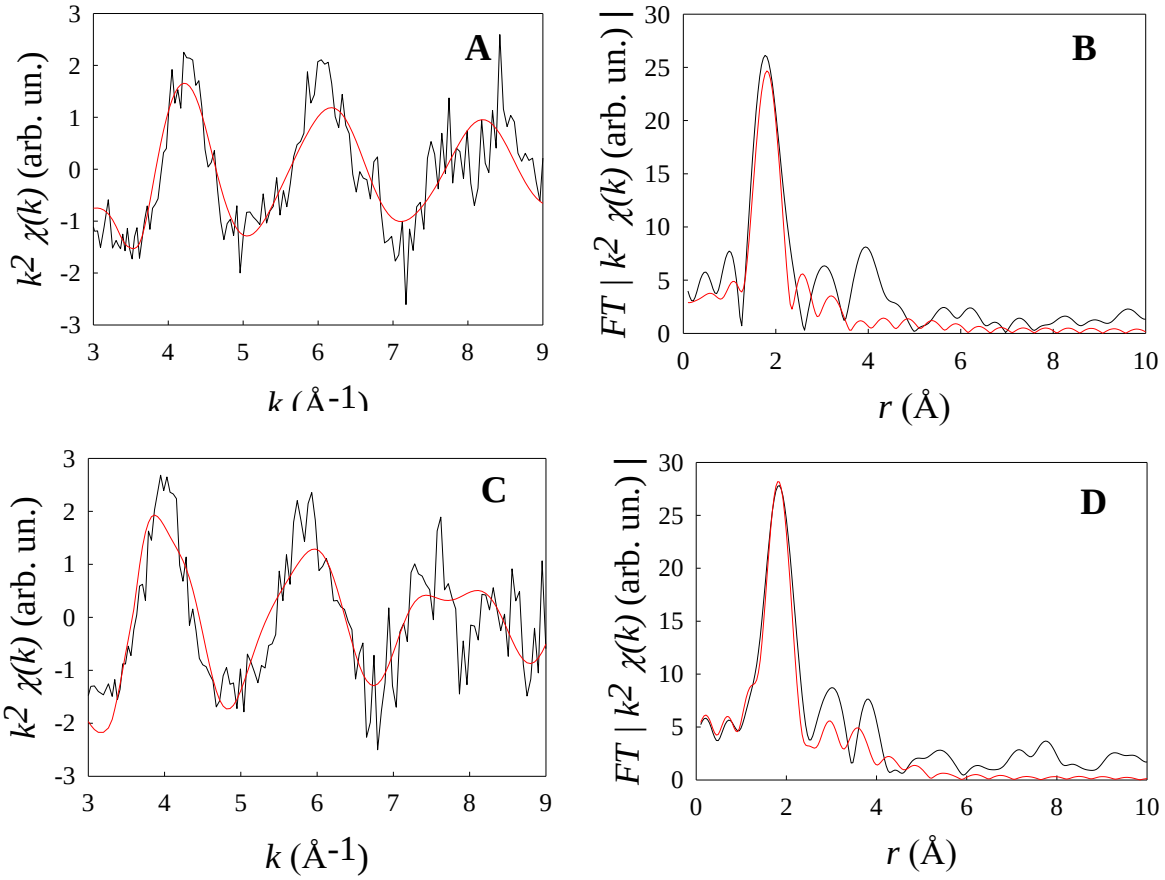

Figure 5.22. Fitting of EXAFS (A) and relative FT (B) spectra in acidic and (C and D) basic medium. The experiment is the black line whereas the theory is represented as a red line.

Tab. 5.2 illustrates the parameters obtained by the fitting procedure for the different reaction times (*i.e.* after 0.23, 5.2, 10.0, and 34.8 s) and the distance parameters found in literature according to crystallographic information (r^*)[21]. The distance of the second and the third shell were kept constant and equal to the crystallographic values in order to avoid correlation due to a too large ratio

of number of parameters to number of data; however, it is worth mentioning that the addition of these further shells is needed to obtain a good fit. In all cases, the goodness of fit values (*F*) obtained are between ca. 25 and ca. 30 %. This is a good value, given the unavoidable noise affecting the spectra.

0.23 s						**5.2 s**					
Shell	***N***	**Atom**	***r* (Å)**	**σ^2(Å^2)**	***r*(Å)***	**Shell**	***N***	**Atom**	***r* (Å)**	**σ^2(Å^2)**	***r*(Å)***
1	2	O	1.64(7)	$3(2)*10^{-2}$	1.943	1	2	O	1.65(9)	$3(3)*10^{-2}$	1.943
2	4	O	1.88(2)	$0(1)*10^{-3}$	1.980	2	4	O	1.89(3)	$0(2)*10^{-3}$	1.980
3	2	Ir	3.110	$3(9)*10^{-2}$	3.110	3	2	Ir	3.110	$2(9)*10^{-2}$	3.110
4	4	O	3.406	$1(2)*10^{-2}$	3.406	4	4	O	3.406	$1(2)*10^{-2}$	3.406
F=27.8 %						*F*=32.4 %					
10.0 s						**34.8 s**					
Shell	***N***	**Atom**	***r* (Å)**	**σ^2(Å^2)**	***r*(Å)***	**Shell**	***N***	**Atom**	***r* (Å)**	**σ^2(Å^2)**	***r*(Å)***
1	2	O	1.70(9)	$4(3)*10^{-2}$	1.943	1	2	O	1.70(9)	$4(3)*10^{-2}$	1.943
2	4	O	1.91(2)	$0(2)*10^{-3}$	1.980	2	4	O	1.90(2)	$1(2)*10^{-3}$	1.980
3	2	Ir	3.110	$0(1)*10^{-2}$	3.110	3	2	Ir	3.110	$1(2)*10^{-2}$	3.110
4	4	O	3.406	$1(2)*10^{-2}$	3.406	4	4	O	3.406	$1(3)*10^{-2}$	3.406
F= 24.3 %						*F*= 26.0 %					

Table 5.2. EXAFS fitting parameters obtained for spectra acquired at 0.23, 5.2, 10.0 and 34.8 s in acidic medium; *r*: distances; σ^2: distance variances; *r*:* crystallographic values; The coordination numbers *N* have been kept constant to their crystallographic values.

On the basis of previous assumptions, the spectra recorded in basic medium were fitted using a model consisting of a first coordination shell of six oxygen atoms in an exactly octahedral arrangement (Tab. 5.3). The first comment concerns the negative trend of the first Ir—O distances with time, as we can expect for an oxidation process from Ir(III) to Ir(IV). The distances obtained for the sample at the last time are markedly close to the mean value of the crystallographic distances for IrO_2. Furthermore, at all times the distances are significantly larger than those obtained for the sample in acidic medium. Finally, the goodness of Fit values (*F*) referred to this case are smaller than 30 %, thus supporting the inference of a perfect octahedral arrangement of oxygen atoms in the first coordination shell. A reasonable explanation to this structural

different between acidic and alkaline medium can be the protonation of the two axial oxygen atoms in acidic medium.

0.23 s						**5.2 s**					
Shell	**N**	**Atom**	***r* (Å)**	**s^2(Å^2)**	***r*(Å)***	**Shell**	**N**	**Atom**	***r* (Å)**	**s^2(Å^2)**	***r*(Å)***
1	2	O	2.00(2)	$5(2)*10^{-3}$	1.943	1	2	O	1.98(2)	$5(2)*10^{-3}$	1.943
2	4	O	2.00(2)	$5(2)*10^{-3}$	1.980	2	4	O	1.98(2)	$5(2)*10^{-3}$	1.980
3	2	Ir	3.110	$1(9)*10^{-3}$	3.110	3	2	Ir	3.110	$1(8)*10^{-3}$	3.110
4	4	O	3.406	$1(2)*10^{-2}$	3.406	4	4	O	3.406	$1(3)*10^{-2}$	3.406
F=25.9 %						*F*=26.3 %					
10.0 s						**34.8 s**					
Shell	**N**	**Atom**	***r* (Å)**	**s^2(Å^2)**	***r*(Å)***	**Shell**	**N**	**Atom**	***r* (Å)**	**s^2(Å^2)**	***r*(Å)***
1	2	O	1.97(2)	$5(2)*10^{-3}$	1.943	1	2	O	1.96(2)	$3(2)*10^{-3}$	1.943
2	4	O	1.97(2)	$5(2)*10^{-3}$	1.980	2	4	O	1.96(2)	$3(2)*10^{-3}$	1.980
3	2	Ir	3.110	$0(9)*10^{-3}$	3.110	3	2	Ir	3.110	$0(8)*10^{-3}$	3.110
4	4	O	3.406	$1(2)*10^{-2}$	3.406	4	4	O	3.406	$0(2)*10^{-2}$	3.406
F= 26.7 %						*F*= 23.5 %					

Table 5.3. EXAFS fitting parameters obtained for spectra acquired at 0.23, 5.2, 10.0 and 34.8 s in alkaline medium; *r*: distances; σ^2: distance variances; *r*:* crystallographic values; The coordination numbers *N* have been kept constant to their crystallographic values.

Let's now consider the results obtained from the XANES fitting procedure, aimed at studying the time dependence of the oxidation/reduction process of Ir in order to assess a kinetic law.

Both the Lorentzian position (x_0) and amplitude (b) show a sensible variation with time and therefore they can be used to calculate the Degree of Reaction according to Eq. (5,4). An example of the overall time evolution of these parameters is displayed in Fig. 5.23.A and in Fig. 5.23.B respectively.

The parabolic trend observed is a clear indication that the process is under diffusion control. It is important to underline that the trend of the Lorentzian position shows a lower noise and is definitely more reliable: the typical variation between the first and the last spectrum is ca. 1 eV while the spectrum-to-spectrum reproducibility is ca. 0.02 eV. As a matter of fact, we consider this assessment valid for all the XAS measurements and therefore only this

parameter will be discussed later on. Fig. 5.23 shows the results obtained from the XANES fitting of a sequence of spectra corresponding to the oxidation process from Ir(III) to Ir(IV). In this case the potential jump applied is 0.2 → 1.05 V.

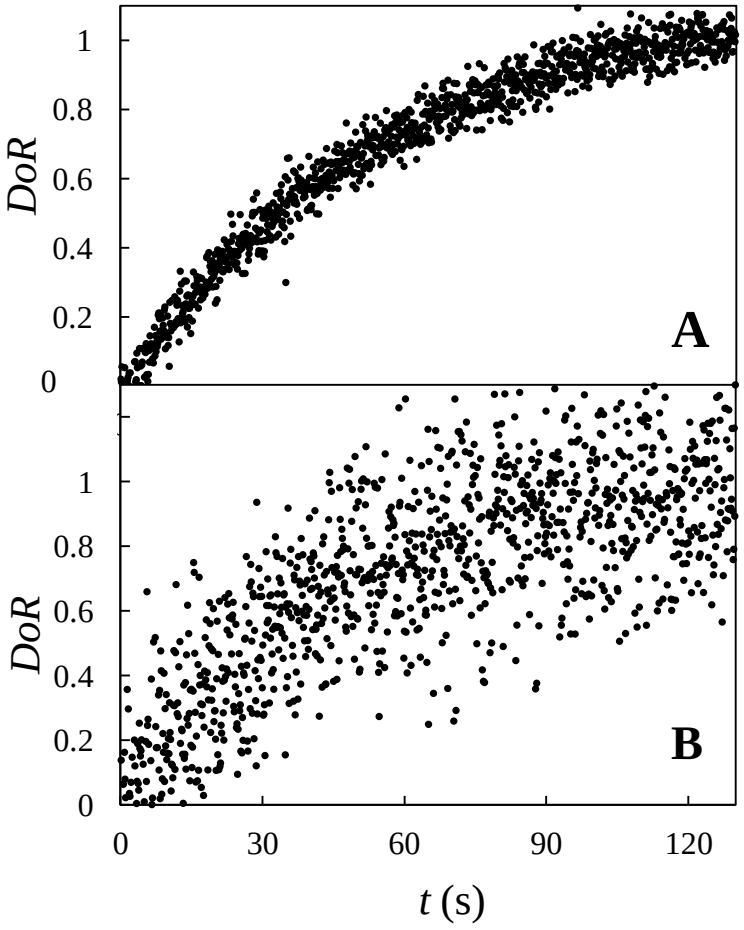

Figure 5.23. Fitting results for the sequence of spectra corresponding to the oxidation process from Ir(III) to Ir(IV) in acidic medium A): time evolution of the *DoR* obtained from the energy of the Lorentzian component. B): time evolution of the *DoR* obtained from the width of the Lorentzian component.

Fig. 5.24 shows examples of *DoRs* obtained in the experiment carried out in acidic medium for different potential steps. It is important to underline that for each potential step the measurements was performed more than once in order to check for the reproducibility of the results.

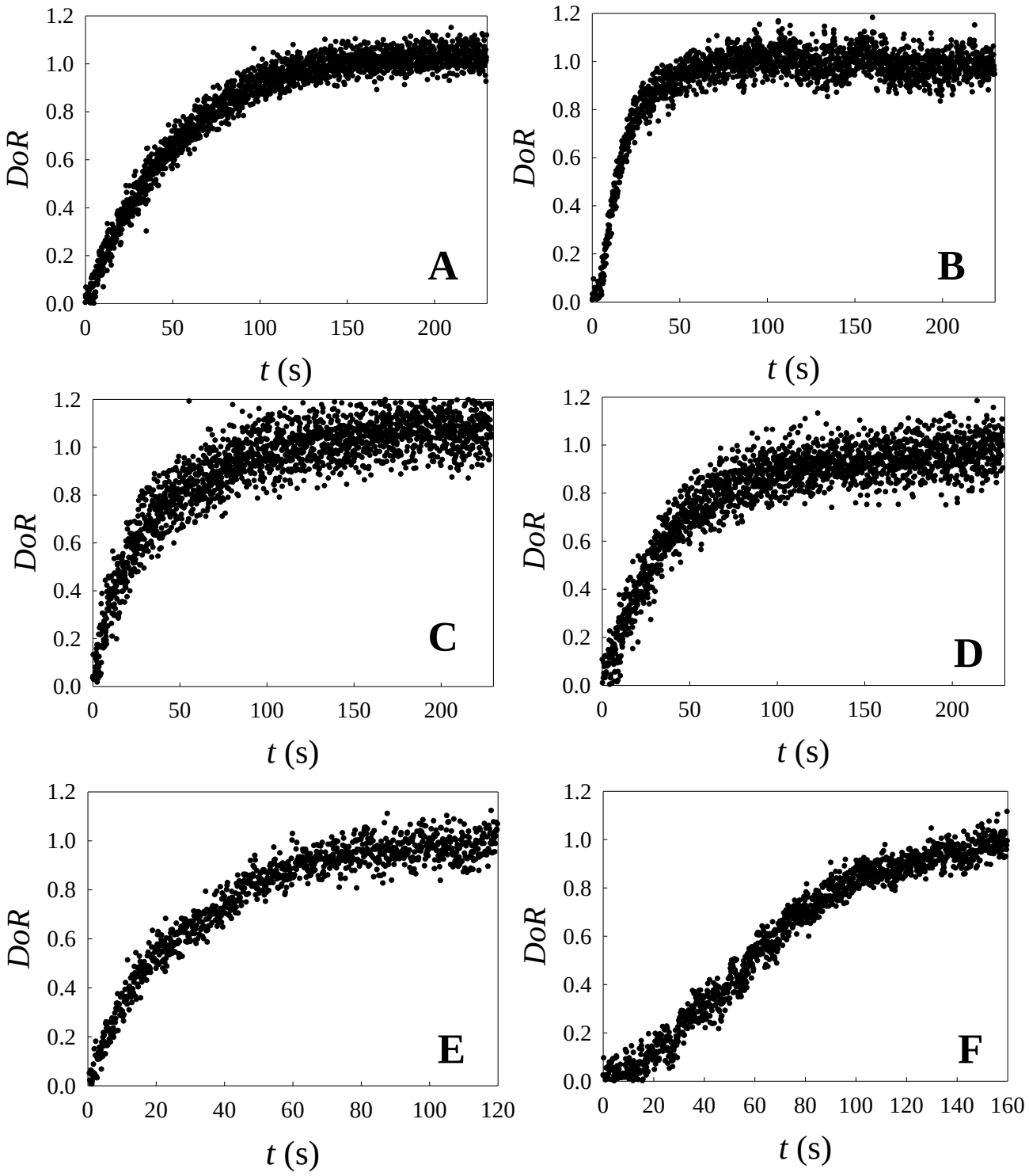

Figure 5.24. Examples of fitting results for sequences of spectra obtained in acidic medium applying the potential steps 0.2 → 1.05 V (A), 1.05 → 0.2 V (B), 1.05 → 1.3 V (C), 1.3 → 1.05 V (D), 1.05 → 1.5 V (E), 1.5 → 1.05 V (F). The investigation of the *DoRs* was made according to the energy of the Lorentzian function.

Fig. 5.25 illustrates XANES results referred to some data sets obtained in presence of alkaline medium as electrolyte.

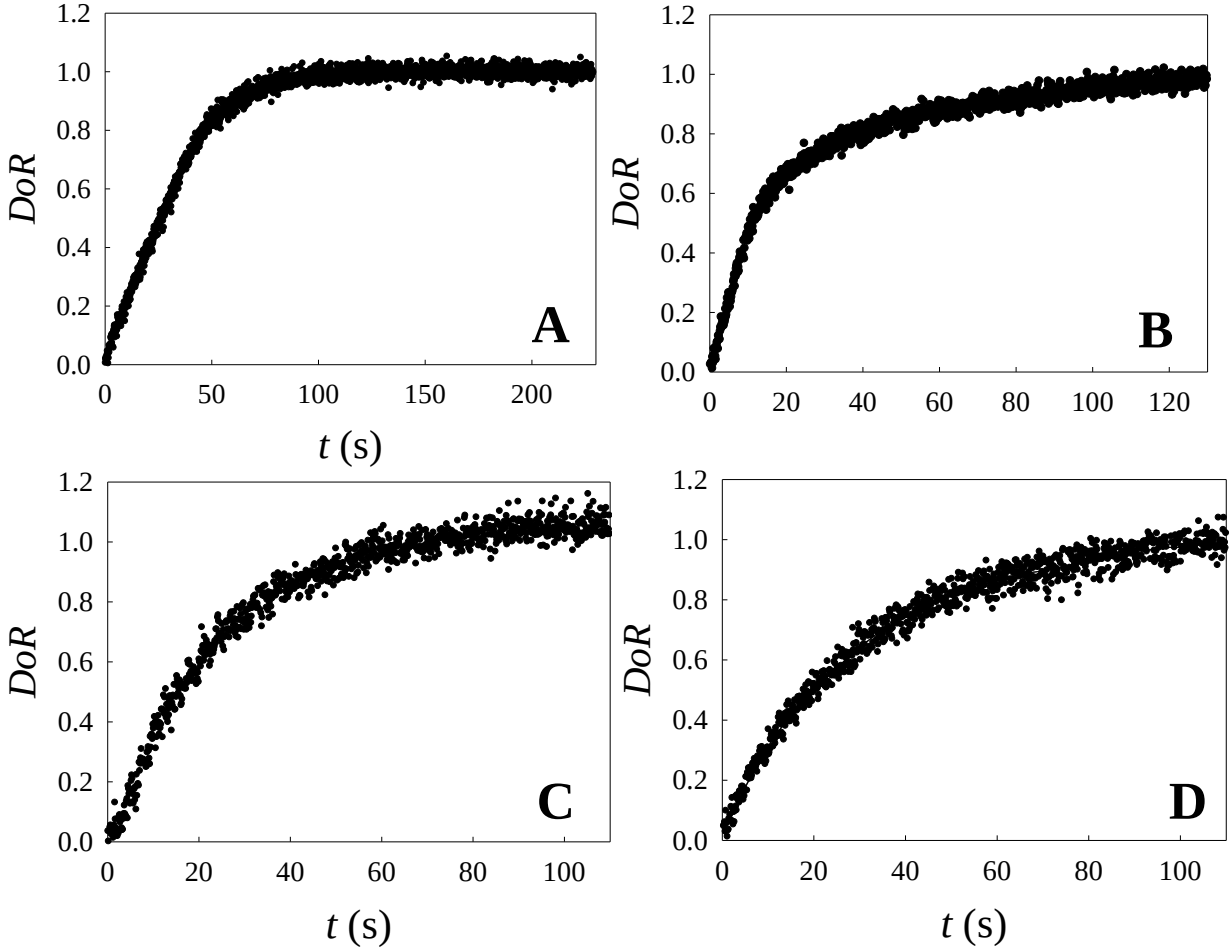

Figure 5.25. Examples of fitting results for sequences of spectra obtained in alkaline medium applying the potential steps 0.2 → 0.9 V (A), 0.9 → 0.2 V (B), 0.9 → 1.2 V (C), 1.2 → 0.9 (D). The investigation of the *DoRs* was made according to the energy of the Lorentzian function.

Only sequences of spectra acquired in acidic medium will be discussed in this part since we do not have identified yet a model to interpret XANES data obtained in alkaline medium.

The common understanding for the redox process involving the IrO_x material is that the rate determining step of the reaction is the diffusion of H^+ ions in the electrodic moiety. Thus from the fitting results it is possible to obtain the diffusion coefficient of H^+.

Taking into account that the system under investigation is mono-dimensional, the second Fick's law is:

$$\frac{\partial n}{\delta t} = D\frac{\delta^2 n}{\delta x^2} \tag{5,5}$$

where n is the concentration (amount of substance/length[3]), D diffusion coefficient, t time and x is the position inside the electrode with respect to one of the surfaces. The system under investigation can be described by a 1D model based on a porous electrode layer with depth L enclosed between a metal body and a buffered pool of liquid electrolyte, which acts as an unlimited source of the diffusing species (H^+) at a constant concentration (Fig. 5.26).

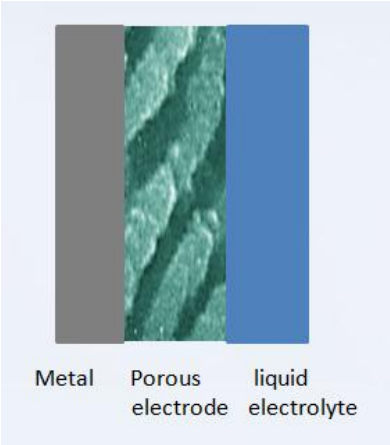

Figure 5.26. 1D model suggested for the systems under investigation.

If we take into account the pertinent boundary conditions, an approximate solution of the Fick's Law is[23]:

$$\frac{q(t)}{q_s} = 1 - \frac{8}{\pi^2}\sum_{n=0}^{\infty}\frac{1}{(2n+1)^2}e^{\frac{-(2n+1)^2\pi^2 Dt}{L^2}} \tag{5,6}$$

where $q(t)$ is the total amount that has entered the layer at time t, while q_s is the corresponding quantity at long times. Eq. 5,6 can be considered as an advancement degree and is suitable to comparison with experiments. Thus, the asymptotic expression is:

$$\frac{q(t)}{q_s} = 1 - \frac{8}{\pi^2} e^{-\frac{\pi^2 Dt}{L^2}} \tag{5,7}$$

It is easy to demonstrate that Eq. 5,7 gives a linear plot of $ln\left[1 - \left(\frac{q}{q_s}\right)\right]$ vs *t*. Taking into account that $\left(\frac{q}{q_s}\right)$ represents the *DoR*, we obtain:

$$\ln(1 - DoR) = ln\frac{8}{\pi^2} - \frac{\pi^2 Dt}{L^2} \tag{5,8}$$

The value of the diffusion coefficient can be easily obtained from the slope by:

$$D = -\frac{L^2 slope}{\pi^2} \tag{5,9}$$

where *L* is the thickness of the electrode, which can be estimated from the density by using the Lambert-Beer equation.

With this in mind it is possible to examine in more detail the results obtained for the reduction process from Ir(IV) to Ir(III) and the oxidation reaction from Ir(III) to Ir(IV). As described above, two independent measurements are in principle available to calculate the *DoR*: *i)* the position of the Lorentzian peaks used in the XANES fitting; and *ii)* the integral of the current under the experimental conditions. It is important to note that in absence of non-faradic phenomena, a correlation plot of the *DoR* obtained by XAS investigation vs the *DoR* obtained by the integral of the current should lie on the diagonal of the first quadrans. Such a plot is shown for the reduction and the oxidation in Fig. 5.27.A

and 5.27.B respectively: in both cases we note a good agreement between spectroscopy and electrochemistry.

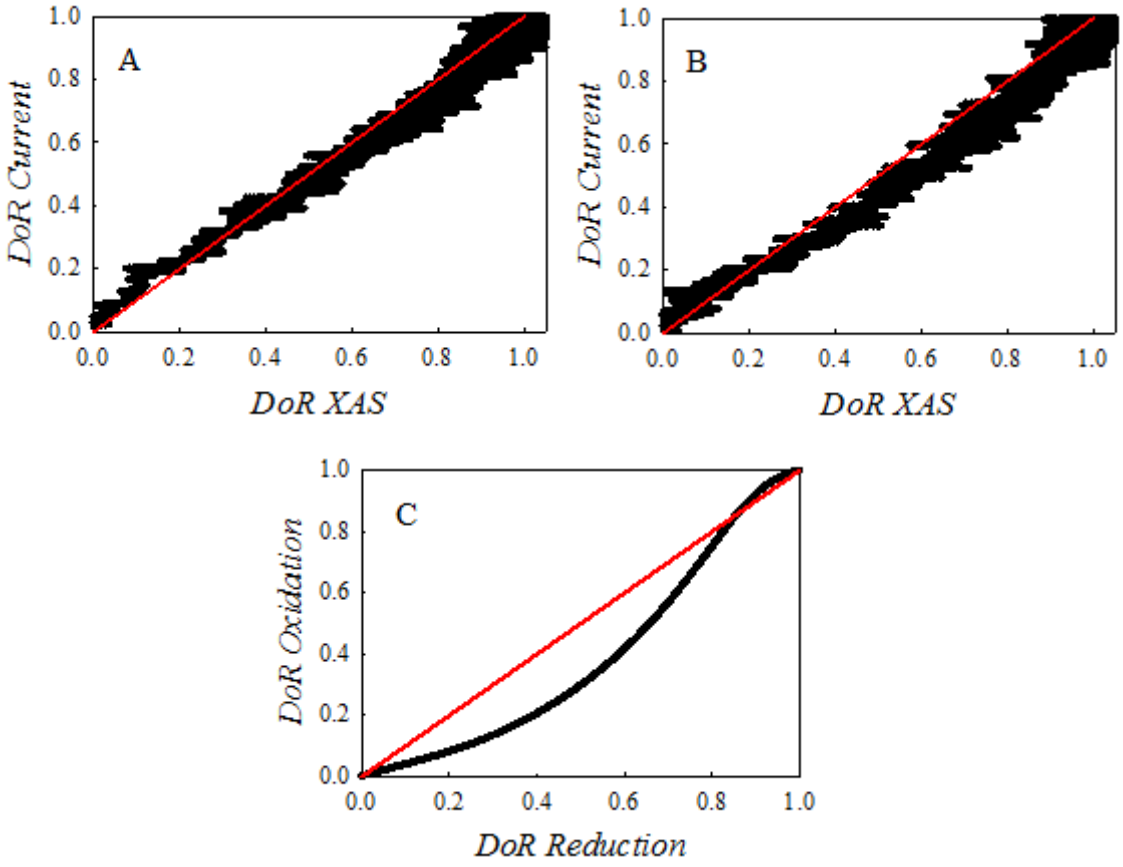

Figure 5.27. Results obtained for the reduction Ir(IV) →Ir(III) and the oxidation Ir(III) →Ir(IV). The potential jumps associated are 1.0→0.2 V and 0.2→1.0 V respectively and measurements have been carried out in acidic medium. A) *DoR* from current *vs DoR* from XAS for the reduction process. B) *DoR* from current *vs DoR* from XAS for the oxidation process. C) *DoR* of oxidation *vs. DoR* of reduction (both from the integral of the current).

Furthermore, we should point out that, if the mechanisms for the reduction and the oxidation were exactly the same, the correlation plot of the *DoR* of oxidation vs the *DoR* of reduction would also give a straight line in correspondence of the diagonal of the first quadrans. Such a comparison is shown in Fig. 5.27.C using the *DoR*s determined by the current for better clarity: the reduction is notably faster at the beginning (*DoR* < 6) and then slower at the very end.

Fig 5.28 illustrates the results obtained by testing the model described in Eq. (5,6) and (5,7) against the experimental data. It is well apparent that for the reduction process (Fig. 5.28.A) data are well interpreted by the Eq. (5,7) for t > 6 s *ca.*, and by Eq. (5,6) in all the time interval considered. This suggests that the reduction Ir(IV) → Ir(III) takes place under diffusion control in all the time interval investigated. The diffusion coefficient obtained by fitting the linear part of the graph shown in Fig. 5.28.B is ca. 4.4 x 10^{-6} cm^2/s.

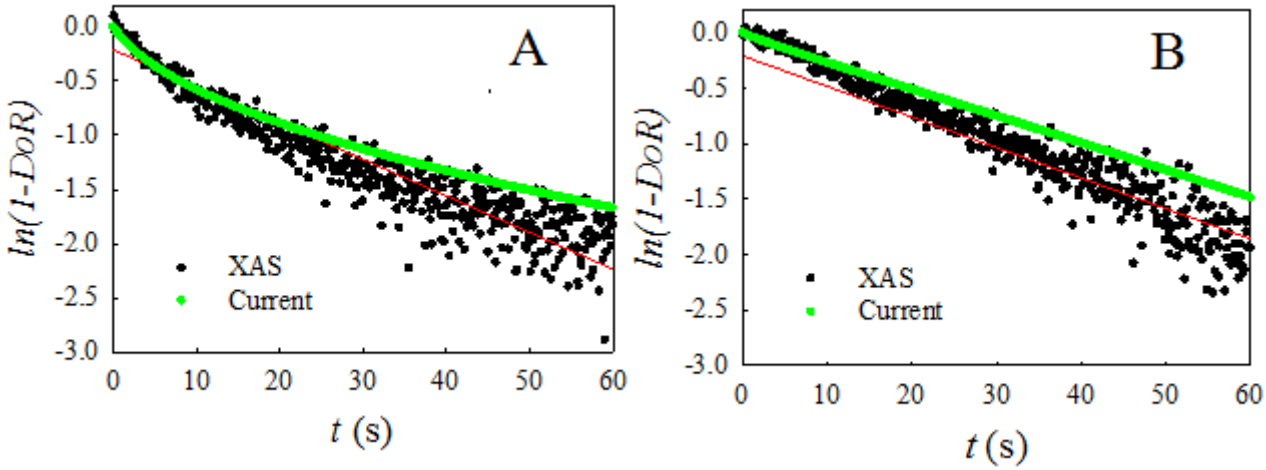

Figure 5.28. A) ***ln (1-DoR)*** **vs** ***t*** **for the reduction process (1.0→0.2 V). B)** ***ln (1-DoR)*** **vs** ***t*** **for the oxidation process (0.2→1.0 V). The green points refer to the** ***DoR*** **obtained from the current, the black points refer to the** ***DoR*** **obtained from the XAS, and the red trace shows the asymptotic fitting model described in the text.**

Now, we can discuss the oxidation Ir(III) → Ir(IV) (Fig. 5.28.B). The plot of the *DoR* vs *t* is characterized by a linear trend extrapolating at $\ln(8/\pi^2)$ for t=0 after 15 s ca.. In this case the diffusion coefficient obtained by the fit of the linear part is ca. 3.6 x 10^{-6} cm^2/s. The initial stages of the process are limited by a slower step, giving also a linear trend of ln(1-*DoR*) vs *t*. This feature is a further evidence to the fact that the reduction from Ir(IV) to Ir(III) is faster than the oxidation from Ir(III) to Ir(IV) for small *DoRs*.

Finally, let's consider the series of spectra acquired in oxygen evolution conditions. This case provides a clear evidence that coupling X-ray Absorption Spectroscopy and current measurements leads to important insights into the

mechanism in order to clarify whether the processes involve side reactions or parasitic effects. The chronoamperometric programs applied are characterized by the potential steps 1.5 V → 1.05 V and 1.05 → 1.5 V (1.3 V marks the potential conditions at which oxygen evolution reaction begins). In this last case, the *DoR* obtained by XAS is not directly comparable with the integral of the current since oxygen evolution occurs uninterruptedly and thus the time integral of the current does not reach zero. So, at long enough tomes, a constant current value was estimated and preliminarily subtracted to the raw current data.

Fig. 5.29.A and Fig. 5.29.B illustrate the correlation plot of the *DoR* obtained by the integral of the current vs the *DoR* obtained by XAS for both potential steps. We can observe that spectroscopy and electrochemistry are not in good agreement. For the potential step 1.5 V → 1.05 V, the correlation plot lies above the diagonal of the first quadrans thus indicating that the process described by the current is faster if compared to Ir reduction. This result can be explained by the occurrence of another process in parallel with Ir reduction. For the potential step 1.05 V → 1.5 V, the variation in the oxidation state of iridium takes place at a rate that it is comparable to the exchange of electrons (we should not forget that we have subtracted the contribution due to oxygen evolution). Furthermore, the mechanisms of the reductions and of the oxidation reactions are not the same as shown by Fig. 5.29.C and Fig. 5.29.D which illustrate the correlation between the *DoR* of the oxidation and the *DoR* of the reduction process calculated on the basis of the integral of the current and of the XAS respectively. The experimental evidence is that the process investigated in oxidation conditions is notably faster than the one investigated in reduction conditions. A reasonable explanation to this lies in the occurrence of an electrochemical process, not involving changes in the oxidation state of iridium.

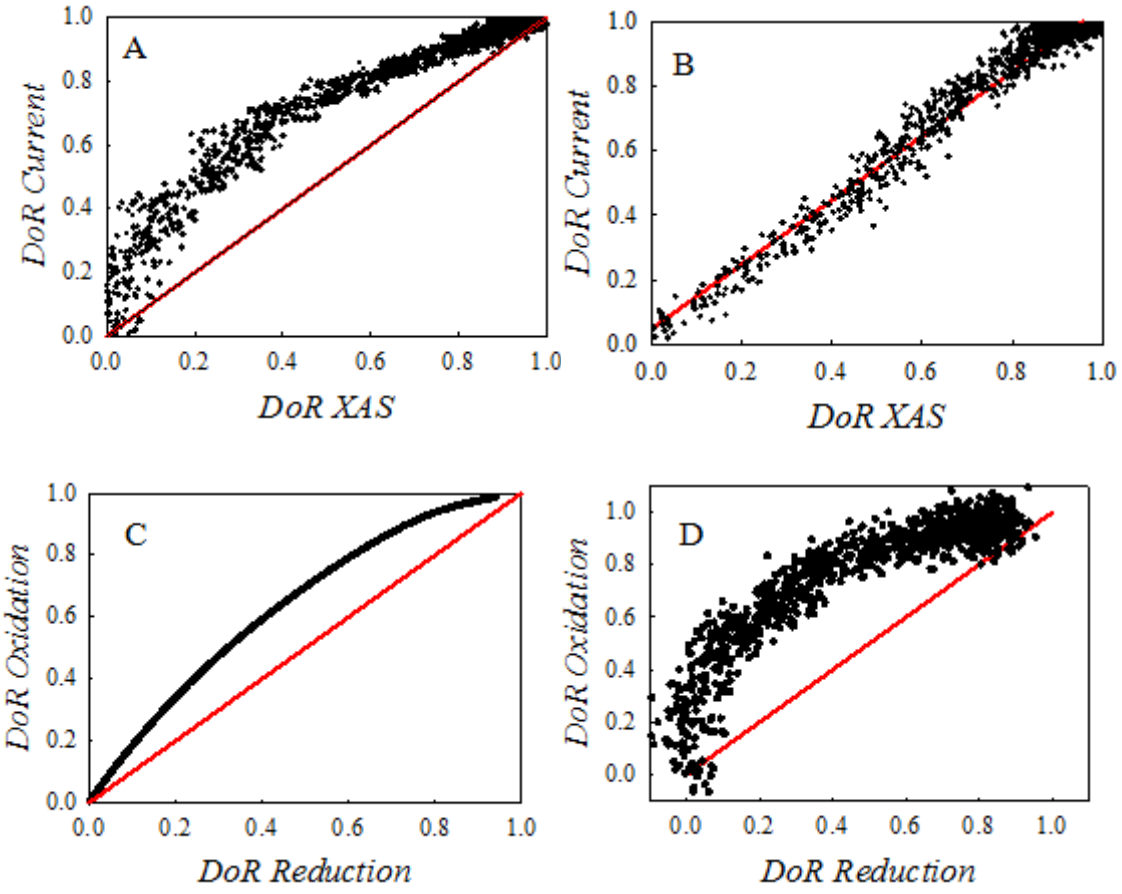

Figure 5.29. A) *DoR* obtained by the integral of the current vs. the *DoR* obtained by the XAS for the potential step 1.5 → 1.05 V. B) *DoR* obtained by the integral of the current vs. the *DoR* obtained by the XAS for the potential step 1.05 → 1.5 V. C) *DoR* of oxidation *vs.* the *DoR* of reduction obtained from the integral of the current. D) *DoR* of oxidation *vs.* the *DoR* of reduction obtained from XAS.

In Fig. 5.30 we can see the results obtained by testing the model described in Eq. (5,7) to the data obtained for the potential step 1.5 V → 1.05 V (A) and for the potential step 1.05 V → 1.5 V (B). For the measurements acquired in oxidation conditions, the *DoR* from XAS shows all features required by the diffusion model described by Eq. (5,7) such as the linear trend at high times, the extrapolation of the linear trend to to $\ln(8/\pi^2)$ for $t = 0$, the upwards curvature of the trend of the initial data. In this case, the estimated D value is ca. 5.2×10^{-6} cm^2/s. For the same process, the *DoRs* from current data are initially in agreement with the *DoRs* from XAS, then they become regularly larger, and follow a roughly linear trend that is not consistent with the features of the

diffusion model. In this case a tentative explanation concerns the oxygen evolution process related to the formation of Ir(V) clusters. According to this assumption, the formation of proximal Ir(V)-Ir(V) couples takes place after ca. 20 s.

For the measurements recorded in reduction conditions, it is evident that Ir reduction accounts for only a certain amount of the total charge exchanged and that the *DoRs* (both from XAS and current) do not show the features required by the model. An explanation to this could be that the process does not occur under diffusion control.

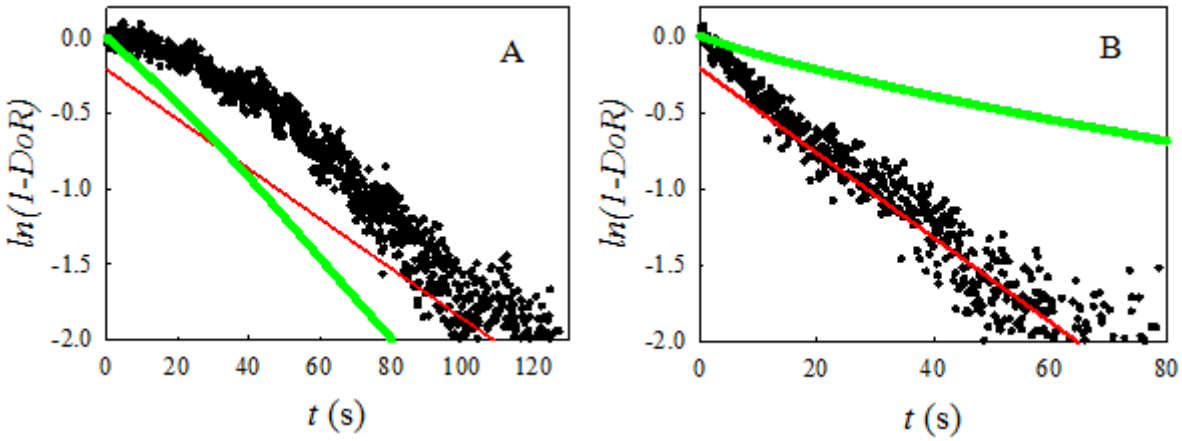

Figure 5.30. Testing of the diffusion model described in Eq. (5,7) for the data related to the potential step 1.5 V → 1.05 V (A) and for the data related to the potential step 1.05 V → 1.5 V. Green points: *DoR* from the integral of the current; black points: *DoR* from XAS; red trace: diffusion model.

5.3.4. CONCLUSIONS

The Dispersive-XAS measurements performed *in situ* onto IrO_x electrodes, while applying different chronoamperometric programs, allowed us to study the stability of IrO_x material and the behaviour of the photo-absorber with a time resolution of subseconds.

From the EXAFS signals it was possible to monitor the local chemical and geometric environment of iridium. The results obtained showed that the local structure around iridium remains the same while Ir changes oxidation state and it is quite similar to that of the rutile. This is a nice proof that the material is very flexible in accommodating different oxidation states of Ir.

The XANES allowed us to gain key information about the mechanisms of the kinetics of the electrochemical reactions under different chronoamperometric programs in acidic medium:

(i) For the potential window 0.2 V – 1.05 V the agreement between spectroscopy and electrochemistry confirms the absence of non-faradic phenomena. Furthermore, the reduction process is clearly faster than the oxidation one and both of them are well interpreted by the diffusion model consisting of a finite layer characterized by an infinite source of protons (Eq. (5,7)).

(ii) For the potential window 1.05 V – 1.5 V, spectroscopy and electrochemistry are not in agreement neither for the potential step up nor for the potential step down. This can be reasonably explained by the occurrence of non-faradic phenomena. For the potential step 1.05 V → 1.5 V, data are well interpreted by the diffusion model described by Eq. (5,7) whereas it cannot be employed for the potential step 1.5 V → 1.05 V. A reasonable explanation lies in the occurrence of a process which does not change Ir oxidation state.

REFERENCES

[1] H. Dau, C. Limberg, T. Reier, M. Risch, M. Roggan and P. Strasser, *Chem.Cat. Chem.* (2010), 2, 724—761;

[2] A. Minguzzi, O. Lugaresi, C. Locatelli, S. Rondinini, F. D'Acapito, E. Achilli and P. Ghigna, *Anal. Chem.* (2013), 85, 7009−7013;

[3] A. Vertova, L. Borgese, G. Cappelletti, C. Locatelli, A. Minguzzi, C. Pezzoni and S. Rondinini, *J. Appl. Electrochem.* (2008), 38, 973−978;

[4] C. Locatelli, Minguzzi, A. Vertova, P. Cava and S. Rondinini, *Anal. Chem.* (2011), 83, 2819−2823;

[5] F. D'Acapito, A. Trapananti, and A. Puri, *J. Phys.: Conf. Ser.* (2016), 712, 012021;

[6] B. K. Agarwal, "X-ray Spectroscopy: An Introduction" (Springer Series in Optical Sciences), Springer-Verlag, Berlin, Heidelberg, New York, (1991);

[7] L. Mandelstam and Ig. Tamm, *J. Phys. (USSR)* (1945), 9, 249-254;

[8] J.H. Choy, D.K. Kim, G. Demazeau, D.-Y. Jung, *J. Phys. Chem.* (1994), 98, 6258-6262;

[9] J.-H. Choy, D.-K. Kim, S.-H. Hwang, G. Demazeau and D.-Y. Jung, J. *Am. Chem Soc.* (1995), 117, 8557-8566;

[10] P. Ghigna, G. Spinolo, M. Scavini, U. A. Tamburini and A. V. Chadwick, *Physica C* (1995), 253, 147-155;

[11] A. R. Hillman, M. A. Skopek and S. Gurman, *Phys. Chem. Chem. Phys.* (2011), 13, 5252-5263;

[12] J.-H. Choy, D.K. Kim, G. Demazeau, D.-Y. Jung, *J. Phys. Chem.*(1994), 98, 6258-6262;

[13] A. Minguzzi, C. Locatelli, O. Lugaresi, E. Achilli, G. Cappelletti, M. Scavini, M. Coduri, P. Masala, B. Sacchi, A. Vertova, P. Ghigna and Sandra Rondinini, *ACS Catal.* (2015), 5, 5104−5115;

[14] C. Prestipino, O. Mathon, R.o Hino,a A. Betevaa and S. Pascarelli, *J. Synchrotron Rad.* (2011), 18, 176−182;

[15] S. Pascarelli, O. Mathon, M. Munoz, T. Mairs and J. Susini *J. Synchrotron Radiat.* (2006), 13, 351;

[16] S. Pascarelli and O. Mathon *Phys. Chem. Chem.* Phys. (2010), 12, 5535;

[17] J. C. Labiche, O. Mathon, S. Pascarelli, M. A. Newton, G. G. Ferre, C. Curfs, G. Vaughan, A. Homs and D. F. Carreiras *Rev. Sci. Instrum.* (2007), 78, 091301 27;

[18] S. J. A. Figueroa, and C. Prestipino, J. Phys.:Conf. Ser. (2016), 712, 012012;

[19] N. Binsted, S.S. Hasnain *J. Synch. Rad.* (1996), 3, 185;

[20] MINUIT – Function Minimization and Error Analysis, CERN Program Library entry D506;

[21] R. T. Downs and M. Hall-Wallace, "The American Mineralogist crystal structure database," *The American Mineralogist* (2003), 88, 247−250;

[22] F. James, "Minuit, Function Minimization and Error Analysis, Reference Manual, Version 94.1", *CERN Program Library Long Writeup D506*, CERN, Geneva 1994;

[23] J. Crank "The Mathematics of Diffusion", 197.

6. IrO_X/α-Fe_2O_3 COUPLING AND THE PHOTO-ELECTROCHEMICAL WATER SPLITTING

The goal of the work described in this chapter is to shed light on the role of Ir catalyst when coupled to a semiconductor for light-driven water splitting[1]. Photo-electrochemical water splitting represents in principle the ideal energy conversion process since it allows the direct production of high purity hydrogen from sunlight. When a semiconductor is irradiated by UV-Vis light characterized by energy larger than the gap, electron-hole pairs are generated by excitation from the valence to the conduction band. In presence of a *n*-type semiconductor, thanks to the space charge generated within the semiconductor when in contact with an electrolyte, holes migrate towards the semiconductor/electrolyte interface and oxidize water to oxygen, while electrons are driven through an external circuit to a counter electrode where reduce water to hydrogen. In this work we consider photo-anodes in which IrO_x electrocatalyst is coupled to a semiconductor part composed of α-Fe_2O_3. Hematite is considered one of the most promising materials because of its low cost, absorption in the visible region and high stability under working conditions. The behaviour of such a photo-electrochemical architecture is still not well understood and the experiments described demonstrate how it is possible to directly observe charge transfer phenomena between hematite and IrO_x while applying different potentials. Photo-anodes investigated are described in section 3.1.4.

6.1. THE *IN SITU*-XAS INVESTIGATION

The experimental part was carried out on BM08 (LISA beamline, ESRF)[1]. X-ray Absorption measurements were performed in situ and in operando at the Ir-L_{III} edge in the fluorescence mode and the experimental scheme was designed in order to investigate light-driven electrochemical processes (Fig. 6.1).

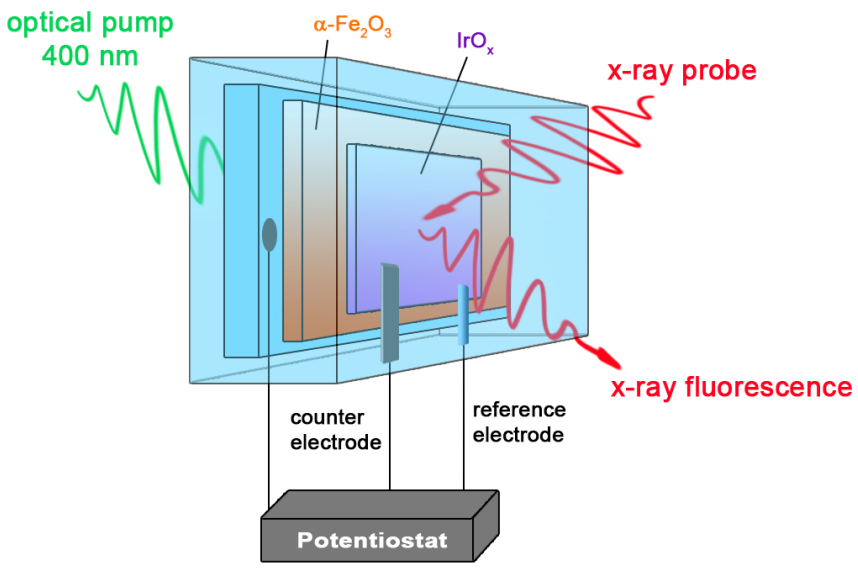

Figure 6.1. Representation of the photo-spectroelectrochemical setup.

UV-Vis light was generated by means of a 400 nm LED. The photo-electrochemical cell employed was built by means of a 3D printer (see section 4.5.2). This device mounted with the three-electrodes setup is shown in Fig. 6.2: the working electrode is composed of an IrO_x domain in contact with hematite supported onto Fluorine-doped Tin Oxide (FTO), the counter electrode is represented by a Pt foil and the reference is a Ag/AgCl.

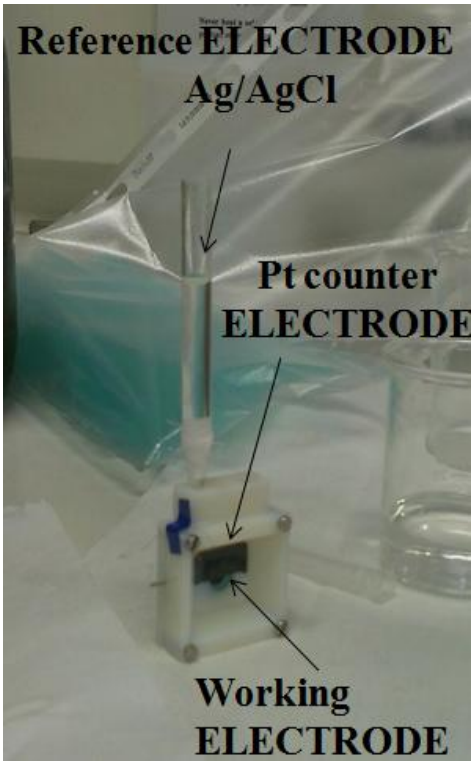

Figure 6.2. Scheme of the photo-spectroelectrochemical device mounted with the three electrodes assembly.

The design of the cell was made in order to ensure a width of the 1 M HK_2PO_4 solution equal to 1 mm. The need to fulfil this requirement lies in the fact that one side of the electrocatalyst is in contact with Fe_2O_3, which prevents from measuring X-ray fluorescence, and the other with the electrode solution. We should remember that the absorption length of water is 0.363 cm at 11215 eV and thus the width of the solution layer should not be larger than 1 mm in order to allow the recording of spectra with adequate signal-to-noise ratio. The reference electrode is separated from the solution by means of a salt bridge filled with agar and containing a 0.2 M aqueous solution of $KClO_4$. One side of the electrochemical device presents a hole matching with the area of the working electrode.

The investigation of the α-Fe_2O_3 /IrO_x systems was carried out in a broad potential window which is much wider than that in which water splitting occurs. The intention is to clarify the behaviour of the electrochemical architecture in the different electrochemical conditions.

FEXRAV and XANES signals were recorded at room temperatures both under UV-Vis light irradiation and in dark conditions.

6.1.1. LIGHT AND DARK XANES SIGNALS OF THE PHOTO-ANODES

While investigating the α-Fe_2O_3 /IrO_x systems, FEXRAV[2] measurements were applied for the first time in a photo-electrochemical configuration in order to study the variations in the absorption coefficient μ during a Cyclic Voltammetry both under UV-Vis irradiation and in dark conditions (Fig. 6.3). The energy was kept fixed to 11221 eV, which corresponds to the energy position of the WL for Ir(IV). The electrodic solution was 1 M K_2HPO_4 at a pH equal to 9.75: it was a good compromise in order to ensure the stability of both IrO_2 and hematite and to avoid any local pH variation induced by prolonged proton production during the water oxidation process. The signals recorded account for a higher absorption coefficient in presence of photo-currents.

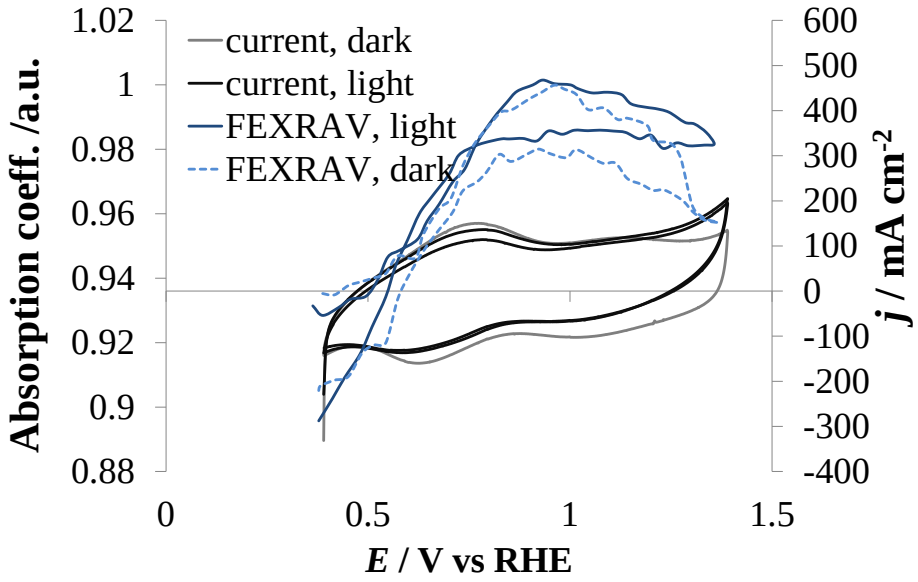

Figure 6.3. FEXRAV (second cycle) of Ir at 11221 eV. Hydrous IrO_x is deposited onto hematite, that is kept in the dark (dark blue, full line) or illuminated by means of a 410 nm LED (light blue, dashed line). In the figure, the data are normalized to absorption coefficient equal to 1 at an applied potential of 1 V for the sake of better comparison. The corresponding values of current densities (current intensities normalized for the geometric area under illumination) are reported in the secondary scale both as recorded under illumination (black line) and in the dark (grey line).

Furthermore, a technique based on a slight modification of FEXRAV method was also applied in order to study the variations in the absorption coefficient μ

while changing UV-Vis light conditions. Fig. 6.4 illustrates the raw Fixed Energy Absorption Signal acquired during the application of three UV-Vis light "off-on" cycles of 500 s. The measurement was carried out applied while keeping the applied potential equal to 1.1 V, at which all iridium is supposed to be present in the form of Ir(IV). The UV-Vis irradiation determines an increase in the absorption coefficient. A reasonable explanation to this phenomenon is the photo-deposition of Ir during irradiation.

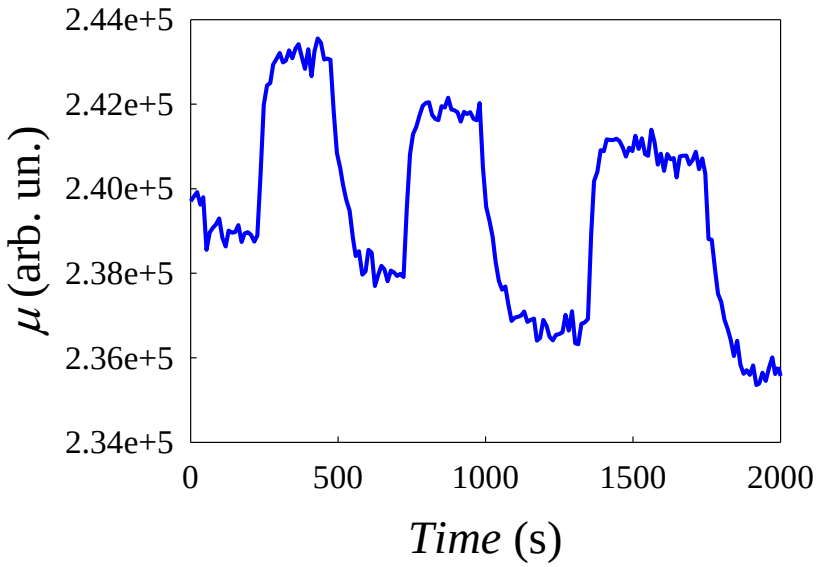

Figure 6.4. Absorption coefficient μ recorded at a fixed energy value (11221 eV) during the application of three UV-Vis light "off-on" cycles of 500 s. Potential was kept equal to 1.1 V.

Afterwards, XANES spectra were collected while applying different potentials (in the range from 0.1 to 1.4 V) both in dark conditions and under UV-Vis light irradiation. The measurements were performed in order to minimize possible systematic errors: for each energy value the acquisition was performed both in presence ("light") and in absence ("dark") of UV-Vis light before stepping the monochromator to the higher energy value. This ensures that for each energy value the absorption coefficient in light or dark conditions is measured in the same instrumental conditions. The most striking difference between the XANES

spectrum collected under irradiation and the one collected in dark conditions appears at 1.4 V (vs. RHE), when photocurrent is observed (Fig. 6.5).

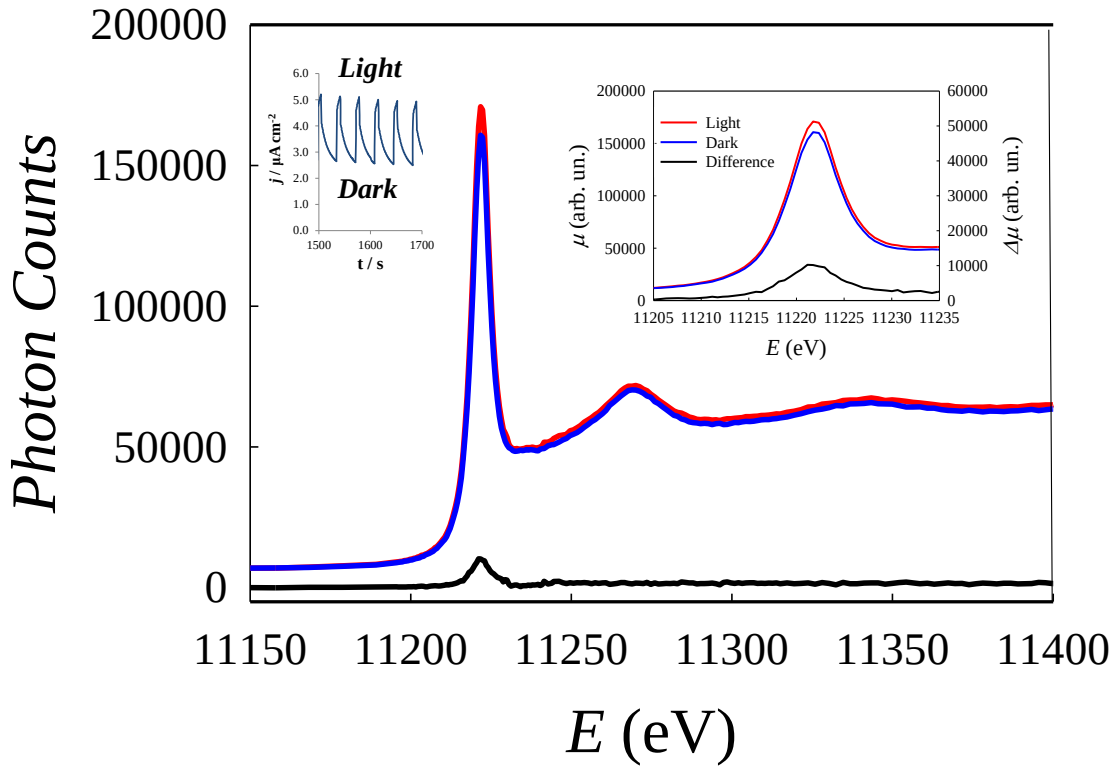

Figure 6.5. Ir-L_{III} edge XANES spectra acquired in presence (red line) and in absence (blue line) of UV-Vis light irradiation and the corresponding difference (black line) at 1.4 V (vs. RHE) in aqueous 1 M K_2HPO_4. The inset in the right side is a magnification of the XANES region while the one in the left side shows a series of dark/light steps during the XAS acquisition.

UV-Vis irradiation affects both the XANES and the EXAFS regions (located at energy values larger than 11235 eV). As shown in Fig. 6.5, the absorption coefficient μ increases under illumination thus accounting for a larger amount of photo-absorbers in the X-ray beam. However, the most important insights come from the XANES region of the two spectra. The significant difference observed in this region remains even after the normalization of the two data sets. This feature is a clear indication that the increase in the absorption coefficient under irradiation is not simply associated to a quantitative effect but is due to differences in the *5d* band. The larger WL peak area suggests that the *2p* → *5d* electronic transition is more probable, likely because the *5d* band is

less filled. This assessment implies the occurrence of a hole transfer from the excited hematite to the IrO_x domain in presence of UV-Vis light.

In order to investigate the bilayer architecture in different electrochemical conditions, the X-ray Absorption Analysis was extended to lower potentials: 0.8, 0.4 and 0.1 V. The last potential represents the electrochemical conditions at which electron accumulation likely establishes.

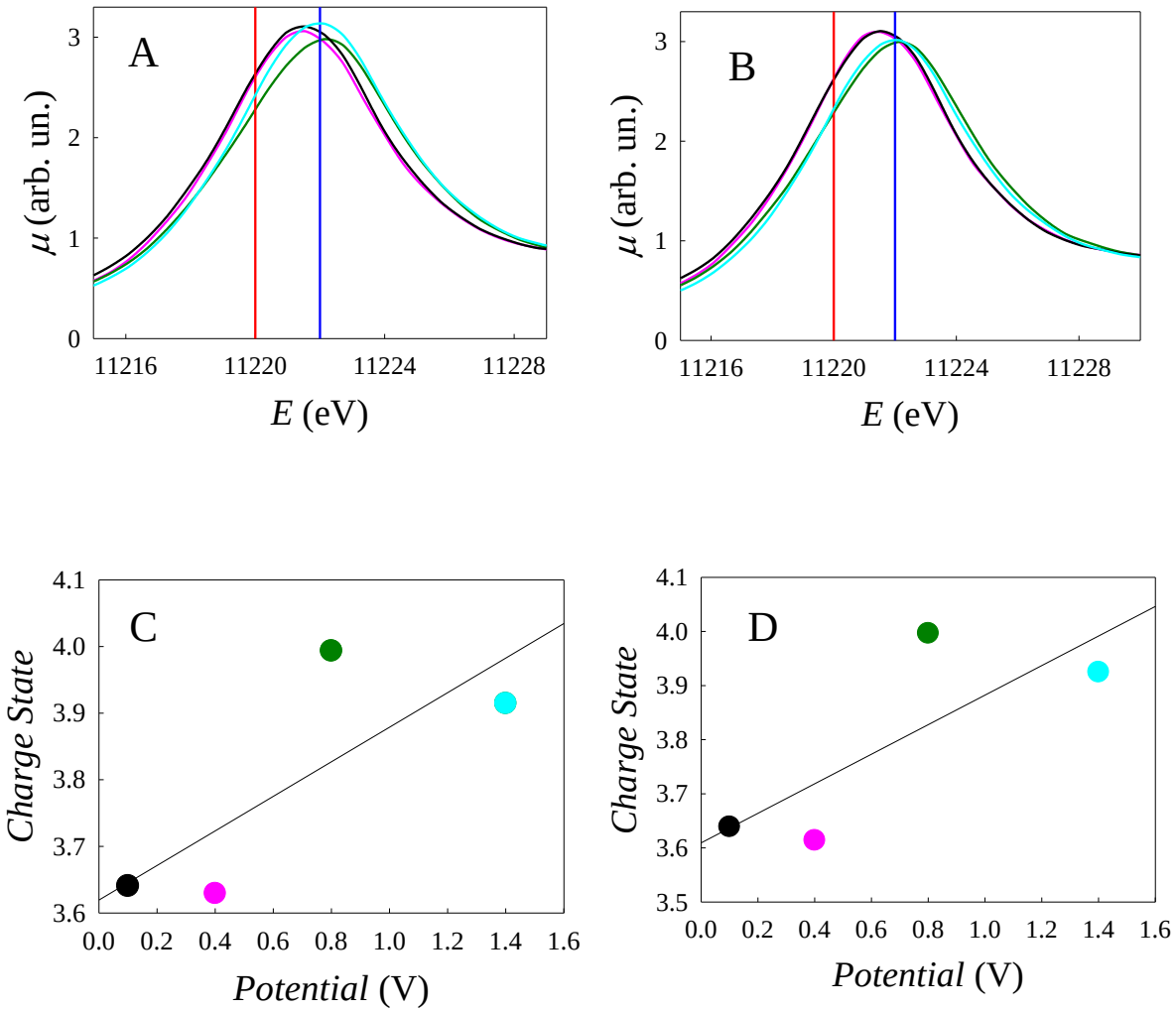

Figure 6.6. Ir L_{III} XANES spectra obtained in UV-Vis light (A) and dark (B) conditions at different potential values: 0.1 V (black line), 0.4 V (pink line), 0.8 V (green line) and 1.4 V (cyan line). For reference, the absorption edges of Ir(III) and Ir(IV) standards are indicated as vertical lines, red and blue respectively. The charge state Vs applied potential graphs are illustrated for the light (C) and dark (D) conditions. Charge states have been obtained from XANES fitting procedures.

Fig. 6.6.A and 6.6.B illustrate the XANES spectra collected at the four different potential values investigated with and without the presence of the UV-Vis light respectively. For a better reference, the absorption edges of Ir(III) and Ir(IV) standards are indicated as vertical lines (red and blue respectively). At first sight we can observe a shift of the absorption edge as the potential increases for both the light and dark conditions. When the potential is equal to 0.1 and 0.4 V the absorption edges lie between those of $IrCl_3$ and IrO_2 standards, suggesting that the mean oxidation state of iridium lies between (III) and (IV), while for larger potential values (0.8 and 1.4 V) the position of the absorption edges are very similar to that of IrO_2, thus indicating that the oxidation state of iridium is very close to (IV). This provides a support to what was previously observed by means of FEXRAV investigation (Fig. 6.3): the decrease in the absorption coefficient, taking place when the potential is lower than 0.8 V, can be explained by the shift of the absorption energy towards lower energy values.

In order to quantify rationally the energy shift, a fitting of the XANES spectra was performed. This procedure was carried out by means of a linear combination of an arctangent and a Lorentzian function. Having in mind that $IrCl_3$ and IrO_2 contain Ir(III) and Ir(IV) respectively, and considering the position of their absorption edges, a relationship between the absorption position and the charge state of the photo-absorber can be obtained:

$$\textit{(Charge State)} = 0.6211 \times \textit{(Lorentzian Position, eV)} - 6966 \qquad (6,1)$$

The trend of the charge states Vs the potential is shown in Fig. 6.6.C and 6.6.D for both the UV-Vis and dark conditions respectively. The numerical values are indicated in Tab. 6.1.

DARK CONDITIONS	
Potential (V)	*Charge State*
0.1	3.64
0.4	3.61
0.8	4.00
1.4	3.92

LIGHT CONDITIONS	
Potential (V)	*Charge State*
0.1	3.64
0.4	3.63
0.8	3.99
1.4	3.91

Table 6.1. Charge state values estimated by means of Eq. (6,1) for each applied potential both in absence and in presence of UV-Vis irradiation.

The results obtained are roughly the same for the light and the dark conditions and they illustrate that the charge state of Ir ranges from 3.6 to 4.0. We can conclude that the shift in the absorption peak and therefore in the oxidation state range of Ir is smaller if compared to previous results (see Chapter 5). A reasonable explanation to this is the ohmic drop due to the presence of the hematite.

Fig. 6.7, for each potential value, shows the difference signal obtained by subtracting the XANES spectrum acquired in dark conditions from that acquired under irradiation. Very interestingly, all difference spectra obtained for potentials lower or equal to 0.8 V are marked by an increase in the weight at low energy values and a decrease in the weight at high energy values. This experimental evidence accounts for a shift toward lower energy values and thus for a partial reduction of iridium in presence of UV-Vis light due to the photoelectrons injected in the overlayer. These are able to partially fill the empty *5d* band of Ir, directly observed at the Ir L_{III} edge. It is important to note that no significant photocurrent (due to water splitting reaction) are observed in these electrochemical conditions. This means that charge transfer phenomena between hematite and iridium oxide exist and are not limited to the jump of a hole from the semiconductor domain to the electrocatalytic part. Furthermore,

the occurrence of an electron transfer at low potential values is an indication of a good overlap between the semiconductor and the IrO_x electronic states. This represents a very important insight in the study of the role of overlayers on hematite photoanodes.

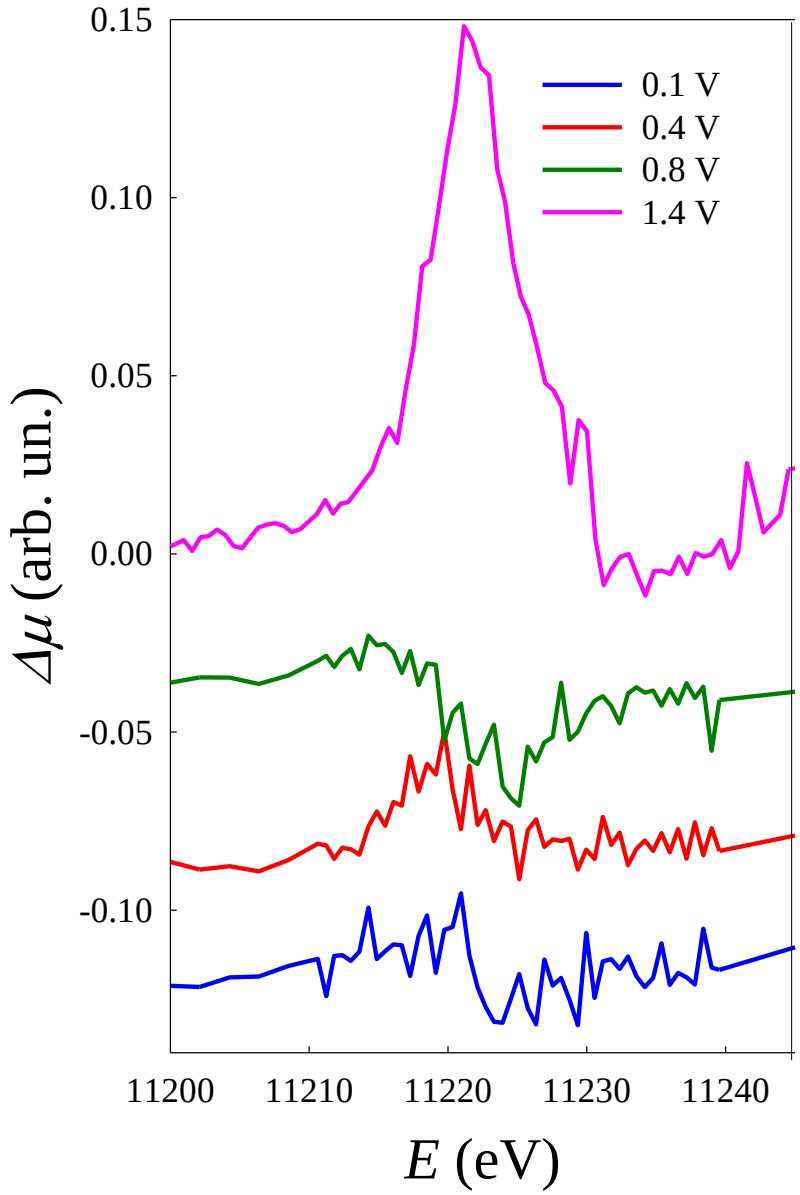

Figure 6.7. Light – Dark difference signal for the different applied potentials. The differences were calculated after normalization of the original spectra.

On the basis of the results obtained, it is possible to conclude that the beneficial effects of the overlayer (anticipated photocurrents) are not directly related to an improved reaction kinetics but rather lie in a modification of the energies of the semiconductor generated by the contact with the iridium oxide part. Also according to transient absorption spectroscopy experiments[3], the effectiveness of the overlayer is not associated to a true catalytic effect but to a depletion of electron density in the semiconductor. The occurrence of a hole transfer and the suppression of photocurrents in the presence of an overlayer are strictly correlated. We should remember that the overlayer consists of a highly conductive oxide, which is characterized by large redox activity with extended density of states. Furthermore, the oxide should accumulate a sufficient amount of oxidative equivalents before reaching the threshold of the catalytic cycle, consisting of vicinal Ir(V) states[4]. Before attaining this condition, the holes are accumulated in the overlayer and are stored causing an increase in the occupancy of Ir *5d* states: IrO_x acts as a "hole trap".

Fig. 6.8 show a scheme for the suggested mechanisms occurring in the bilayer architecture when E ≤ 0.8 V (left side) and when E is equal to 1.4 V (right side). The illumination by means of UV-Vis light determines an electron transfer from the valence band to the cinduction band of hematite. For the lower applied potentials an electron transfer takes place from the conduction band of the hematite to the *5d* states of Ir.

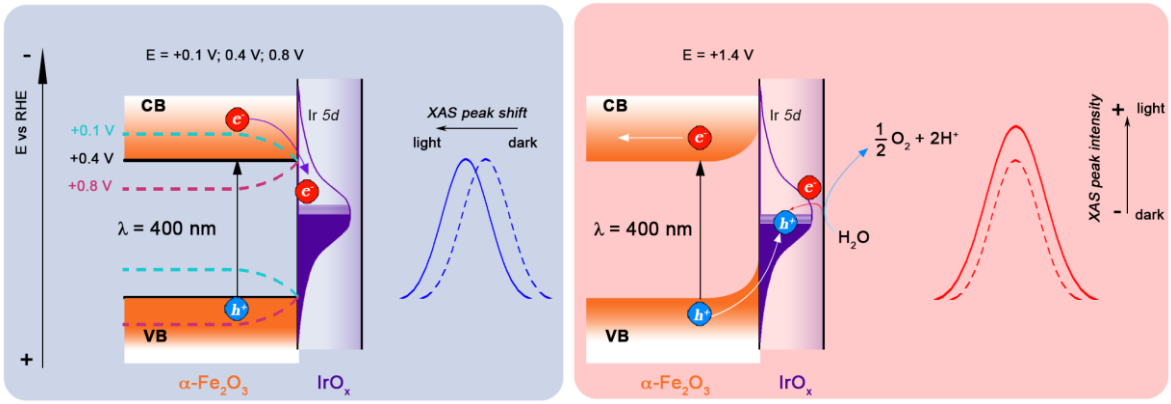

Figure 6.8. Scheme of the charge transfer processes occurring between the α-Fe_2O_3 and the IrOx for potential lower or equal to 0.8 V (left) and at potential equal to 1.4 V (right).

This phenomenon is responsible for a reduction of Ir and determines a shift of the absorption edge toward lower energy values. In oxygen evolution conditions (E=1.4 V), it is reasonable to assume that a hole is transferred from the valence band of the hematite to the *5d* states of Ir. This is subsequently filled by the oxygen evolution reaction. This phenomenon is responsible for an increase in the WL peak area as shown in Fig. 6.8.

6.2. "PUMP AND PROBE" TIME RESOLVED ANALYSIS

In order to gain a more datailed understanding about the kinetics and the mechanism of the processes described in the previous section, a "pump and probe" time resolved analysis was carried out. This was able to improve the time resolution up to hundreds of nanoseconds[5]. Thanks to a multi-bunch based experimental setup (Fig. 6.9), it became possible study the process with a delay of 600 ns between the UV pump and the X-ray probe.

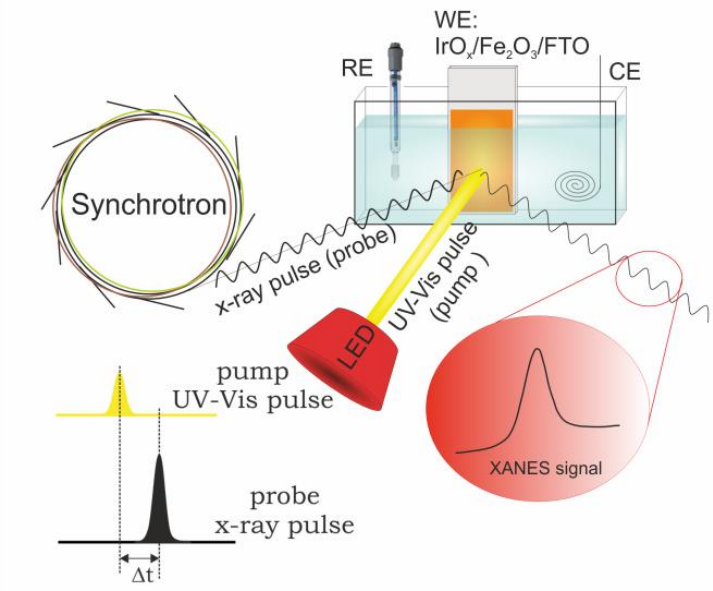

Figure 6.9. Scheme of the "pump and probe" time resolved XAS experiment on the bilayer photo-anodes deposited on Fluorine doped Tin Oxide (FTO). The pump is represented by a UV flash of 60 ns at λ =400 nm and the probe is the X-ray pulse. The storage ring operated in the 4 bunches mode with a bunch spacing of 700 ns and a pulse duration of 100 ps.

The experiment was carried out on LISA beamline[1] with the storage ring operating in the 4 bunches mode with a bunch spacing of 700 ns and a pulse duration of 100 ps. The pump was a UV Light Emitting Diode (LED) working at a wavelenght of 400 nm and characterized by a FWHM of 10 nm. The UV flash are charcterized by a duration of 60 ns (Fig. 6.10).

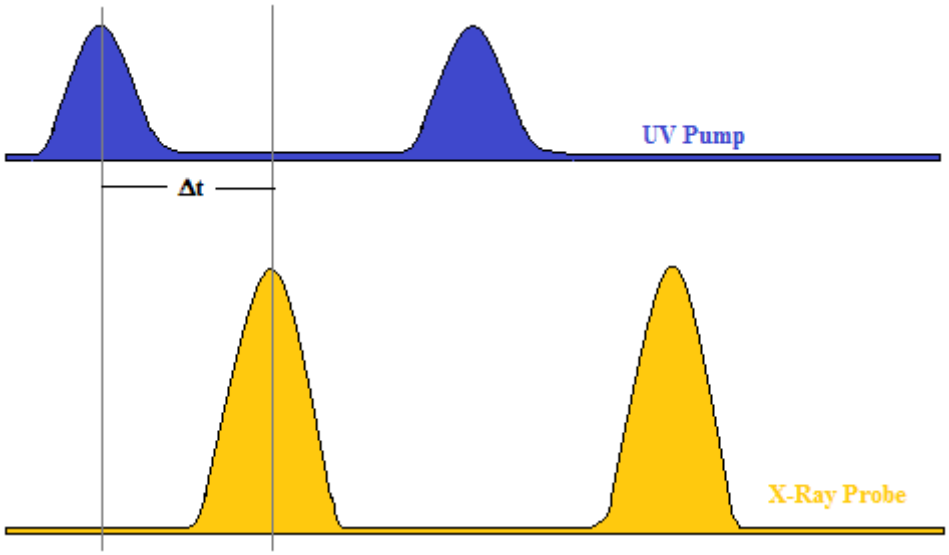

Figure 6.10. Time-resolved "pump and probe" XAS. The UV pump duration is 60 ns, while the X-ray probe duration is 100 ps. The distance between the X-ray bunches in the 4 bunches mode is 700 ns.

In order to synchronize it with the X-ray flashes we employed a programmable board (BCDU8, ESRF) and we used a fast Photo-multiplier Tube detector to monitor the correct timing. The flux on the sample was hestimated to be ca. 0.5 W in continuous wave mode. The acquisitions were made both in simultaneous irradiation of UV and X-rays with a delay of 600 ns, which is very close to the maximum allowed by the four bunches mode at the ESRF. For each energy point the aquisition was made both in presence and in absence of the UV pulse before stepping to a higher energy value. The intention was to study the differences between the spectra avoiding errors due to the movement of the monochromator. The energy calibration was based on the measure of the

Absorption Spectrum of a metallic Platinum foil at the Pt-L_{III} edge (Pt-L_{III}: 11564 eV). All signals were obtained at room temperature.

A picture of the spectro-electrochemical device employed for these measurements is illustrated in Fig. 6.11.

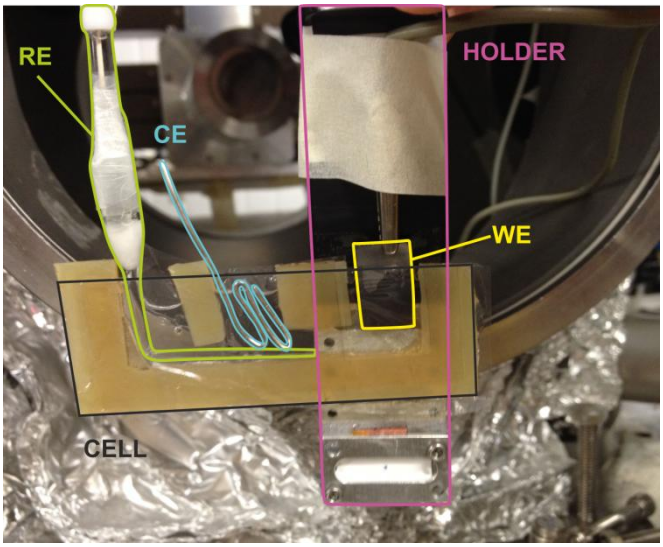

Figure 6.11. Image of the spectro-photoelectrochemical cell mounted on BM08 beamline with the three electrodes setup: working electrode (WE) constituted of IrOx/α-Fe_2O_3@FTO, counter electrode (CE) made of platinum and reference electrode (RE) constituted of Ag/AgCl.

The cell, assembled manually by means of a mylar film and silicon, is transparent to both UV light and X-rays and allows a lodging for a counter electrode and a glass tube hosting the reference. The electrolyte solution employed was aqueous 0.1 M K_2HPO_4 (ensuring a pH of 9.1) or 0.5 M NaH_2PO_4 (ensuring a pH of 11.1).

6.2.1. "PUMP AND PROBE" TIME RESOLVED RESULTS

In the present experiment Ir-L_{III} XANES spectra were acquired at two different applied potentials: 1.56 V Vs RHE, which is situated after the onset of the anodic photocurrent, and 1.46 V[5]. Fig. 6.12 shows the comparison between the Ir-L_{III}

XANES spectra acquired at 1.56 V without and with the activation of the UV pump both for the application of a delay of 600 ns between the pump and the probe and for simultaneous irradiation by means of UV light and X-rays. Results presented are obtained from the average of three data sets obtained in the same experimental conditions.

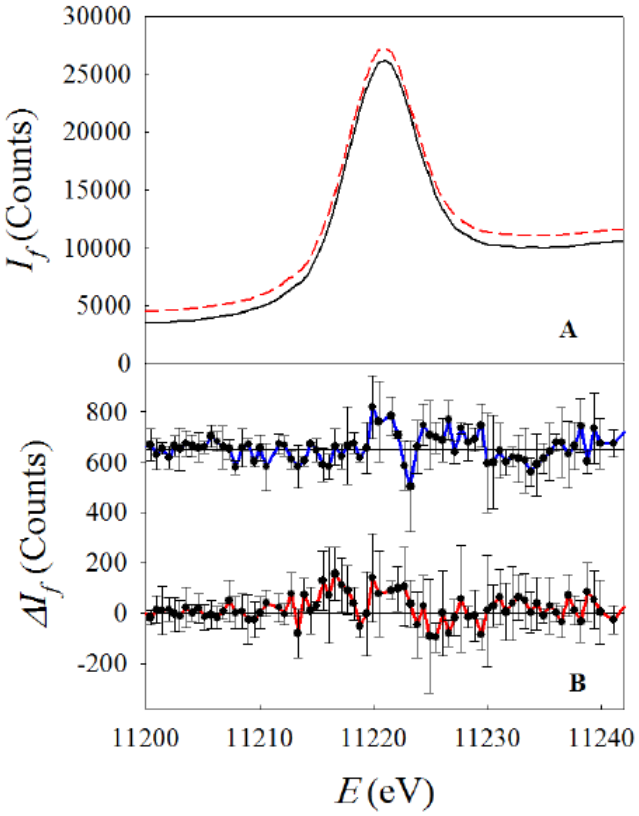

Figure 6.12. A) Average Ir-L_{III} XANNES spectra recorded with (red dotted line) and without (black full line) the activation of the UV pump with a delay of 600 ns between the UV pump and the X-ray probe (the two spectra are shifted along the *y* axis for the sake of better clarity). B) Average (Light-dark) difference signals and corresponding error bars obtained by simultaneous irradiation by UV light and X-rays (blue line) and with a delay of 600 ns (red line). The two signals are shifted along the *y* axis and the zero is indicated by the black horizontal lines. All data were obtained at 1.56 V vs RHE.

Differences between the two spectra are observed in both cases examined. The blue line represents the average (Light – Dark) difference acquired with Δt=0 while the red one represents the average (Light – Dark) difference acquired with Δt=600 ns. In both cases the experimental signal is well above the statistical error and shows an increase with the activation of the UV pump in the energy

range corresponding to the *2p* → *5d* transitions. Looking more closely at the two different signals, it is possible to notice that the application of the delay between the pump and the probe determines a (Light – Dark) difference signal in a wider energy range. Having in mind that XANES is a direct probe for the density of empty states, we can assume a larger number of holes in the *5d* states of iridium under irradiation. The only reasonable explanation to this is the occurrence of a hole transfer between the hematite and iridium in these conditions. Furthermore, when a delay of 600 ns is applied the effect is larger if compared to the case of simultaneous irradiation. This experimental evidence likely accounts for the occurrence of a charge transfer cascade between the semiconductor and the iridium oxide overlayer. As a consequence we can consider IrO_x overlayer as a medium for accumulating photogenerated holes.

In order to further investigate the system in other electrochemical conditions, we chose the potential 1.46 V Vs RHE. The main reason lies in the fact that this value is not far from the previous one but is not characterized by the presence of a net anodic photocurrent. It is important to underline that, in this experimental approach, at least three spectra should be collected to obtain good data. Therefore, because of the time consumption, only two potential values were investigated. Fig. 6.13 illustrates the results obtained without and with the imposition of the 600 ns delay at 1.46 V. The blue line represents the average (Light – Dark) difference acquired with Δt=0 while the red one represents the average (Light – Dark) difference acquired with Δt=600 ns

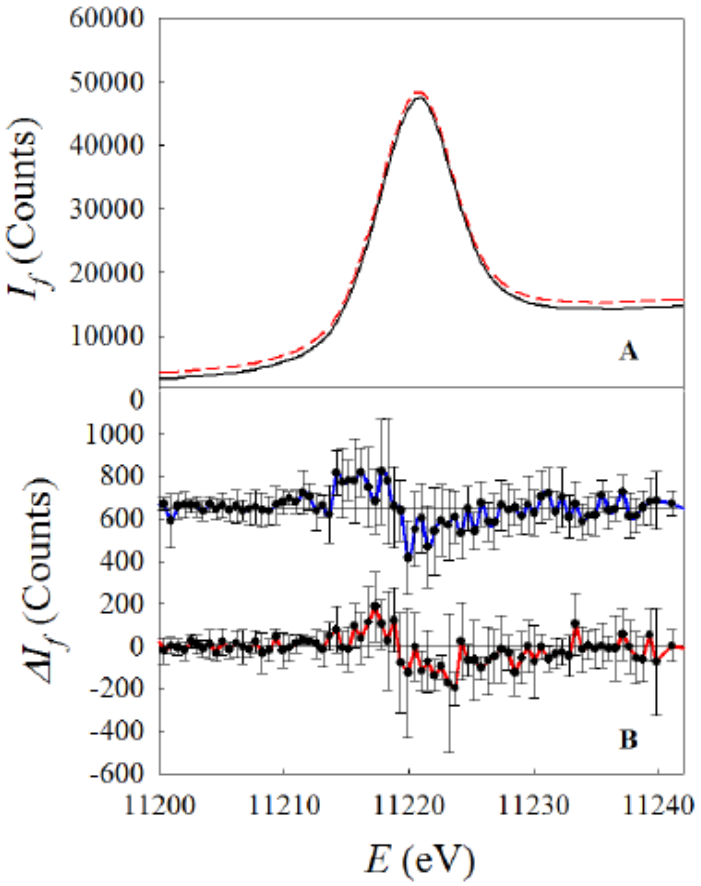

Figure 6.13. A) Average Ir-L_{III} XANNES spectra recorded with (red dotted line) and without (black full line) the activation of the UV pump with a delay of 600 ns between the UV pump and the X-ray probe (the two spectra are shifted along the *y* axis for the sake of better clarity). B) Average (Light-dark) difference signals and corresponding error bars obtained by simultaneous irradiation by UV light and X-rays (blue line) and with a delay of 600 ns (red line). The two signals are shifted along the *y* axis and the zero is indicated by the black horizontal lines. All data were obtained at 1.46 V vs RHE.

Like before, the (light – dark) differences referred to both cases show a statistically significant signal but with a different trend if compared to the previous case. These curves show a positive signal at low energy values (before the edge) and a negative signal at higher energy values. This profile is a clear indication of rigid shift of the spectrum toward lower energy values with the activation of the UV pump. This result should be ascribed to a partial reduction of iridium if subjected to UV irradiation. Additional information can be obtained from the integral curves reported in Fig. 6.14 and indicated by the red lines.

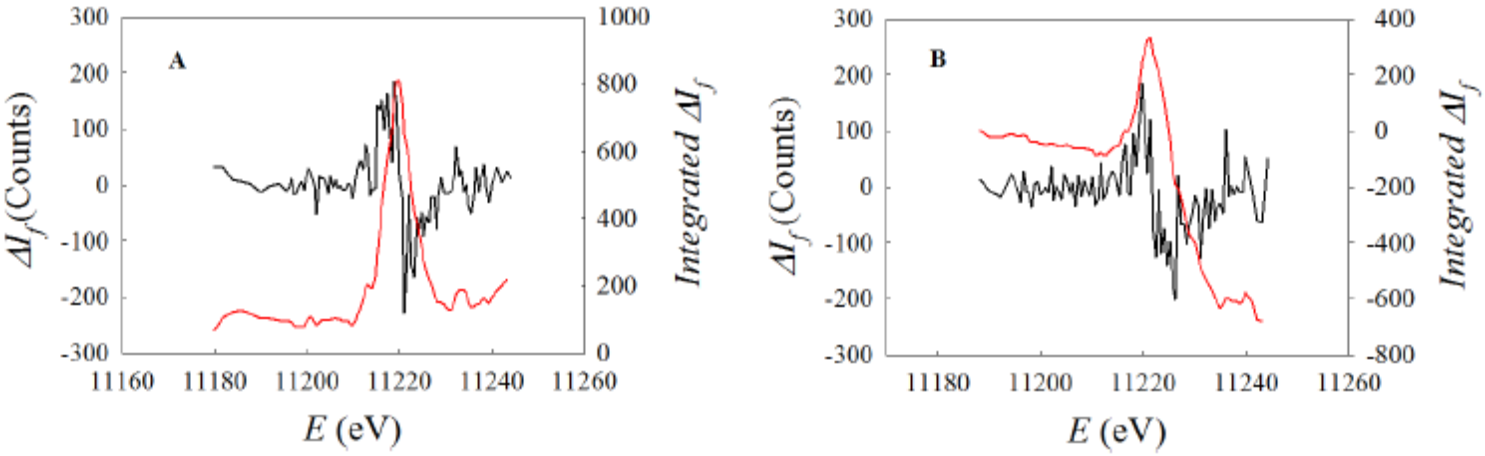

Figure 6.14. (Light-Dark) difference signals (black lines) and corresponding integral curves (red lines) for simultaneous irradiation by UV light and X-rays (A) and for the application of the delay (B)

The trend of the integral curve obtained in the case of simultaneous irradiation by UV light and X-rays (Fig. 6.14.A) is marked by a positive peak in correspondence of the absorption edge: this demonstrates that the positive peak in the difference signal, located between 11210 and 1220 eV, is fully compensated by the negative peak ranging between 11220 and 11230 eV. This curve profile provides further support to the rigid shift of the spectrum under illumination. A different trend of the integral curve can be observed in the case of delay equal to 600 ns (Fig. 6.14.B). Also in this case a positive peak appears at 11220 eV but for larger energy values the signal does not tend to zero but reaches negative values very large in modulus. This trend still accounts for a reduction of iridium under illumination but indicates that the positive part of the difference signal is not fully compensated by the negative one. In other words the area subtended by the positive curve below 11220 eV is much smaller than the area subtended by the negative curve situated above 11220 eV. This can be interpreted by a transfer of spectral weight towards lower energy under illumination by UV light: a reduction in width of the WL is accompanied by a

shift towards lower energy values. A reasonable explanation to this phenomenon can be due to the fact that in absence of delay a fraction of Ir sites are reduced to Ir(III) although the coordination distances and the chemical environment are maintained similar to those typical of Ir(IV). When the UV pump and the probe are delayed of 600 ns, the system has time to relax and reach the typical configuration of Ir(III). This phenomenon can be considered the reason underneath the contraction of the spectrum in correspondence of the WL.

REFERENCES

[1] F. D'Acapito, A. Trapananti, and A. Puri, *J. Phys.: Conf. Ser.* (2016), 712, 012021;

[2] A. Minguzzi, O. Lugaresi, C. Locatelli, S. Rondinini, F. D'Acapito, E. Achilli and P. Ghigna, *Anal. Chem.* (2013), 85, 7009–7013;

[3] M. Barroso, C. a. Mesa, S.R. Pendlebury, a. J. Cowan, T. Hisatomi, K. Sivula, M. Gratzel, D.R. Klug, and J.R. Durrant, *Proc. Natl. Acad. Sci.* (2012), 109, 15640–15645;

[4] A. Minguzzi, O. Lugaresi, E. Achilli, C. Locatelli, A. Vertova, P. Ghigna,and S. Rondinini, *Chem. Sci.* (2014), 5, 3591–3597;

[5] T. Baran, M. Fracchia, A. Vertova, E. Achilli, A. Naldoni, F. Malara, G. Rossi, S. Rondinini, P. Ghigna, A. Minguzzi, and F. D'Acapito *Electrochim..Acta*, (2016), 207, 16—21.

7. $Ni(OH)_2$ / Fe_2O_3 ELECTRODES

The largest part of the most efficient electrocatalysts for the water splitting reaction, is represented by noble metals[1] which are very expensive and not so abundant for a large scale commercial use. In this chapter the attention will be focused onto another cheaper and sustainable electrocatalyst also showing good properties towards the water splitting reaction: nickel hydroxide[2-4]. In particular bilayer photo-electrochemical systems composed of a catalytic domain containing Ni coupled to hematite will be discussed. The electrochemistry of nickel hydroxide involves several phases and the oxidation and reduction processes occur through topochemical reactions leading to amorphous products[5]. In literature we can find much information concerning the very promising catalytic properties of nickel oxide and nickel hydroxide films[2-4,6-8] and the structural features associated to the oxidation/reduction processes of Ni[9-10]. However, nothing is known about the behaviour of nickel hydroxide when coupled to a semiconductor for photo-electrochemical water splitting. Two experiments will be described in this chapter: *(i)* a Ni-K edge XAS investigation and *(ii)* a Fe-K_β edge HERFD-XAS analysis[11]. The purpose is to investigate the variations in the chemical and electronic environment of the materials constituting the bilayer system while applying different photo-electrochemical conditions. For the preparation of the bilayer electrochemical systems see section 3.2..

7.1. Ni-K EDGE: AN *IN SITU* PHOTOELECTROCHEMICAL INVESTIGATION

As a preliminary study, electrodes consisting of only the electrocatalytic domain were investigated. These are constituted of a 80 nm layer of $Ni(OH)_2$. Firstly, a XANES spectrum of the electrode not connected in the electric circuit and in dry conditions (Fig. 7.1.A) was acquired in order to identify the most adequate energy value for the subsequent FEXRAV investigation (Fig. 7.1.B). This was carried out while maintaining the energy fixed to 8350.49 eV, which corresponds to the maximum of the XANES spectrum (marked by the black arrow): any shift of the maximum due to an oxidation process results in a decrease in the absorption coefficient. FEXRAV signal was recorded while applying a CV in the potential range between 1.3 and 1.7 V (Vs RHE), starting from 1.3 V and performing two cycles to check for the reproducibility of the results.

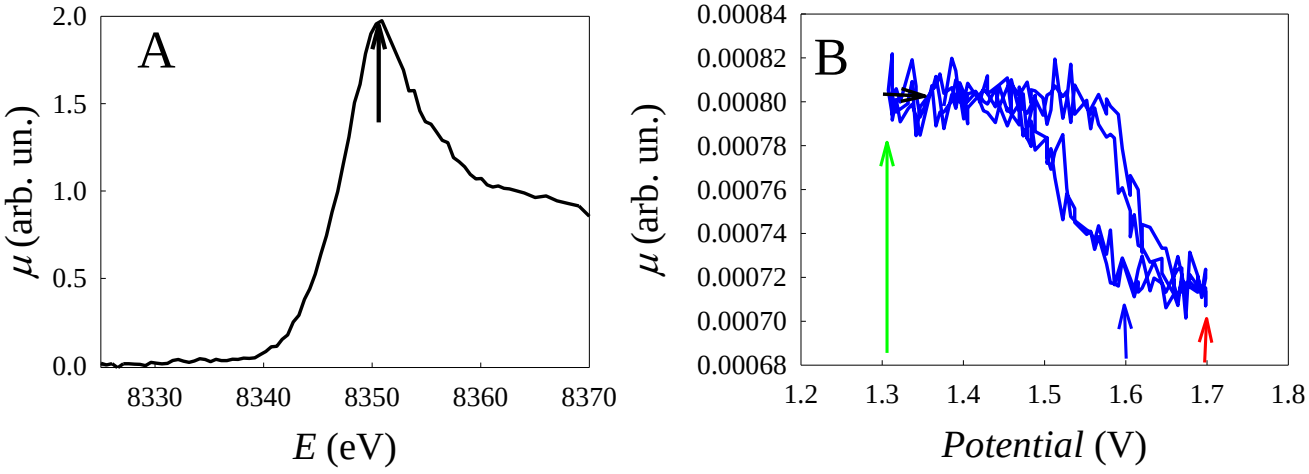

Fig. 7.1. A) Normalized Ni-K edge XANES spectrum of the $Ni(OH)_2$ electrode not connected in the electric circuit and in dry conditions: the arrow marks the energy value chosen for the subsequent FEXRAV analysis. B) FEXRAV signal recorded at *E*: 8350.49 eV while applying a CV in the potential range between 1.3 and 1.7 V (Vs RHE) starting from 1.3 V.

As we can expect, at the beginning of the CV, when the potential is 1.3 V, the absorption coefficient is characterized by its maximum value since Ni is present with oxidation state (II). FEXRAV signal remains constant until potential becomes ca. 1.55 V, then it starts decreasing until ca. 1.65 V when it reaches its lowest value. The three coloured arrows mark the potential values chosen for the subsequent full XAS investigation: green for potential 1.3 V (when μ has its largest value), red for potential 1.7 V (when μ is characterized by the lowest value) and blue for potential 1.6 V (situated in the region of variation). According to electrochemistry at potential 1.7 V water oxidation should begin. Fig. 7.2 presents the three XANES spectra acquired at the three different potential values (A) and the corresponding first derivatives (B).

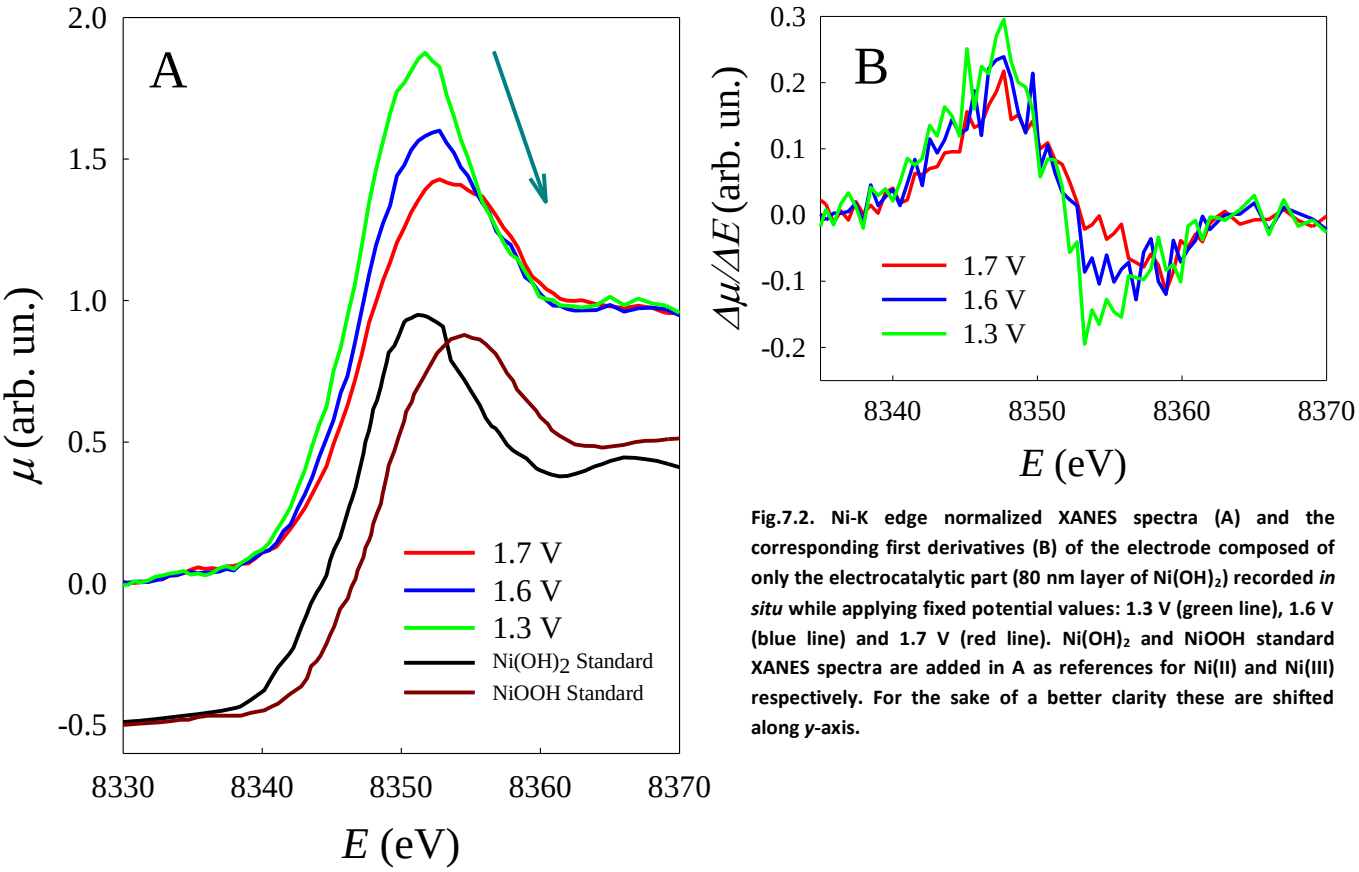

Fig.7.2. Ni-K edge normalized XANES spectra (A) and the corresponding first derivatives (B) of the electrode composed of only the electrocatalytic part (80 nm layer of $Ni(OH)_2$) recorded *in situ* while applying fixed potential values: 1.3 V (green line), 1.6 V (blue line) and 1.7 V (red line). $Ni(OH)_2$ and NiOOH standard XANES spectra are added in A as references for Ni(II) and Ni(III) respectively. For the sake of a better clarity these are shifted along *y*-axis.

The arrow in Fig. 7.2.A evidences the variations detected in the spectra: as the potential increases the maximum decreases in intensity and shifts slightly

towards larger energy values. However, the absorption edge, corresponding to the point of inflection in the spectrum and in the maximum in the derivative, does not change position. A reasonable explanation to this trend can be the fact that only a small part of the photo-absorbers undergoes oxidation since not all the electrocatalytic material participates in the process. $Ni(OH)_2$ and NiOOH standard spectra are added as references and shifted along the *y* axis for the sake of a better clarity. On the basis of the assumption that at 1.3 V all Ni is present with charge state +2, we estimated an oxidation degree for the potentials 1.6 and 1.7 V by performing a linear combination fit of the XANES spectra. This calculation was carried out in the energy range between 8332.8 and 8374.0 eV and the two starting spectra employed in the linear combination are: *(i)* the XANES obtained at 1.3 V (in conditions of reduction), and *(ii)* the XANES of NiOOH standard material. The graphical results are illustrate din Fig. 7.3.

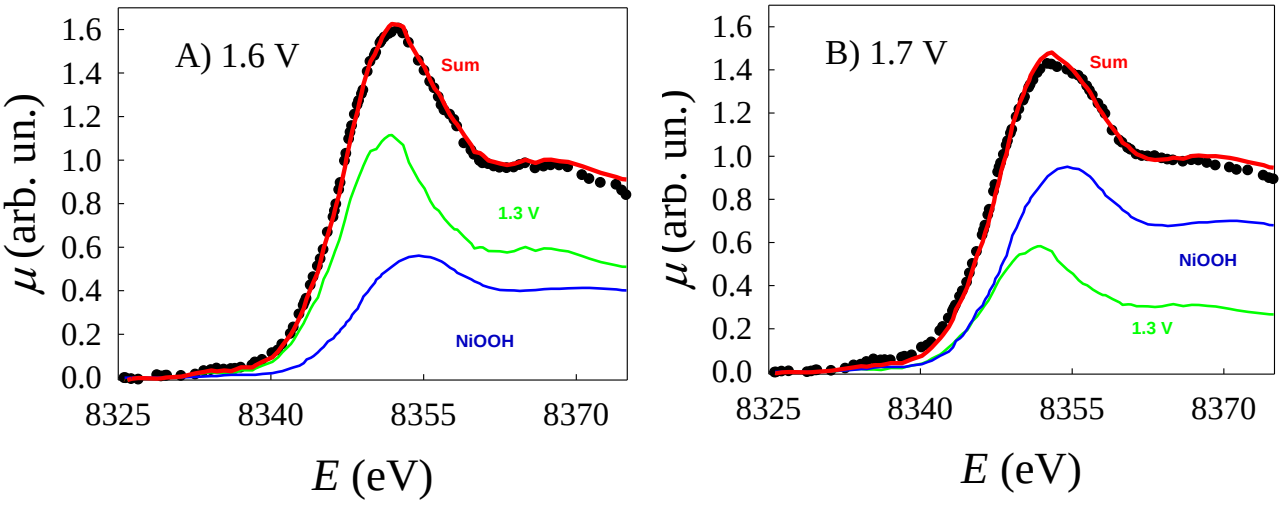

Fig.7.3. Linear combination fit of the Ni-K edge XANES spectra referred to the electrode composed of 80 nm of $Ni(OH)_2$ obtained at 1.6 V (A), and 1.7 V (B). The fit was carried out in the energy range between 8332.8 and 8374.0 eV and the two starting spectra employed in the linear combination are: the XANES obtained at 1.3 V (in reduction conditions) and the XANES of NiOOH standard material.

The parameters arising from the fitting procedure are listed in Tab. 7.1.

Potential	**1.6 V**	**1.7 V**
% XANES spectrum at 1.3 V	59.3(7)	31(1)
% NiOOH standard XANES spectrum	40.7(7)	69(1)
R-factor	0.0004	0.0009

Tab. 7.1. Parameters obtained by the linear combination fit of the spectra illustrated in Fig. 7.3.

The percentages value of the standards employed in the two fits suggest that the charge state of Ni is ca. +2.4 at potentials 1.6 V and ca. +2.7 at potential 1.7 V . When looking at the EXFAS signals at the three different potential values (Fig. 7.4), it is easy to observe that the oscillations recorded at 1.3 V are very similar to those obtained at 1.6 V while the spectrum at 1.7 V is very different. This experimental result suggests that at the applied potential 1.6 V Ni has begun the oxidation process towards Ni(III) but the local chemical environment remains that typical of $Ni(OH)_2$.

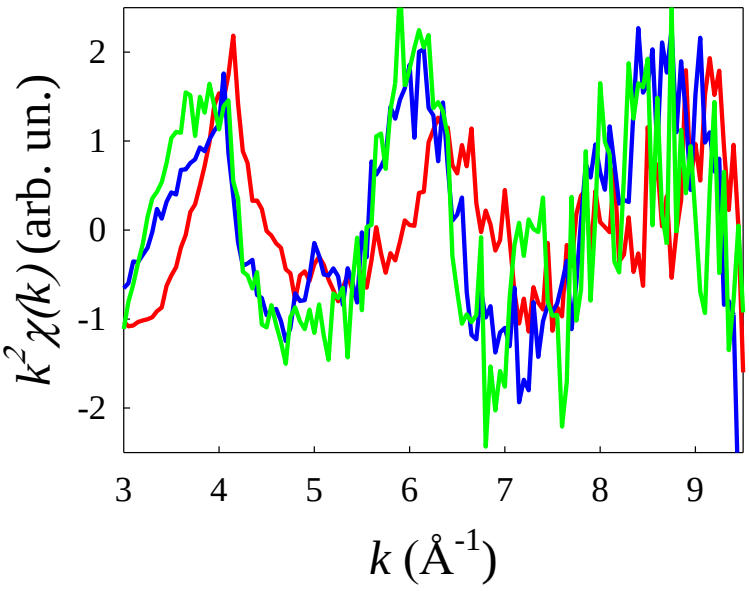

Fig.7.4. Ni-K edge EXAFS signals referred to samples constituted of a 80 nm $Ni(OH)_2$ layer obtained at 1.3 V (green line), 1.6 V (blue line) and 1.7 V (red line).

Let's turn the discussion to the results obtained for the $Ni(OH)_2/Fe_2O_3$ bilayer electrodes (in this experiment we considered electrodes of Type 1 described in section 3.2). The experiments carried out on this kind of sample are aimed at investigating the role of Ni catalyst when coupled to a semiconductor.

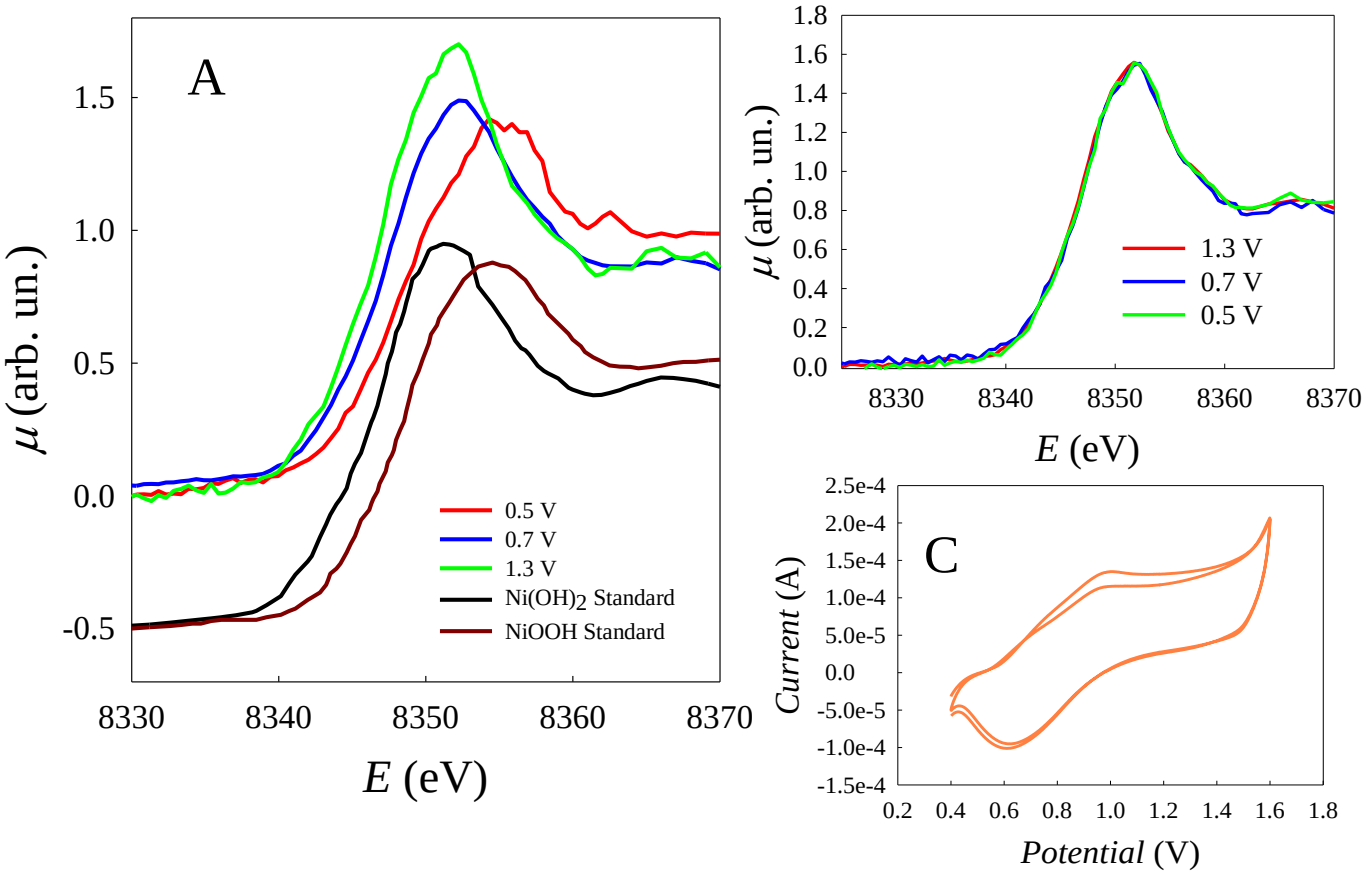

Fig.7.5. Ni-K edge normalized XANES spectra recorded in presence (A) and in absence (B) of UV-Vis irradiation while applying different potentials: 0.5 V (green line), 0.7 V (blue line) and 1.3 V (red line). Ni-K edge normalized standards of Ni(II) (black line) and Ni(III) (brown line) are added for a better reference in A. In order the better visualize the spectra they are shifted along the *y*-axis. C) CV performed in the potential range within 0.5 V and 1.6 V by applying 0.05 V/s under UV-Vis irradiation. Potentials are Vs RHE.

Fig. 7.5 shows Ni-K edge normalized XANES spectra acquired in presence (A) and in absence (B) of UV-Vis irradiation while applying different potentials: 0.5 V (green line), 0.7 V (blue line) and 1.3 V (red line). These values were chosen on the basis electrochemical measurements (Fig. 7.5.C). At first sight it is easy to observe that, when the UV-Vis light source is off, the XANES spectra recorded at the three different potentials are characterized by almost identical spectral profiles, which are very similar to that of $Ni(OH)_2$. Under UV-Vis illumination,

the increase in the potential determines both a shift of the absorption edge towards larger energy values and a modification of the spectral shape. This experimental evidence is a clear proof that the variation of the photo-electrochemical conditions results in a different oxidation state and local structure of the photo-absorber. By observing the shape of Ni-K edge XANES spectra present in literature[3,4,12], we can safely affirm that, under UV-Vis irradiation, Ni is characterized by oxidation state (II) and is present in the form of $Ni(OH)_2$ at 0.5 V, is characterized by oxidation state (III) and is present in the form of NiOOH at potential 1.3 V and is characterized by intermediate oxidation state and local structure at 0.7 V. In order to better perceive the effect of UV-Vis light on the sample, Fig. 7.6 compares the spectrum acquired in dark (blue line) and the one acquired in light conditions (red line) for each applied potential.

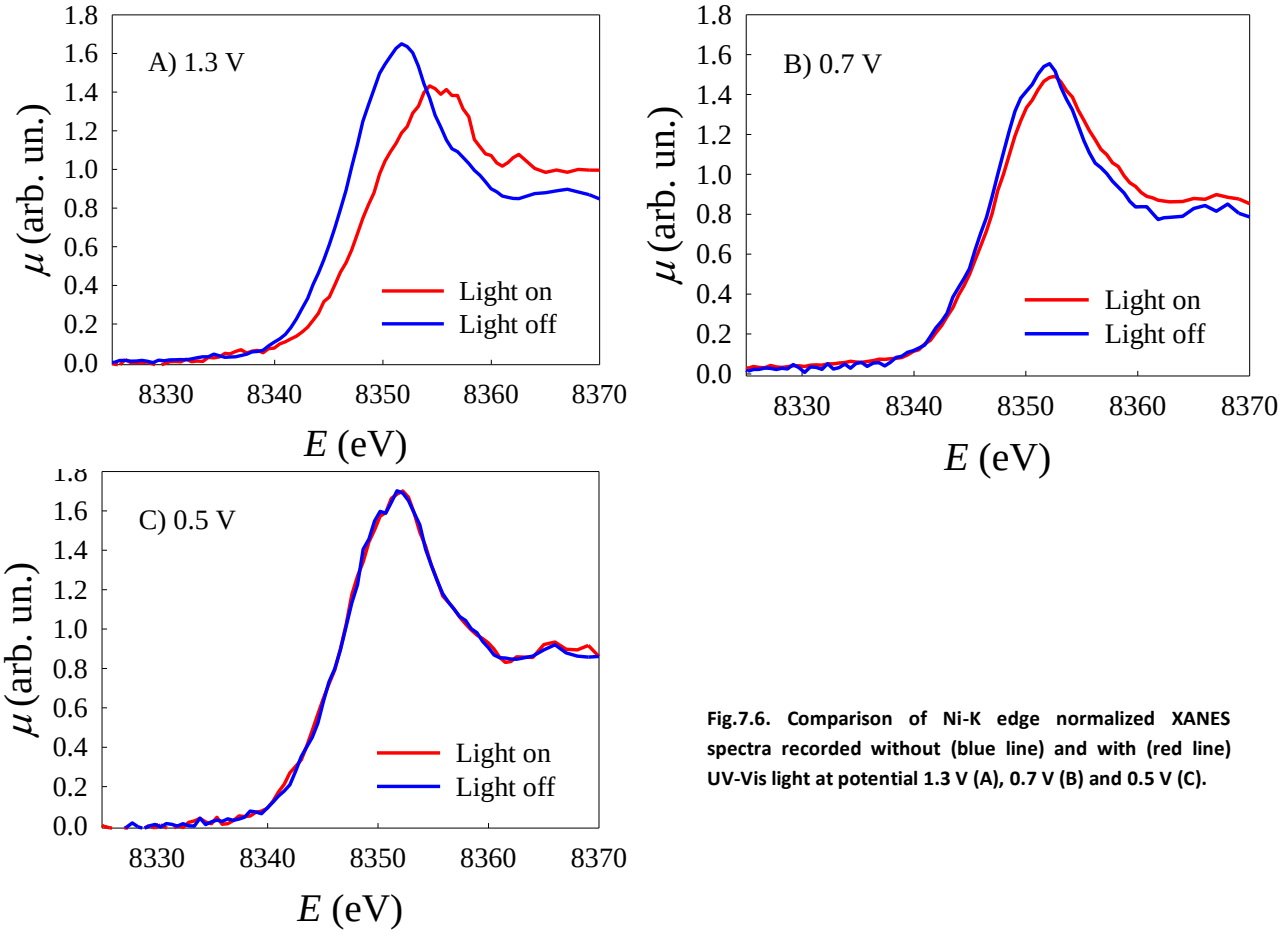

Fig.7.6. Comparison of Ni-K edge normalized XANES spectra recorded without (blue line) and with (red line) UV-Vis light at potential 1.3 V (A), 0.7 V (B) and 0.5 V (C).

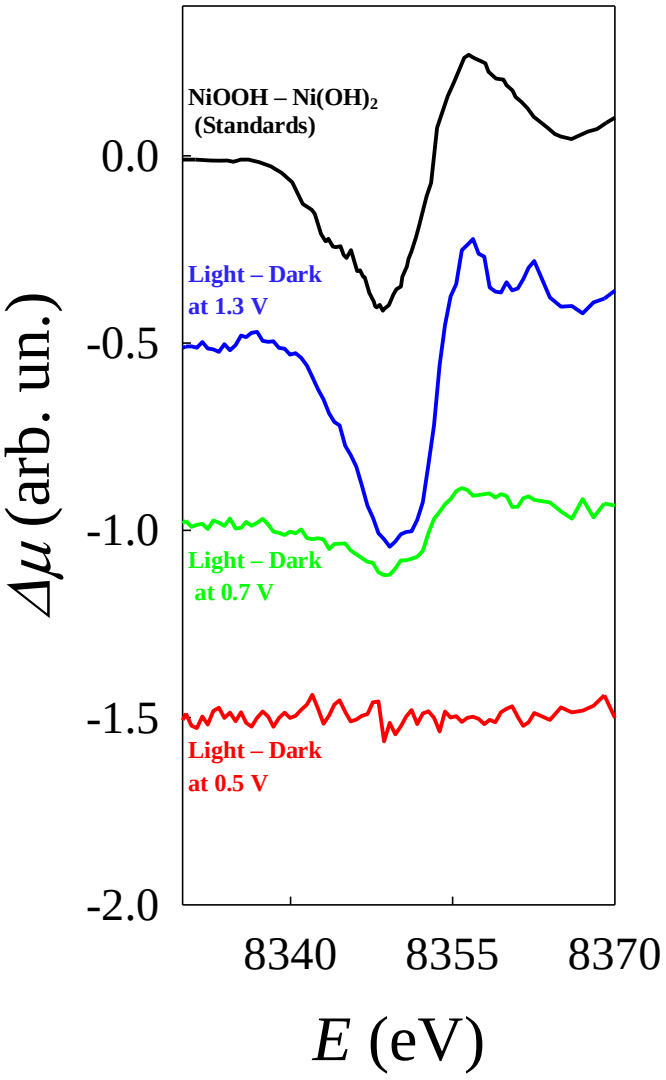

Fig. 7.7. Light-dark difference signals obtained from the normalized XANES spectra at 1.3 V (blue line), 0.7 V (green line) and 0.5 V (red line). The difference signal obtained by subtracting the $Ni(OH)_2$ standard spectrum from that of NiOOH is added as a reference and indicated as a black line.

For each potential value, Fig. 7.7 illustrates the light-dark difference signal calculated: the difference signal obtained by subtracting the $Ni(OH)_2$ standard spectrum from that of NiOOH is added as a reference and indicated as a black line. The difference signal referred to potential 1.3 V shows a great similarity with that arising from the standards both in shape and in intensity: this is in agreement with the previous assumption concerning the oxidation of Ni under UV-Vis irradiation at 1.3 V. This light-dark difference decreases in intensity but is still marked by the same trend at potential 0.7 V and completely disappears at 0.5 V.

In order to quantify the oxidation degree induced by UV-Vis irradiation at each potential value, a linear combination fit by means of ATHENA software[13] was carried out (Fig. 7.8). The fit was carried out in the energy range between 8332.8 and 8374.0 eV and the two starting spectra employed in the linear combination are: *(i)* the XANES obtained at the same potential but without UV-Vis irradiation, *(ii)* the XANES of NiOOH standard material. Tab. 7.2 illustrates the parameters obtained with the fitting procedure. When the applied potential is 1.3 V (Fig. 7.8.A), the XANES spectrum obtained in presence of UV-Vis light is dramatically different from

that obtained at the same potential but in dark conditions and the contribution of NiOOH standard spectrum is equal to 100(2) %. If the applied potential is equal to 0.7 V (Fig. 7.8.B) the percentage of the XANES spectrum at the same potential but in dark conditions is 72(1) % and the percentage of the XANES spectrum of NiOOH standard is 28(1) %. Finally, for 0.5 V (Fig. 7.8.C) the best fit is obtained with 100(1) % of the XANES spectrum at the same potential but in dark conditions.

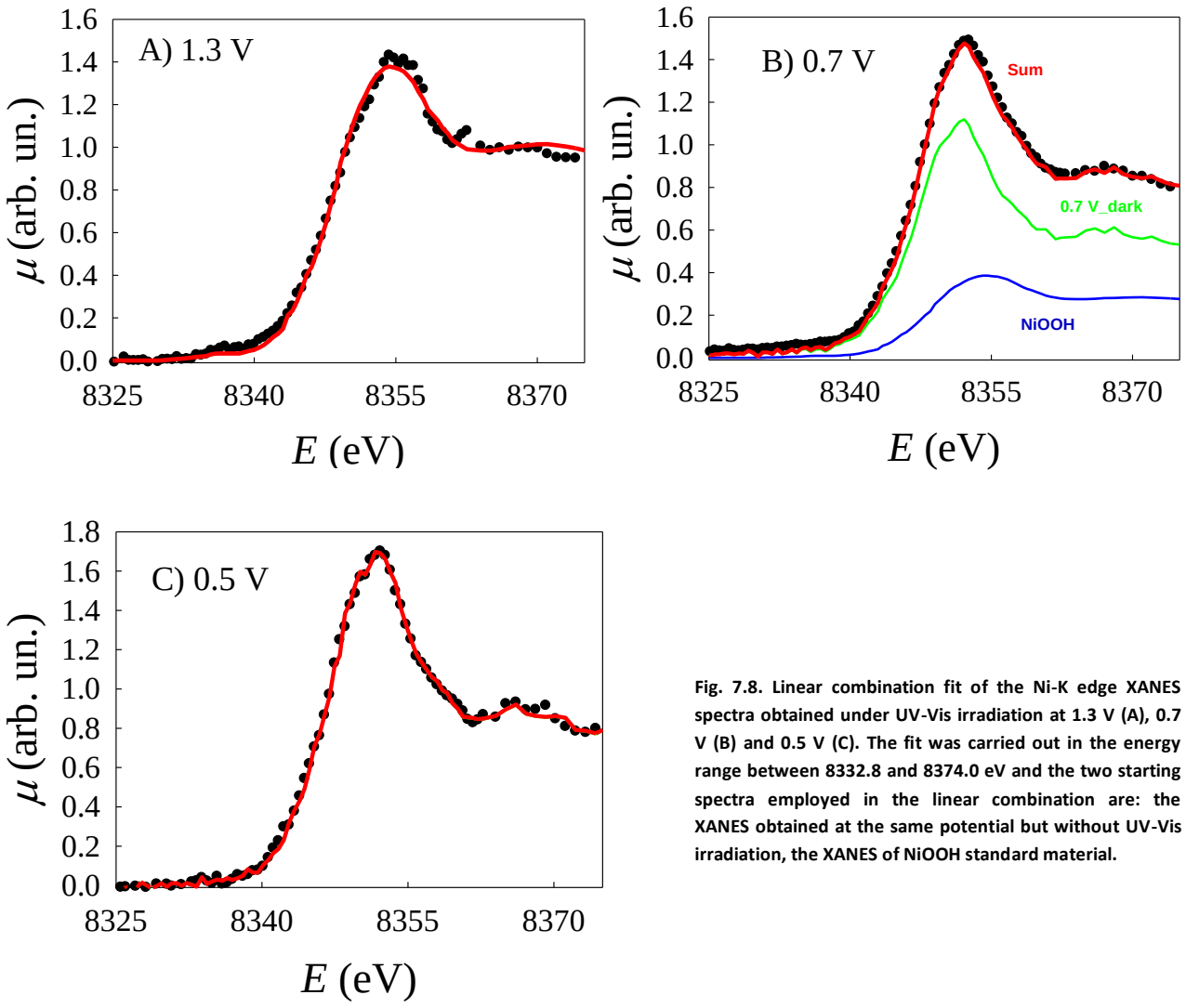

Fig. 7.8. Linear combination fit of the Ni-K edge XANES spectra obtained under UV-Vis irradiation at 1.3 V (A), 0.7 V (B) and 0.5 V (C). The fit was carried out in the energy range between 8332.8 and 8374.0 eV and the two starting spectra employed in the linear combination are: the XANES obtained at the same potential but without UV-Vis irradiation, the XANES of NiOOH standard material.

Potential	**1.3 V**	**0.7 V**	**0.5 V**
% XANES spectrum at the same potential but in dark conditions	0(2)	72(1)	100(1)

% NiOOH standard XANES spectrum	100(2)	28(1)	0(1)
R-factor	0.003	0.0006	0.0007

Tab. 7.2. Parameters obtained by the linear combination fit of the spectra illustrated in Fig. 7.7.

Having in mind that Ni has charge state +2 in $Ni(OH)_2$ and charge state +3 in NiOOH, it is possible to affirm that all Ni is present with charge state +3 at 1.3 V and with charge state +2 at 0.5 V. Furthermore, we can estimate an average charge state of +2.28 for applied potential 0.7 V.

The reproducibility of the results obtained was checked by recording the absorption coefficient μ at a fixed energy value equal to 8349.05 eV (corresponding to the position of maximum contrast) and at potential 1.3 V while applying UV-Vis light off/on cycles. Fig. 7.9 shows the trend of the absorption coefficient during two light off/light on cycles of ca. 500 s: under irradiation the signal assumes a lower value with respect to dark conditions. This is a further experimental evidence of the oxidation of the photo-absorber under UV-Vis irradiation. In addition, the largest and the lowest values are constant in the two cycles and therefore account for the reproducibility of the process.

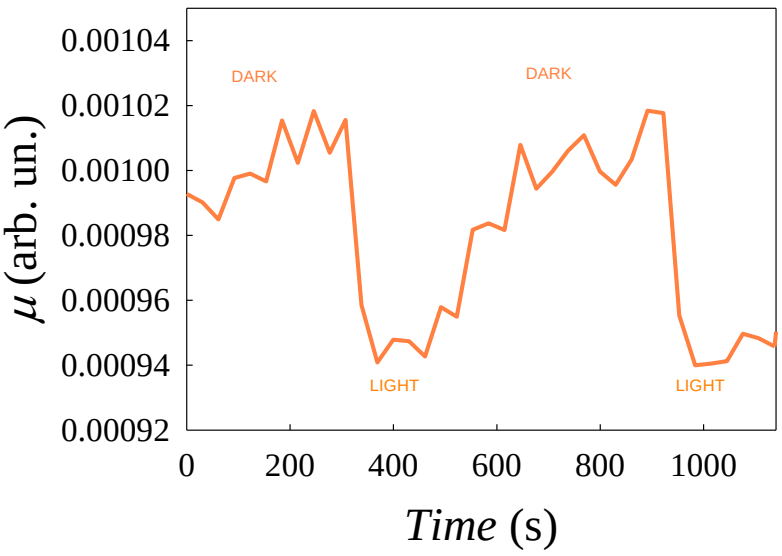

Fig. 7.9. Measure of the absorption coefficient μ at a fixed energy value equal to 8349.05 eV and at potential 1.3 V while applying two UV-Vis light off/on cycles of ca. 500 s each.

7.2. EXPLORING THE K_β OF Fe IN THE HEMATITE

After investigating the effects induced in the nickel hydroxide by the presence of the hematite in the different photo-electrochemical conditions, it is important also to study the influence of the electrocatalytic domain on the semiconductor part. The main properties of *3d* transition metals are associated to the electronic and magnetic structure and can influence the quadrupolar *1s* → *3d* transition[14]. Therefore, by observing the variations in the pre-edge features it is possible to gain important information about the magnetic and structural properties[15].

7.2.1. THE ROLE OF HERFD-XAS

When investigating the pre-edge features at the *K* absorption of transition metals, the main limitations of XAS spectroscopy deal with the *1s* core-hole lifetime of ca. 1.15 eV[15]. Even in presence of a good spectrometer it is not possible to gain a high energy resolution. In addition it is difficult to separate the components due to quadrupolar contribution from those governed by dipolar contribution (generated by *p-d* hybridization and present in non-centrosymmetric structures)[15]. In the experiment described in this chapter, aimed at investigating the local structure of hematite, the lifetime broadening is reduced by recording the X-ray absorption signal of the emitted X-ray fluorescence in a narrow energy bandwidth: this technique is called HERFD-XANES (High Energy Resolution Fluorescence Detected XANES)[16]. In this case the K_β line was employed: it corresponds to final states with unpaired spin in the *3p* shell either parallel or antiparallel with respect to the unpaired spin in the *3d* shell[17]. Fig. 7.10 shows the energy level diagram for the intermediate and final states involved in the electronic transition process.

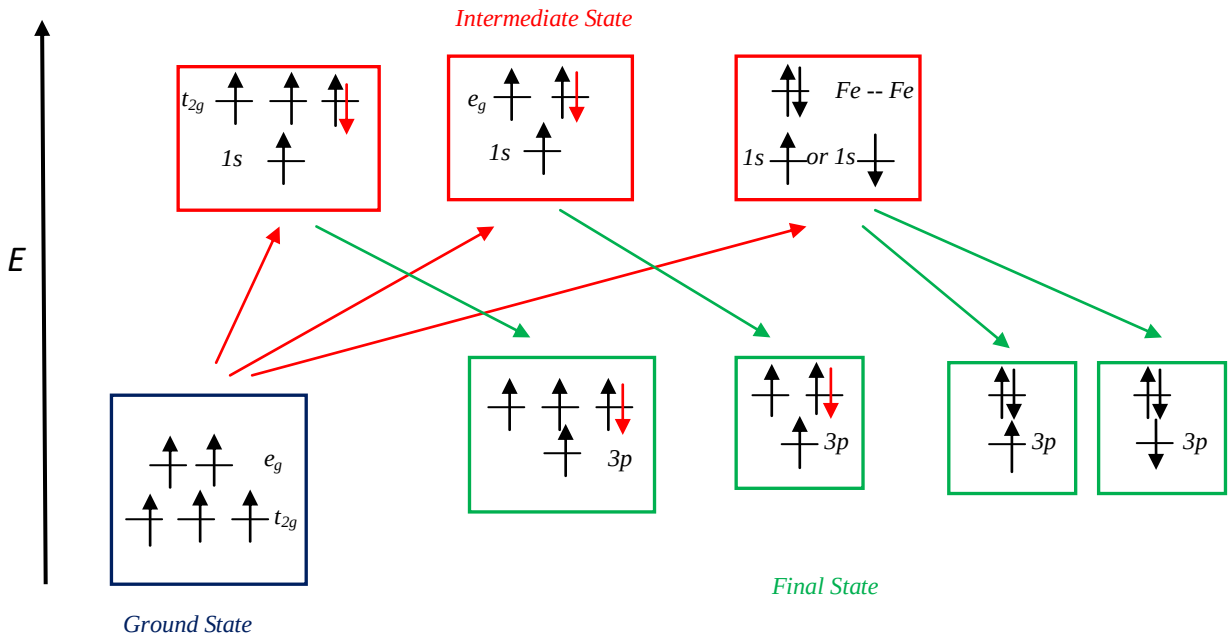

Fig. 7.10. Scheme of the energy levels for *1s3p* HERFD-XAS: O_h symmetry is considered for Fe *3d* states.

The parallel or antiparallel alignment is conserved upon the *3p* → *1s* transition (according to the Δs=0 selection rule neglecting spin-orbit interaction). Therefore, the final states select the spin orientation of the photoexcited electron and, as the *3d* states constitute the conduction band, the spin selective transition can provide information about the magnetic properties of the material.

7.2.2. THE RESULT OBTAINED ON BEAMLINE ID26

The experiment was carried out on beamline ID26[18] at the ESRF. The selection of the incident energy was performed by means of a pair of cooled Si monochromators characterized by an energy bandwidth of 0.5 eV. The incident flux was of the order of 10^{12} photons/s and the beam spot on the sample 0.35 x 1.0 mm. The detector was a Si photodiode. All the spectra were normalized at the *K* edge jump. The electrodes considered in this experiment are of Type 2 (see section 3.2).

The most interesting result obtained is illustrated in Fig. 7.11. This shows the pre-edge features of the HERFD—XAS spectra of three types of electrodes constituted by hematite, not connected in any electrochemical cell nor immersed in any electrolyte: hematite alone (red line), hematite + electrodeposited $Ni(OH)_2$ (blue line) and hematite + photodeposited $Ni(OH)_2$ (green line). The two peaks marked by letters A and B are generated by electronic transitions towards t_{2g} and e_g states respectively while the C and D features are associated to the spin selective transitions to Fe band states[17].

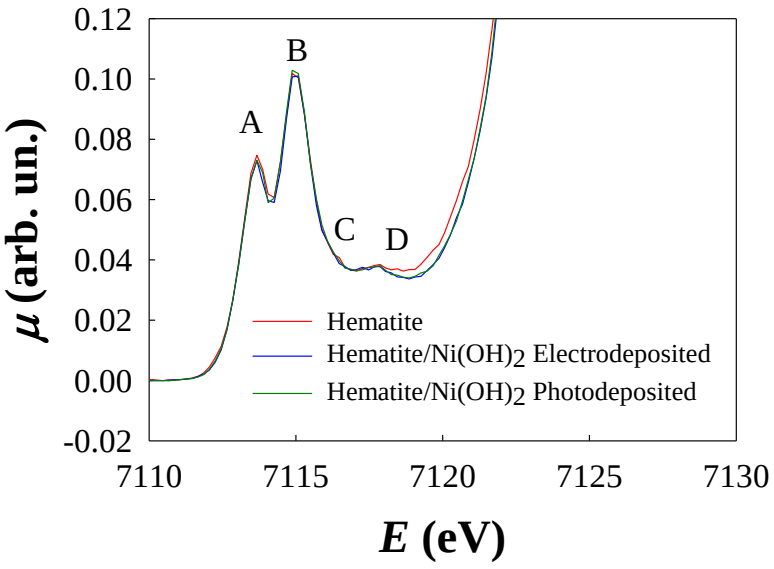

Fig. 7.11. Pre-edge features of the normalized HERFD-XAS spectra of three types of electrodic materials: hematite alone (red line), hematite + electrodeposited $Ni(OH)_2$ (blue line) and hematite + photodeposited $Ni(OH)_2$ (green line).

At first sight it is possible to observe that the pre-edge features referred to the two electrodes containing nickel are almost identical to each other but show a difference if compared to that referred to hematite alone. This difference, which however should be investigated by further analysis, provides a clear experimental evidence that the local structure of Fe in the hematite is influenced by the presence of Ni electrocatalyst. Furthermore, the fact that it is located in correspondence of the spin selective transition makes it reasonable to think that it is due to differences in the magnetic ordering.

In order to validate this assumption rationally, the pre-edge features were fitted by means of ATHENA software[13] using a proper linear combination of Pseudo-Voigt profiles and error functions (Fig. 7.12).

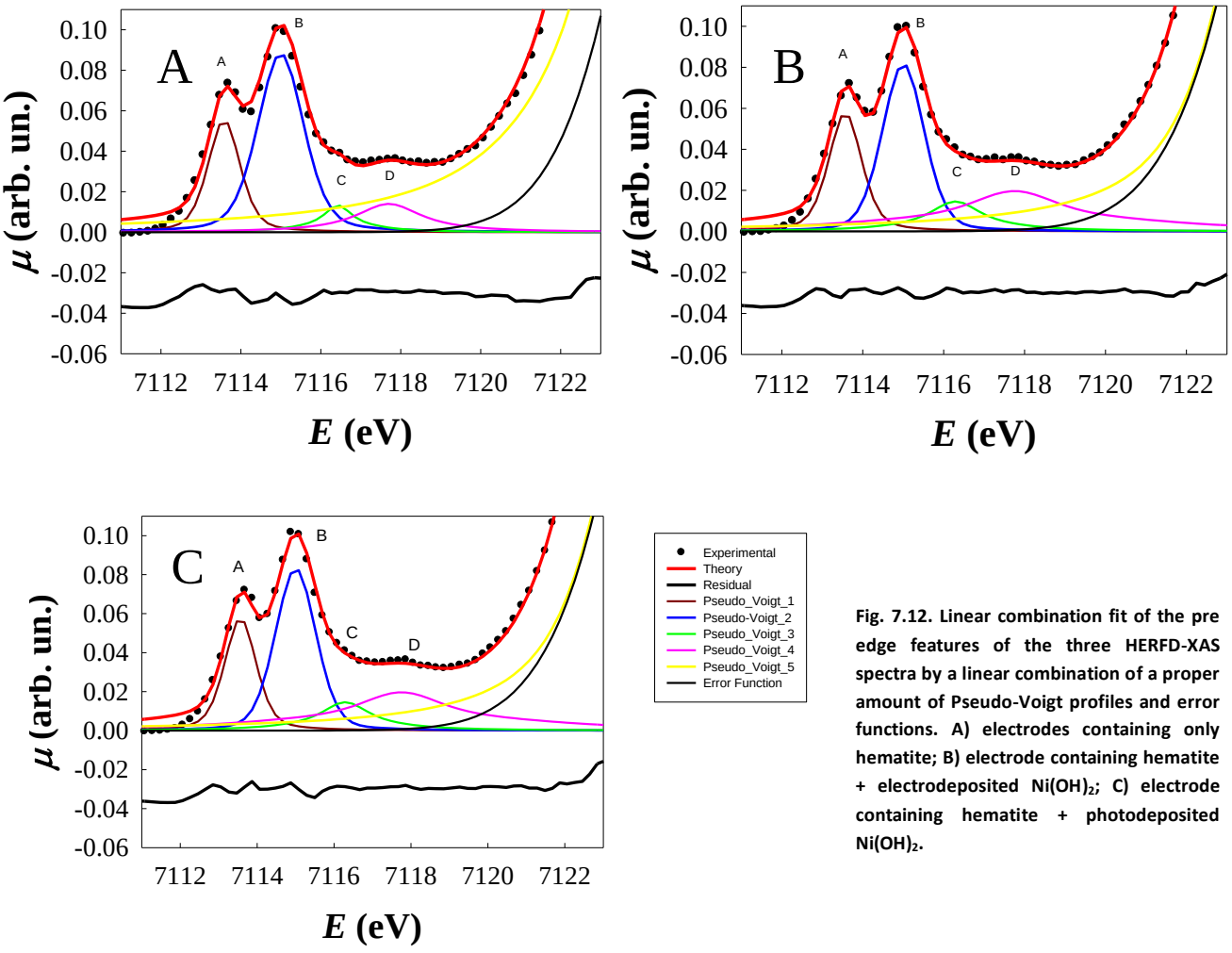

Fig. 7.12. Linear combination fit of the pre edge features of the three HERFD-XAS spectra by a linear combination of a proper amount of Pseudo-Voigt profiles and error functions. A) electrodes containing only hematite; B) electrode containing hematite + electrodeposited $Ni(OH)_2$; C) electrode containing hematite + photodeposited $Ni(OH)_2$.

The most interesting parameters refer to Pseudo-Voigt 3 and 4, associated to the spin selective electronic transitions, and are represented by the Gaussian widths. As we can expect, in presence of bilayer systems we obtain identical values (1.7 and 3.5 eV respectively) different from those obtained for the hematite alone (1.0 and 2.0 eV respectively).

7.3. CONCLUSIONS

The research work presented in this chapter aims at studying the local structure of the materials constituting the $Ni(OH)_2/\alpha$-Fe_2O_3 bilayer architectures in order to clarify the role of nickel electrocatalyst in the photo-electrochemically induced water splitting. The results of two experiments have been illustrated: *(i)* an *in situ* and *in operando* Ni-K edge XAS investigation and *(ii)* a HERFD-XAS analysis at the K_β of Fe.

(i) In the first experiment we acquired XANES spectra while applying different potential values both in presence and in absence of UV-Vis light irradiation. The results obtained pointed out that in dark conditions the spectral shape remains the same at the different potentials whereas in light conditions an increase in the potential value determines an oxidation of Ni. The reproducibility of these results was demonstrated. The oxidation degree is much more if compared to the response obtained in presence of electrodes containing only $Ni(OH)_2$. This accounts for the occurrence of a bulk process. On the basis of fitting procedures it was possible to estimate a charge state for Ni at the different applied potentials: +3 at 1.3 V, +2 at 0.5 V and +2.28 at 0.7 V. It is reasonable to conclude that, under UV-Vis irradiation and in presence of a sufficiently large potential, a hole transfer occurs from hematite to nickel, causing Ni to pass from oxidation state (II) to oxidation state (III):

$$Ni^{II} - OH \rightarrow Ni^{III} - O + H^+ \quad (7,1)$$

Then it promotes oxygen evolution:

$$H_2O + 2NiOOH \rightarrow 2Ni(OH)_2 + \frac{1}{2}O_2 \quad (7,2)$$

The process described by Eq. (7,1) is notably faster than that described by Eq. (7,2).

(ii) The second experiment allowed to take advantage of a high resolution X-ray absorption technique to compare the local electronic environment of Fe in the hematite in presence of the $Ni(OH)_2$ layer to that in absence of the $Ni(OH)_2$ layer. By observing the differences in the pre-edge features, we can safely affirm that the presence of Ni electrocatalyst influences the local electronic environment of hematite. Even though a further investigation is needed, a reasonable explanation deal with the presence of different magnetic orderings in the different electrodes.

REFERENCES

[1] J. O'M. Bockris, A. K. N. Reddy, M. Gamboa-Aldeco, Modern Electrochemistry 2A, 2nd ed.; Kluwer Academic/Plenum Publishers: New York, 1998;

[2] C. He, X. Wu, and Z. He, J*. Phys. Chem. C* (2014), 118, 4578—4584;

[3] J. McBreen, W. E. O'Grady, K. I. Pandya, R. W. Hoffman, and D. E. Sayers, *Langmuir* (1987), 3, 428-433;

[4] Y. Hu, I. T. Bae, Y. Mo, M. R. Antonio, and D. A. Scherson, Can. J. Chem. (1997), 75, 1721—1729;

[5] H. Bode, K. Dehmelt, and J. Witte, Electrochim. Acta (1966), 11, 1079—1087;

[6] R. L. Doyle, I. J. Godwin, M. P. Brandon, and M. E. G. Lyons, M, Phys. *Chem. Chem. Phys.* (2013), 15, 13737–13783;

[7] M. Cappadonia, J. Divisek, T. von der Heyden, and U. Stimming, *Electrochim. Acta* (1994), 39, 1559–1564;

[8] M. Dinca, Y. Surendranath, and D. G. Nocera, *Proc. Natl. Acad. Sci. U.S.A.* (2010), 107, 10337–10341;

[9] A. J. Tkalych, K. Yu, and E. A. Carter, J. Phys. Chem. C (2015), 119, 24315—24322;

[10] K. I. Pandya, W. E. O'Grady, D. A. Corrigan, J. McBreen, and R. W. Hoffman, J. Phys. Chem. (1990), 94, 21—26;

[11] M. Bauer, *Phys. Chem. Chem. Phys.* (2014), 16, 13827—13837;

[12] A. N. Mansour, C. A. Melendres, M. Pankuch, and R. A. Brizzolara, *J. Electrochem. Soc.* (1994), 141, 69—71;

[13] B. Ravel, and M. Newville, *J. Synchrotron Radiat.* (2005), 12, 537– 541;

[14] G. Dräger, R. Frahm, G. Materlik, and O. Brümmer, *Phys. Status Solidi B* (1988), 146, 287;

[15] J.-P. Rueff, L. Journel, P.-E. Petit, and F. Farges, *Phys. Rev. B.* (2004), 69, 235107;

[16] P. Glatzel, T._C. Weng, K. Kvashnina, J. Swarbrick, M. Sikora, E. Gallo, N. Smolentsev, and R. A. Mori, *J. Electron Spectrosc.* (2013), 188, 17—25;

[17] P. Glatzel, A. Mirone, S. G. Eeckhout, and M. Sikora, *Phys. Rev. B* (2008), 77, 115133;

[18] http://www.esrf.eu/UsersAndScience/Experiments/EMD/ID26.

8. Cu_2O OVERLAYERS: THE STRUCTURE AND STABILITY OF THE PRECURSOR

Copper(I) oxide is considered one of the most important candidates for solar energy conversion devices[1]. Among the main reasons behind the attention that this material has attracted, we should remember its low cost, non-toxicity and electronic properties. The main advantage is represented by the value of the band gap, ranging from 1.96 to 2.38 eV[2]: these values lie in the acceptable range needed for photovoltaic applications. Furthermore, Copper(I) oxide is a *p*-type semiconductor characterized by resistivity varying from a few Ω cm to 10^{14} Ω cm[1], depending on the preparation method. Different are the techniques employed to obtain Cu_2O: thermal oxidation[3], chemical oxidation[4], anodic oxidation[5], vacuum evaporation[6] and electrochemical deposition[7]. One of the cheapest and most wide-spread procedures for preparing Cu_2O films is represented by the electrolization of an alkaline solution containing copper sulphate, in which a large excess of lactate ions prevents the precipitation of copper oxides/hydroxides[8]. On the base of solid structure determination, lactate ions (L) are thought to from a complex with copper characterized by a 1:2 (Cu:L) stoichiometry[9], but not direct information is at present available. The experiment described is devoted to the investigation of the structure and the stability of a copper(II) lactate complex in an alkaline solution (the preparation is described in section 3.3) by means of dispersive-XANES spectroscopy and XANES simulation.

8.1. XANES THEORY

The base of XANES theory lies in the Fermi's *Golden Rule*, according to which the X-ray Absorption coefficient is given by:

$$\mu(E) = 4\pi^2 \alpha\omega \sum_f |\langle i|\boldsymbol{A} * \boldsymbol{p}|f\rangle|^2 \delta(E - E_f) \tag{8,1}$$

Where $E = \hbar\omega - E_i$ is the photoelectron energy, $\boldsymbol{A}*\boldsymbol{p}$ is the coupling to the X-ray field with vector potential $\boldsymbol{A}$, and the sum refers to unoccupied final states[10]. $\alpha(\cong \frac{1}{137})$ is the fine structure constant and ω is the X-ray energy. The initial state i is defined *core level* and can be considered insensitive to the chemical environment. The excited state f corresponds to an X-ray core-hole and presents a width Γ of several eV. The edge structures can be viewed as the convolution of the final states and Γ. Γ broadening can be viewed as:

$$\Gamma(E) = \frac{\hbar}{\lambda(E)} \sqrt{\frac{2E}{m}} \tag{8,2}$$

The spatial and energy dependence of the electron *DOS* can be expressed in terms of the one-electron Green's function operator:

$$G = [E - H]^{-1} \tag{8,3}$$

with H: effective one-electron Hamiltonian and E: photoelectron energy. The total *DOS* $\rho(E)$ for real energies can be obtained from the integral of $Im\ G$ in position space[11]:

$$\rho(\boldsymbol{r}) = -\frac{2}{\pi} Im \int_{-\infty}^{E_f} dE G(\boldsymbol{r}, \boldsymbol{r}, E) \tag{8,4}$$

In terms of G the absorption coefficient becomes:

$$\mu(E) \sim -\frac{1}{\pi} Im \langle i | \hat{\boldsymbol{\varepsilon}} \cdot \boldsymbol{r}' G(\boldsymbol{r}', \boldsymbol{r}, E) \hat{\boldsymbol{\varepsilon}} \cdot \boldsymbol{r} | i \rangle \tag{8,5}$$

In the Multiple Scattering (MS) theory the propagator can be factored:

$$G(\boldsymbol{r}', \boldsymbol{r}, E) = \sum_{L,L'} R_L(\boldsymbol{r}) G_{L,L'} \cdot R_L \cdot (\boldsymbol{r}') \tag{8,6}$$

Furthermore, the matrix $G_{L,L'}$ can be re-expressed as a sum of all the MS paths that a photoelectron can cross from the absorbing atom and back.

Recently, fitting procedures of the XANES region, from the edge up to 200 eV above it, have been applied to several systems[12]. These methods are based on the comparison between the experimental data and theoretical simulations and the fit is performed by varying selected structural parameters starting from a proposed structure present in literature and characterized by a well defined geometrical local arrangement. The method employed for the analysis of the data collected in the experiment described in this chapter are based on the Full Multiple Scattering (FMS) calculations[13].

In the EXAFS region the absorption coefficient can be expressed in terms of Single Scattering approximation as follows:

$$\mu(k) = \mu_0(k)[1 + \chi_2(k)] \tag{8,7}$$

In which $\mu_0(k)$ represents the atomic absorption coefficient and $\chi_2(k)$ is the EXAFS function, calculated on the basis of scattering paths of order 2 (Single Scattering paths).

Taking into account the Multiple Scattering effects (Fig. 8.1), Eq. (8,7) becomes:

$$\mu(k) = \mu_0(k)\left[1 + \sum_{n=2}^{\infty} \chi_n(k)\right] \tag{8,8}$$

Where $\chi_n(k)$ indicates the contribution to the absorption coefficient due to the scattering paths of order n and can be expressed as[12]:

$$\chi_n(k) = \sum_{p_n} A_n(k, p_n) sin\left[kR_{p_n} + \phi(k, p_n) + 2\delta\right] \tag{8,9}$$

The sum is calculated over all possible paths p_n of order n and R_{p_n} is the corresponding path length. A_n and ϕ are quantities that depend upon the potential affecting the photo-electron.

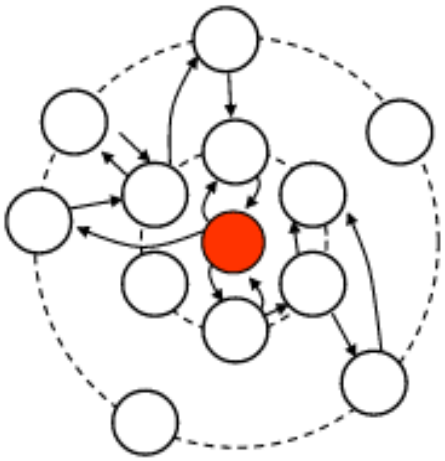

Figure 8.1. Scheme of possible Multiple Scattering paths occurring between the photo-absorber atom (red circle) and the backscattering atoms (white circles).

According to the relative contribution of the *n*-order of the paths, it is possible to roughly divide the absorption spectrum in three regions[12]:

(i) A Full Multiple Scattering (FMS) region, generally 20/40 eV within the absorption edge, where the scattering power of the environment is strong enough to scatter the photo-electron many times. In principle, in this region an infinite number of paths contribute to the spectrum profile which provides information about the point group symmetry.

(ii) An Intermediate Multiple Scattering (IMS) region, situated between 30 and 200 eV above the edge, in which only a limited number of paths of low order contribute to the convergence of the series in Eq. (8,7). From this region it is possible to obtain information about bond lengths and on angles between bonds.

(iii) A Single Scattering (SS) region, extending beyond 200 eV from the absorption edge, in which all the paths characterized by $n > 2$ are negligible. Thanks to the features of the spectral profile in this region it is possible to investigate the relative positions of the central atoms and of the backscatterers.

In the following parts, Cu-K edge XANES sipectrum of the copper(II) lactate is investigated in order to gain a deeper understanding about the local geometric structure of copper in the complex. The experimental signal is compared to theoretical simulations obtained on the base of the FMS approach. Calculations are performed up to 60/70 eV over the absorption edge by means of EXCURVE code[14]. The simulation is obtained through the use of the exact calculation of the scattering path operator.

8.2. THE EXPERIMENT ON ID24 BEAMLINE

X-ray Absorption measurements were performed on ID24 beamline[15,16] (ESRF) at the Cu-K edge in the transmission mode. The X-ray source consists of two ondulators whose gaps were adjusted in order to tune constant counts of the first harmonic for energies around the Cu-K edge. The horizontal beam focusing was achieved with a curved polychromator (a Si(111) crystal) in Bragg geometry whereas the vertical beam focusing was achieved by means of a bent Si mirror at a glancing angle of 2.5 mrad with respect to the direct beam. As far as the beam size is concerned, the dimensions are 8 μm FWHM horizontally and 80 μm FWHM vertically. This setup ensures a photon density which preserves the sample from damaging. Furthermore, the curved geometry allows the polychromator to pass a broad band of energy through the sample and to diverge towards a linear photodiode array detector (FreLonCCD camera[17]), where the beam position can be correlated to the energy. Thanks to this experimental setup it was possible to perform time resolved measurements.

The spetcroelectrochemical device employed in this experiment is a cell designed and built by means of a 3D printer[18]. Fig. 8.2.A provides a scheme of the main components of the electrochemical device. This consists of two parts: a polycarbonate disc (1) and a Teflon hollow cylinder (characterized by 21 nm

diameter, 6 mm thickness and 7 mm cavity (4)). The working electrode (2) is held between the main body of the polycarbonate disc, through the use of an o-ring (3), and the Teflon plate (which presents a hole allowing the X-rays to pass). Furthermore, it can host a Pt counter electrode and a Ag/AgCl reference electrode. This can be hold between the two sides of the device. The reference electrode can be separated from the solution by means of a salt bridge made of a glass pipette filled with agar containing 0.2 M aqueous $KClO_4$. Fig. 8.2.B shows an image of the electrochemical device with the three-electrodes setup, mounted in the experimental hutch of beamline ID24.

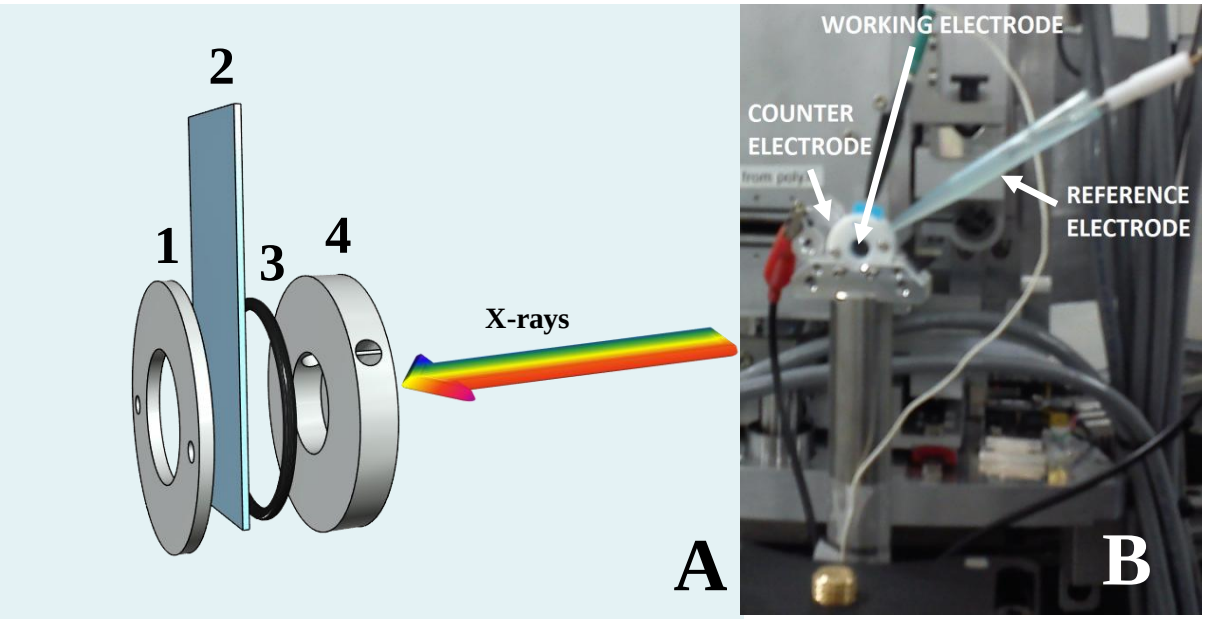

Figure 8.2. Illustration of the 3D printed spectro-electrochemical cell. (A): schematic representation of the two sides (1,4), the working electrode (2) and the O-ring (3). (B): image of the cell with the three electrodes set up, mounted in the beamline hutch.

XAS data were recorded *in operando* in order to investigate both the structure of copper(II) lactate complex in the solution and the solution stability. Two kinds of measurements were performed during this experiment: *(i)* the recording of a single XAS spectrum, in order to gain information about the local geometric structure of copper(II) lactate complex in aqueous solution, and *(ii)* the

acquisition of a sequence of XAS spectra in order to study the stability of copper(II) lactate solution. The SPEC software, at the basis of the control system, allowed to select both the integration time and the number of accumulations for each acquisition. Copper(II) lactate was investigated recording a spectrum resulting from an integration time of 500 ms. The stability of the solution of the complex was studied by recording a sequence of spectra while applying a Linear Sweep Voltammetry (LSV). In this case the acquisition consisted in 320 spectra characterized by an integration time of 500 ms each for a total time of 160 s. These values were chosen as good compromise in order to avoid saturation and to obtain an adequate signal to noise ratio.
The LSV was performed from 1.2 to -0.4 V (Vs Ag/AgCl) and was controlled by means of a potentiostat (a CH instrument 630D).

8.3. *Ab Initio*-XANES, EXAFS AND THE STRUCTURE OF COPPER(II) LACTATE COMPLEX

The analysis of Cu(II) copper lactate XAS spectra is based on three main steps: *(i)* preliminary processing and data extraction (by means of PyMCA[19] and PRESOPRONTO[20] codes), *(ii)* EXAFS fitting and *(iii)* XANES theory calculation. In the investigation of aqueous complexes, only a very small number of *ab-initio* XANES calculations have been performed so far, compared to qualitative interpretations of XANES spectra[21-25]. The main reason lies in the difficulty of the theoretical treatment required.
In order to validate the *ab-initio* XANES simulation procedure employed, a calculation of the Cu-K edge XANES spectrum of a 0.1 M solution of $CuSO_4 \bullet 6H_2O$ standard was performed. Because of the high exchange rate of water molecules and thus the difficulty in obtaining good theoretical simulations[26,27], Cu(II) hydrated ion is an excellent test system for our XANES

fitting approach. Fig. 8.3 illustrates the comparison between the experimental spectrum (blue dots) and the theoretical simulation obtained for three different local geometries: *(i)* a distorted octahedral geometry (red line), *(ii)* a square-pyramidal arrangement (green line) and *(iii)* a trigonal bipyramidal arrangement (orange line).

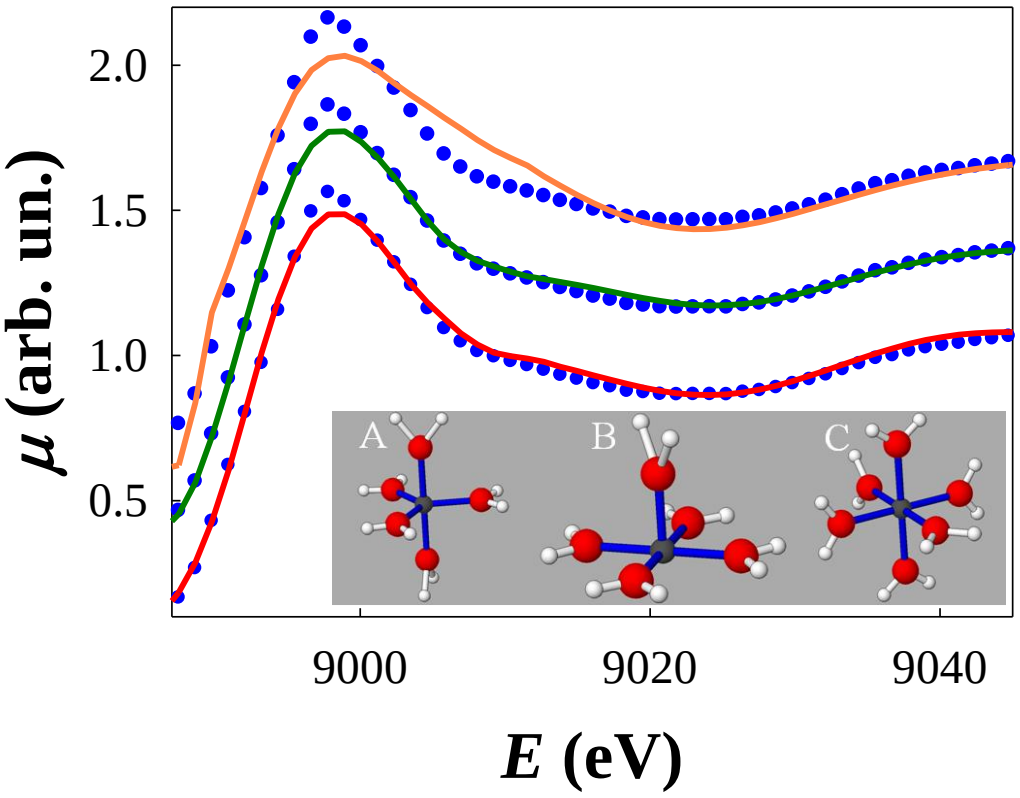

Figure 8.3. Cu-K edge XANES simulations of Cu(II) aquoion. The blue spots represent the experimental signal while the coloured lines are the theoretical calculations based on a trigonal bipyramidal local arrangement (orange line), on a square pyramidal local arrangement (green line) and on a distorted octahedral local arrangement (red line). The insight provides a scheme of the three clusters employed: A) trigonal bipyramidal, B) square pyramidal and C) distorted octahedral.

We can observe that very good simulations are obtained employing the distorted octahedral and the square pyramidal models whereas large discrepancies arise if the trigonal bipyramidal model is used. These results, showing the sensitivity of XANES spectrum to local geometry, are in good agreement with recent literature[28], in which the most probable structures for the Cu(II) hydrated ion

are the distorted octahedral and the square pyramidal ones. The best fitting parameters are listed in Tab. 8.1.

Simulation 1. Distorted Octahedral Arrangement					
Shell	**Coordination Number**	**Type of atom**	**Distance from Cu(II) (Å)**	**σ^2 (Å^2)**	**β (Å^3)**
1	4	**O**	1.97(2)*	4(2) x 10^{-3}*	--
2	2	**O**	2.09(3)*	7(7) x 10^{-3}*	-1.1(3)*
3	8	**H**	2.664	5.0 x 10^{-3}	--
4	4	**H**	3.050	5.0 x 10^{-3}	--
Goodness of Fit *F*: 0.028 %					
Simulation 2. Square Pyramidal Arrangement					
Shell	**Coordination Number**	**Type of atom**	**Distance from Cu(II) (Å)**	**σ^2 (Å^2)**	**β (Å^3)**
1	4	**O**	1.90(3) *	3(4) x 10^{-3}*	-0.4(2)
2	1	**O**	1.90(8)*	1(1) x 10^{-2}*	-2(1)
3	8	**H**	2.664	5.0 x 10^{-3}	--
4	2	**H**	3.050	5.0 x 10^{-3}	--
Goodness of Fit *F*: 0.028 %					
Simulation 3. Trigonal Bipyramidal Arrangement					
Shell	**Coordination Number**	**Type of atom**	**Distance from Cu(II) (Å)**	**σ^2 (Å^2)**	**β (Å^3)**
1	3	**O**	1.91(5)*	1(1) x 10^{-2}*	--
2	2	**O**	1.97(6)*	1(2) x 10^{-2}*	--
3	6	**H**	2.642	5.0 x 10^{-3}	--
4	4	**H**	3.050	5.0 x 10^{-3}	--
Goodness of Fit *F*: 0.14 %					
* Fitted values					

Table 8.1. XANES Calculation parameters of the simulations obtained for the three different geometries. For each shell is reported the coordination number, the type of atom, the distance from the photo-absorber, the thermal disorder (σ^2) and the Skewness (β) when different from zero.

These results can be considered in quite good agreement with those found in literature[26,29-32]. It is important to observe that, in some cases, the addition of the 2nd order cumulant (most commonly known as *skewness*) was necessary in order to improve the Goodness Of Fit. Furthermore, we note an excellent

agreement between experimental signal and theoretical simulation: this is far better than any other that can be found in literature.

Let us now turn to the discussion of the X-ray Absorption Spectra referred to the copper(II) lactate complex in alkaline solution. The Cu-K edge EXAFS signal (A) and the corresponding Fourier Transform (B) are reported in Fig. 8.4.

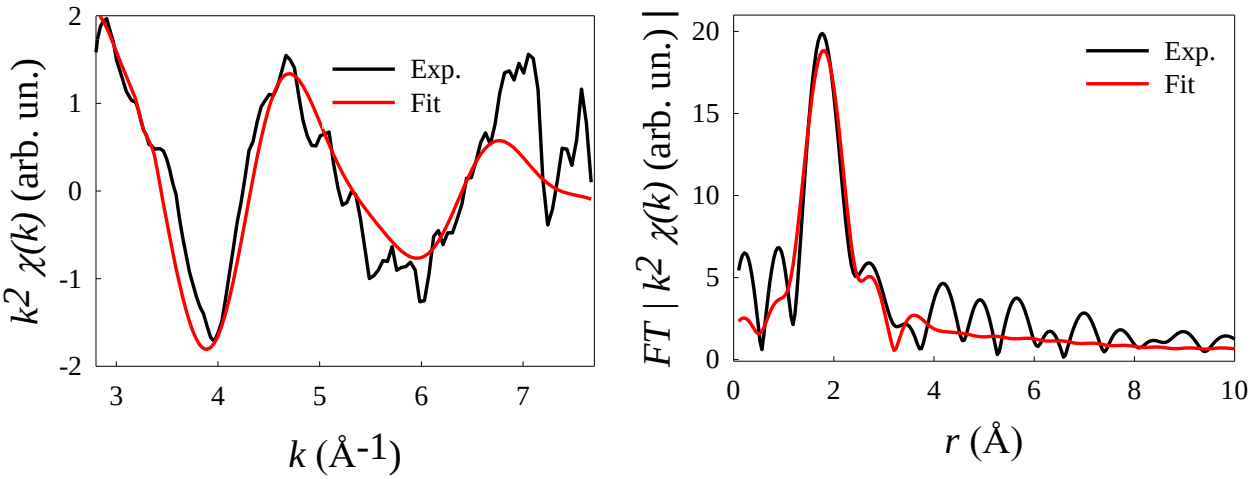

Figure 8.4. Cu-K edge EXAFS signal (A) and the corresponding FT (B) of the alkaline solution of Copper(II) lactate. The experimental signal is represented by the black line, whereas the fit according to the model described in the text is represented by the red line.

The experimental signal is represented by the black line while the fit is the red line. EXAFS oscillations are well visible up to k=8 Å^{-1} and thus it is possible to obtain reasonable quantitative parameters referred to distances within ca. 4 Å from the photoabsorber. The model employed for the EXAFS fitting is a cluster composed of two coordination shells of oxygen atoms: the first is made up of four oxygen atoms situated at ca. 1.9 Å, and the second is composed by four oxygen atoms at ca. 3 Å. This large distance suggests that the two oxygen atoms are not directly bonded to the central Cu(II). Coordination numbers are intrinsically non well defined in EXAFS analysis but the presence of other oxygen atoms in the second shell is a proof that the first shell of oxygen atoms is not able alone to justify the local chemical environment of the photo-absorber.

Tab. 8.2. shows the best parameters obtained in the fitting procedure. The GOF value obtained (23.1 %) can be considered good, having in mind that the dispersive-XAS spectrum is time resolved and thus the signal-to-noise ratio is not as good as in the standard XAS acquisition procedure.

Shell	***N***	**Atom**	***r* (Å)**	**σ^2 (Å^2)**
1	4	**O**	1.87(2)	10(2) x 10^{-3}
2	4	**O**	3.35(6)	8(9) x 10^{-3}
Goodness of Fit *F*= 23.1 %				

Table 8.2. EXAFS fitting parameters for spectra in Figure 8.4. *r*: Distances, σ^2: Distance variances. Coordination numbers *N* have been kept constant.

These results are the basis of the construction of the model employed in the subsequent analysis, represented by the XANES simulation of the aqueous complex. The presence of four oxygen atoms in the first shell of the cluster used in the EXAFS fit (Tab. 8.2) accounts for a tetrahedral or square planar arrangement of lactate anions around the Cu(II) central atom. We can therefore assume three different local arrangements for the coordination geometry of copper(II) lactate: *(i)* Model A (Fig. 8.5.A) consisting of two lactate ions acting as bidentate ligands and characterized by a tetrahedral geometry; *(ii)* Model B (Fig. 8.5.B) comprising two lactate ions acting as bidentate ligands in a square planar arrangement in which two additional water molecules are present in the apical positions yielding an overall distorted octahedral geometry, and *(iii)* Model C (Fig. 8.5.C), which is composed of four lactate ions acting as monodentate ligands to yield a coordination number of 4 in a geometrical arrangement characterized by point symmetry S_4.

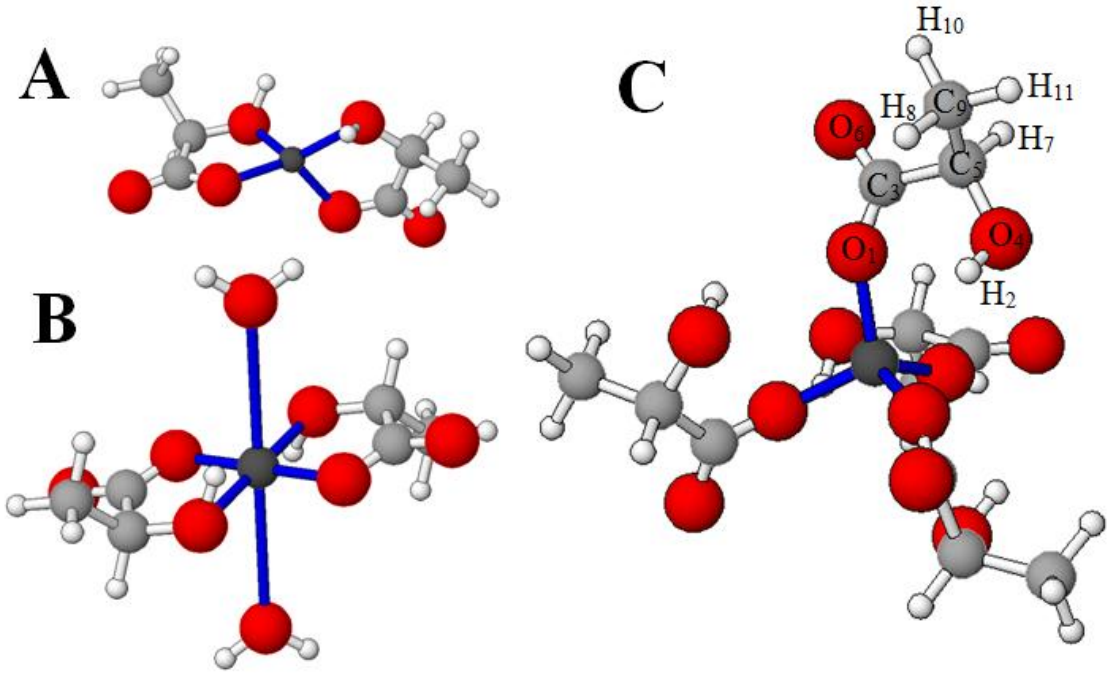

Figure 8.5. Scheme of the three models (A, B and C) employed for the XANES calculations.

Fig. 8.6 shows the test of these three models against the experimental data. The blue spots are the experimental signal whereas the coloured full lines represent the Cu-K edge XANES calculations. At the bottom, the simulation for the simplest geometry (a tetrahedral arrangement with two lactate ions acting as bidentate ligands) is illustrated: the theoretical spectrum, represented by an orange line, leads to poor results, according to previous assumptions made by EXAFS analysis. The first coordination shell of four oxygen atoms is not able alone to justify the local chemical environment of Cu^{2+} ion; and another shell composed of two oxygen atoms situated at ca. 3.3 Å is needed. This consideration led us to employ a model in which two ligands act as bidentate ions in a square planar arrangement and two additional oxygen atoms are present in the apical positions to yield an overall distorted octahedral geometry (Model B). The XANES calculation performed by means of this model is shown in the middle of Fig. 8.6 as a green line: this simulation is better if compared to

that obtained with model A but still it can be improved. The major discrepancies between the theoretical and the experimental spectrum are evidenced by the black arrows. Furthermore, these discrepancies can be better observed in the derivative spectra reported in the insight of the figure on the right.

Thus, we remove the constraint imposing the lactate anions acting as bidentate ligands. Taking into account that even though lactate anion is 15 times more concentrated than copper sulphate, steric hindrance limits the maximum number of ligands around Cu in a single complex and assuming the presence of four lactate anions acting as monodentate ligands (model C), we obtain that the agreement between the experimental signal and theoretical simulation (red line) is largely improved and all the relevant spectral features of XANES manifold are correctly simulated. Therefore, the structure of copper(II) lactate in alkaline solution is different from that assumed by copper(II) lactate in solid state[9].

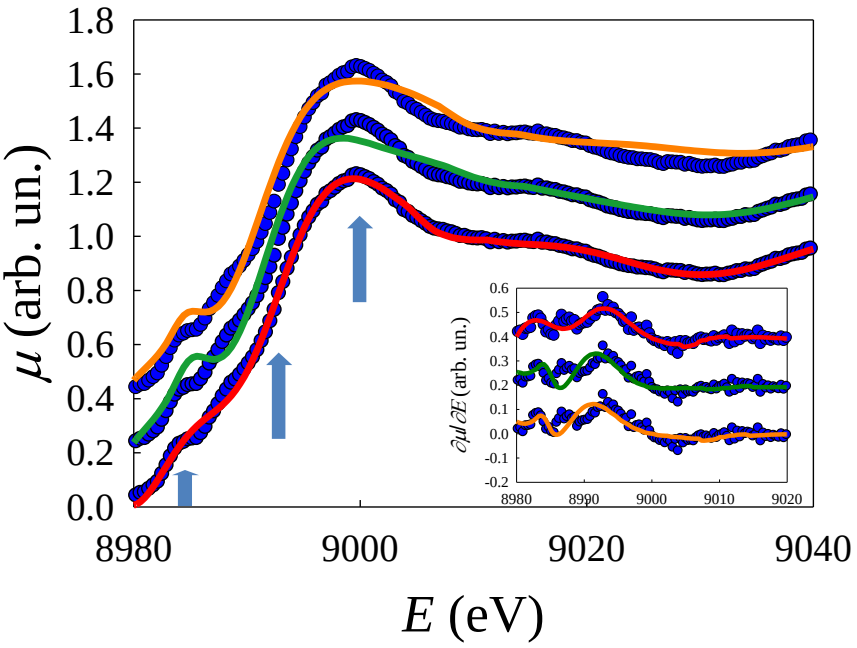

Figure 8.6. Cu-K edge XANES simulations of copper(II) lactate starting solution. The blue spots represent the experimental signal while the coloured lines are the theoretical calculations according to the Model A (orange line), to Model B (green line) and to Model C (red line). An insight illustrating the derivative of both the experimental and the calculated spectra is included.

In Tab. 8.3 the best results of the XANES simulation referred to Model C are shown.

Atom Number	Type of atom	Distance from Cu(II) (Å)	σ^2 (Å^2)
1	**O**	1.855(4)*	6(2) x 10^{-3}*
2	**H**	2.977	6(2) x 10^{-3}*
3	**C**	3.000	6(2) x 10^{-3}*
4	**O**	3.234	6(2) x 10^{-3}*
5	**C**	3.720	6(2) x 10^{-3}*
6	**O**	3.919	6(2) x 10^{-3}*
7	**H**	4.351	6(2) x 10^{-3}*
8	**H**	4.704	6(2) x 10^{-3}*
9	**C**	4.871	6(2) x 10^{-3}*
10	**H**	5.492	6(2) x 10^{-3}*
11	**H**	5.583	6(2) x 10^{-3}*
Goodness of Fit *F*: 0.013 %			
* Fitted values			

Table 8.3. XANES calculation parameters associated to Model C and referred to the theoretical signal represented by a full red line in Fig. 8.6. the fitted parameters are marked by *.

Each line refers to an atom of the cluster employed to calculate the theoretical signal: for each atom the distance from the photo-absorber and the corresponding Debye-Waller factor are indicated. In the fitting procedure, only the distances of the nearest oxygen atoms and the corresponding Debye-Waller factors were fitted and maintained equal to each other. The *GOF* parameter, which is 0.013 %, is a clear indication that the fit according to Model C is very good. In addition, we observe that the parameters obtained by XANES analysis are in perfect agreement to those obtained by EXAFS analysis (Tab. 8.2). All the nearest distances between carbon and oxygen atoms, in each lactate, obtained by the theoretical calculation (according to Model C) were checked by a comparison with literature. As we can see from Tab. 8.4 there is no significant difference between the two.

LACTATE INTERATOMIC DISTANCES		
Atoms	**Distance in the model (Å)**	**Distance in literature (Å)**
O_1—C_3	1.241	1.219
C_3—C_5	1.507	1.507
C_3—O_6	1.219	1.219
O_4—C_5	1.429	1.429
C_6—C_7	1.507	1.507
C_5—C_9	1.530	1.530

Table 8.4. Nearest distances between carbon and oxygen atoms in each lactate molecule present in Model C (Fig. 8.5.C): a comparison between theoretical values and literature.

In order to validate this rationally we discuss the electronic transitions towards localized empty states by observing the XANES spectrum of copper(II) lactate complex in the alkaline solution and the corresponding derivative (Fig. 8.7).

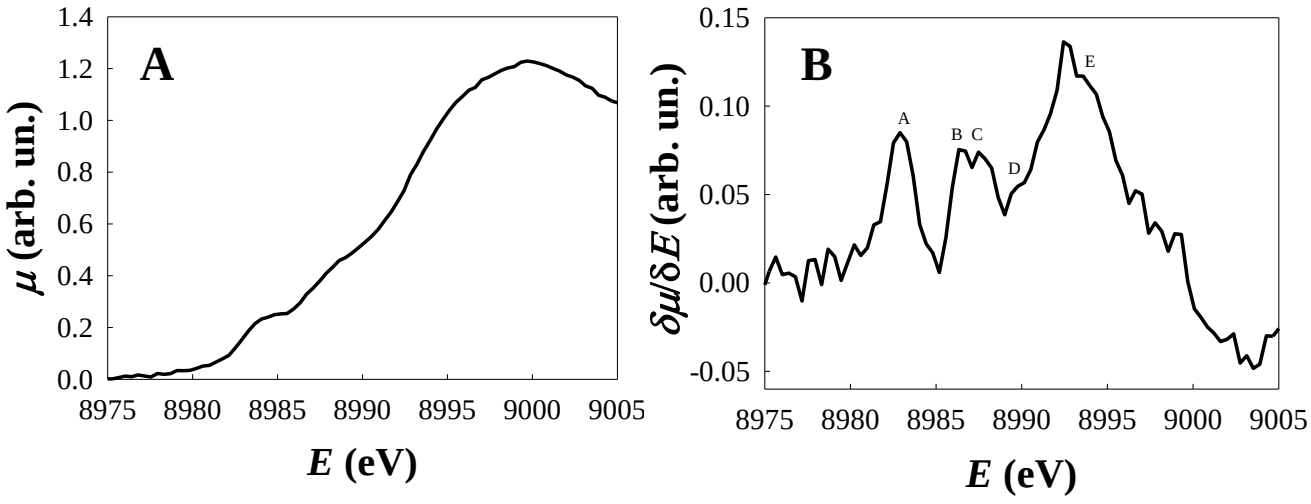

Figure 8.7. Cu-K edge XANES spectrum (A) and the corresponding derivative signal (B) of the copper(II) lactate starting solution. The energy range shown is limited to 30 eV around the threshold in order to better visualize the features corresponding to the electronic transitions towards localized empty states.

As we can observe from the normalized XANES spectrum (A), Cu(II) gives rise to an intense White Line at 8999 eV corresponding to the electronic transition from *1s* states to continuum[33] and other weak peaks before 8990 eV, in the pre-edge region, ascribed to the *1s* → *3d* and *1s* → *4p* electronic transitions. These spectral features can be better evidenced in the corresponding derivative spectrum (B). The peak A, situated at ca. 8983 eV is attributable to the *1s* → *3d* electronic transition while the three features present in the energy range from 8985 and 8990 eV (B, C and D) are due to the *1s* → *4p* electronic transitions. The presence of three different signals for the $4p_x$, $4p_y$ and $4p_z$ final states is a clear proof for the non-equivalence of the three space directions and thus for a distorted local chemical surrounding. On the basis of the small distance between the peaks (ca. 1 eV between B and C, and ca. 2 eV between C and D), a distorted tetrahedral environment is expected. In order to ensure neutral charge, Cu : Lactate stoichiometric ratio should be 1 : 2. However, since the solution present a large excess of lactate compared to the copper sulphate (lactate is 15 times more concentrated) it is reasonable to assume that the complex contains more than one lactate anion and therefore that it is characterized by a negative charge.

While performing XANES simulation an important point concerns the inclusion of hydrogen atoms in the cluster. It is important to underline the small scattering factor makes hydrogen atoms intrinsically not well defined in XAS spectroscopy. During the processing of the data obtained in this experiment we investigated the contribution of the hydrogen atoms to the theoretical calculation. As far as the calculation based on Model C is concerned, in Fig. 8.8 a comparison between the simulation in presence (red lines) and in absence (green lines) of hydrogen atoms in the cluster is illustrated.

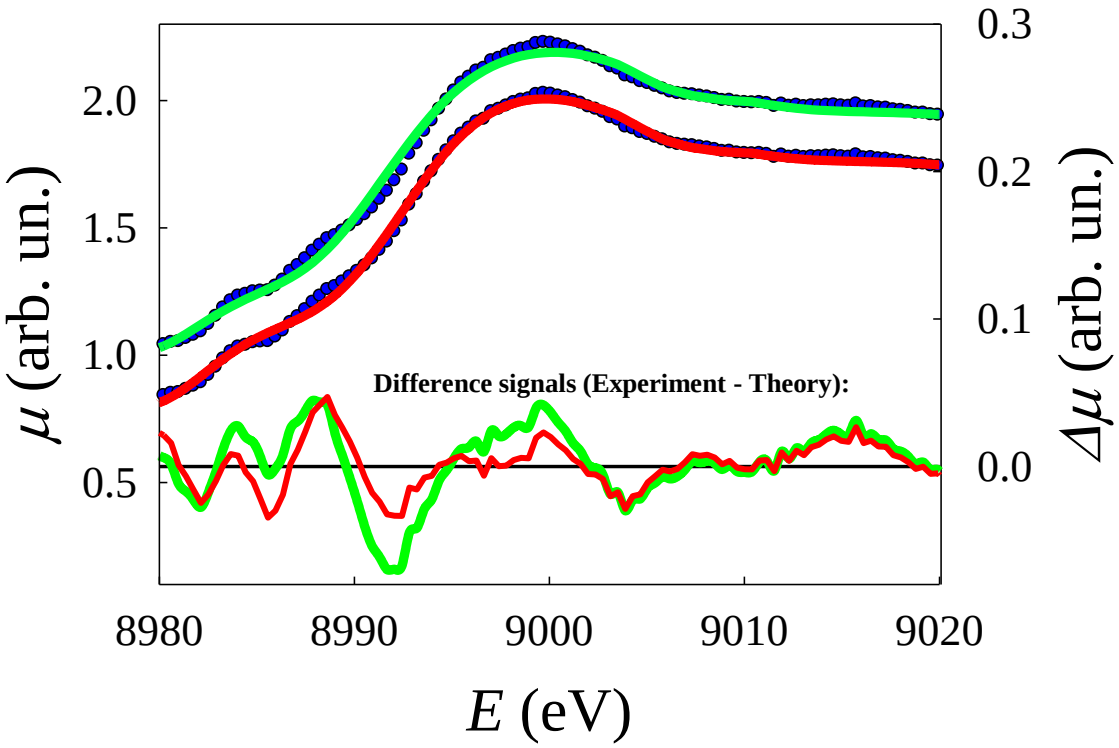

Figure 8.8. Comparison of the simulations of Copper(II) lactate XANES according to Model C with (red line) and without (green line) the inclusion of the hydrogen atoms in the cluster. The experimental signal is represented by the blue spots and the experimental - calculated differences are illustrated at the bottom of the figure for the two cases.

It is evident that the inclusion of hydrogen atoms remarkably affects the theoretical signal determining substantial variations in the simulated XANES spectrum (evidenced by the black arrows). Observing the difference signal between the calculated and the experimental spectra we note that the simulation performed with the inclusion of hydrogen atoms leads to a best fit result. This is a clear indication that the inclusion of hydrogen atoms cannot be neglected, at least up to 20/30 eV above the absorption edge.

8.4. COPPER(II) LACTATE STABILITY

The stability of copper(II) lactate complex was investigated in a potential range in which the complex is expected to be electrochemically stable. A series of 320 spectra with an integration time of 500 ms for a total time equal to 160 s was recorded. Measurements were performed *in operando* while applying a Linear Sweep Voltammetry (LSV) from 1.2 to -0.4 V (*vs* Ag/AgCl) triggered by a potentiostat (CH instrument 630D) which was controlled by the spectra acquisition system. The data processing step was based on: *(i)* preliminary processing and signal extraction, and *(ii)* automatic XANES fitting by linear combination of spectra of standard compounds. The process was carried out by means of LinComb tool belonging to PRESTOPRONTO[20] software.

Fig. 8.9.A shows the XANES spectra of Metallic Cu standard, Cu_2O standard and copper(II) lactate in the starting solution. Differences in the spectra of the three materials are not simply related to a shift of the absorption edge but also to a substantial variation in the spectral profile. As for example, Fig. 8.9.B illustrates seven spectra selected from the sequence and separated by time intervals of ca. 25 s.

The increase in the pre-peak, marked by the black arrow, is a clear indication that Cu(II) undergoes a little reduction process to Cu(I).

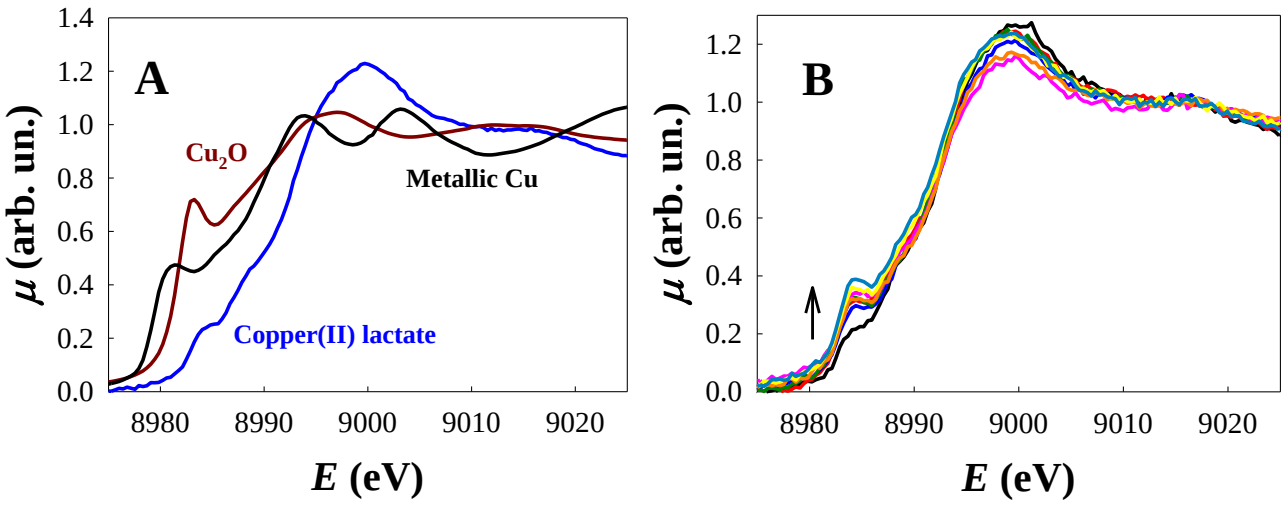

Figure 8.9. A): Cu-K edge XANES spectra of the standards of Copper(II) lactate (blue line), Cu_2O (brown line) and metallic Cu (black line). B) seven spectra selected from the sequence recorded on the Copper(II) lactate solution during the application of the LSV and separated by a time interval of ca. 25 s

The variations along the sequence of spectra were evaluated by a XANES linear combination of two normalized reference spectra (obtained from Cu_2O standard and from Cu(II) lactate starting solution). The experimental spectra μ_{exp} were fitted by means of a theoretical curve calculated as a linear combination of the two reference XANES spectra:

$$\mu_{\text{exp}} = \sum_j \alpha_i \boldsymbol{\mu_{th}} \qquad (8,10)$$

Thanks to the investigation of the dependence of α_i upon the potential, it was possible to evaluate the percentage of copper(II) lactate during the application of the electrochemical program.

The energy range in which the fitting procedure was performed is 8950 – 9030 eV. Fig. 8.10 illustrates the results obtained: the coefficients α_i, associated to the amount of the two species, are related to the potential applied.

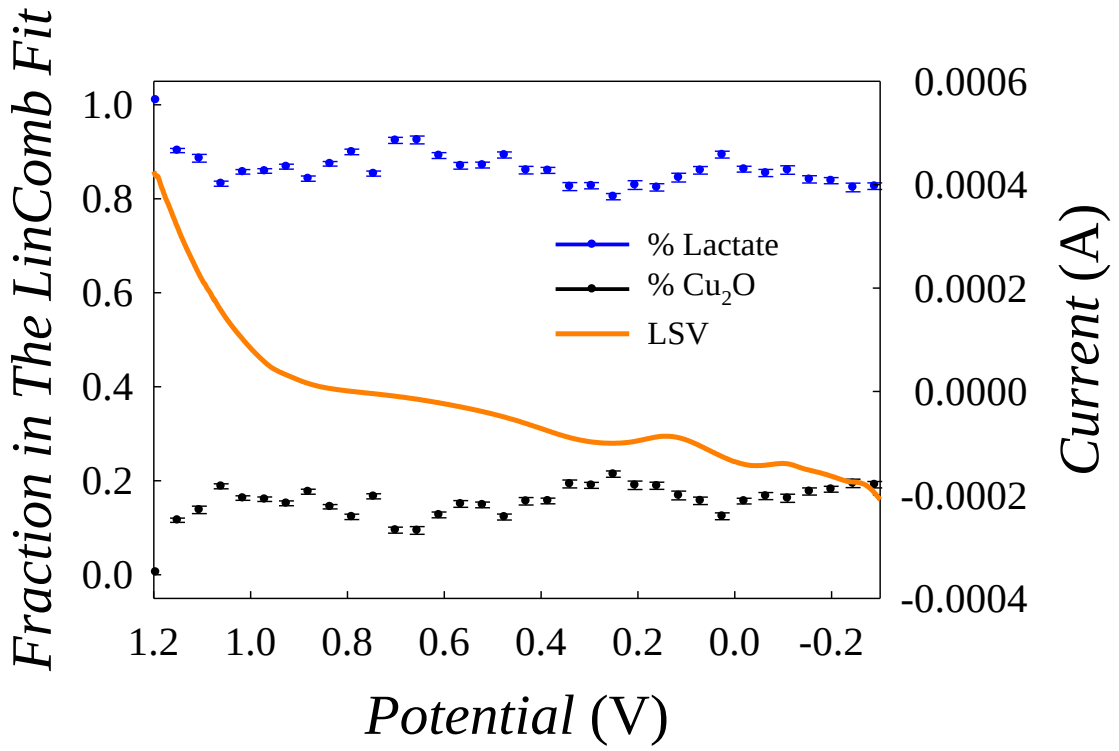

Figure 8.10. Results of the automatic linear combination fitting of the XANES spectra of the sequence recorded during the application of the LSV. The blue spots represent the percentage of Copper(II) lactate, the black spots represent the percentage of Cu_2O and the orange line is the LSV. In order to reduce the scattering of the results, only a spectrum every ten was selected.

At time zero, before the application of the electrochemical program, the amount of Cu(II) lactate is equal to 100 % and no Cu(I) is present. A little amount of Cu_2O (10 %) begins to appear at potential ca. 1.1 V, increasing up to ca. 20 % at ca. 1 V. Then it remains almost constant during the rest of the linear sweep. The initial formation of Cu(I) oxide is not ascribed to radiolysis phenomena generated by the X-ray beam since preliminary tests demonstrated that in absence of the electric circuit the spectral shape remains the same along the whole sequence. At the end of the CV (when the potential is -0.4 V) the amount of Cu_2O is ca. 25 %. In order to check the percentage values obtained by the automatic fitting procedure, four XANES spectra at different potential values along the LSV were selected and fitted manually by means of ATHENA software. Fig. 8.11 illustrates the results obtained in the four cases. At the beginning of the

LSV (for potential equal to 1.2 V) the spectrum corresponds to that of copper(II) lactate in the alkaline solution (A). A small amount of Cu(I) is detected at potential 0.95 V (B) and the quantity is increased at 0.29 V (C). At the end of the electrochemical program (at potential -0.39 V) the percentage of Cu_2O formed is slightly above 20 %.

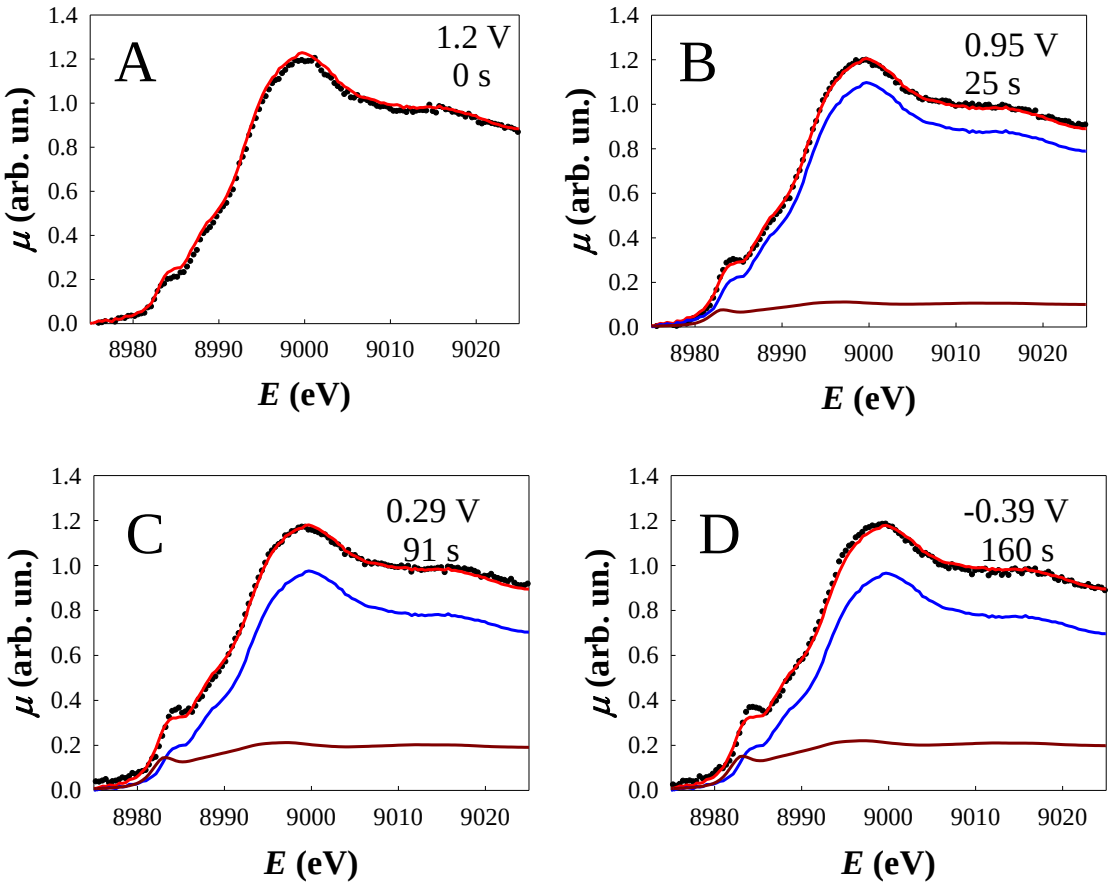

Figure 8.11. Manual linear combination fit of four XANES spectra selected among the whole sequence acquired during the LSV program at 1.2 V (A), 0.95 V (B), 0.29 V (C) and -0.39 V (D). The Black spots represent the experimental signal while the red line the theory, the blue line is Copper(II) lactate contribution and the brown line represents Cu_2O contribution.

The numerical values obtained by the manual fitting procedure are illustrated in Tab. 8.5. The fractions of the standards at the four different time/potentials are in good agreement with the outcome of the automatic linear combination procedure.

Time (s)	*Potential* (V)	*Copper(II) Lactate Fraction(%)*	*Cu_2O Fraction(%)*
0	1.2	100	0
25	0.95	89.3(8)	10.7(7)
91	0.291	79.7(7)	20.3(7)
160	-0.39	78.9(8)	21.1(8)

Table 8.5. Fractional parameters obtained by the manual linear combination fitting of the four XANES spectra reported in Fig. 8.11.

8.5. CONCLUSIONS

The experiment described in this section allowed us to investigate the geometric structure and the electronic properties of one of the most used precursors for the preparation of Cu_2O: copper(II) lactate complex in alkaline solution.

EXAFS fitting and *ab initio*-XANES calculations were performed in order to gain information about the local structure of Cu(II) in the aqueous complex. The best fits obtained account for a model in which four lactate ions act as monodentate ligands to yield a coordination number of 4 in an geometrical arrangement characterized by point symmetry S_4. This is different from the structural determinations referred to solid state[9] but is reasonable considering the large excess of lactate (15 times more concentrated than Cu(II)).

For what concerns the electrochemical stability of copper(II) lactate solution, the sequence of spectra recorded while applying a Linear Sweep Voltammetry from 1.2 to -0.4 V (*vs* Ag/AgCl) showed that a little reduction from Cu(II) to Cu(I) takes place below 0.4 V but at the end the percentage of copper(II) lactate is still ca. 80 %.

REFERENCES

[1] T. D. Golden, M. G. Shumsky, Y. Zhou, R. A. VanderWerf, R. A. Van Leeuwen, and J. A. Switzer, *Chem. Mater.* (1996), 8, 2499-2504;

[2] J. Katayama, K. Ito, M. Masuoka, and J. Tamaki *J. Appl. Electrochem.* (2004), 34, 687–692;

[3]J. Xue, and R. Dieckmann, *J. Phys. Chem. Solids* (1990), 51, 1263--1275;

[4]M. Ristov, G. J. Sinadinovski, and M. Mitreski, *Thin Solid Films* (1998), 167, 309;

[5]V. Ashworth, and D. Fairhurst, *J. Electrochem. Soc.* (1977), 124, 506;

[6]C. Ortiz, C. N. Afonso, F. Vega, J. Solis, J. C. Cheang, C. Ortega, and J. Siejka, *Appl. Surf. Sci.* (1992), 54, 201;

[7]A. K. Mukhopadhyay, A. K. Chakraborty, A. P. Chatterjee, and S. K. Lahiri, *Thin Solid Films* (1992), 209, 92;

[8] A. Paracchino, J. C. Brauer, J.-E. Moser, E. Thimsen, and M. Graetzel, *J. Phys. Chem. C* (2012), 116, 7341—7350;

[9] C. K. Prout, R. A. Armstrong, J. R. Carruthers, J. G. Forrest, P. Murray-Rust, and F. J. C. Rossotti, *J. Chem. Soc.* (1968), 2791—2813;

[10] J.J. Rehr , W. Schattke , F.J. Garcıa de Abajo , R. Dıez Muino , and M.A. Van, *J.Electron Spectrosc.* (2002), 126, 67–76;

[11] A. L. Ankudinov, B. Ravel, J. J. Rehr, and S. D. Conradson, *Phys. Rev. B* (1998), 58, 7565—7576;

[12] S. Mobilio, and F. Boscherini SYNCHROTRON RADIATION Basics, Methods and Applications (2015);

[13] T. Fujikawa, *J. Phis. Soc. Jpn.* (1993), 62, 2155—2165;

[14] N. Binsted, and S.S. Hasnain *J. Synch. Rad.* (1996), 3, 185;

[15] S. Pascarelli, O. Mathon, M. Munoz, T. Mairs and J. Susini *J. Synchrotron Radiat.* (2006), 13, 351;

[16] S. Pascarelli and O. Mathon *Phys. Chem. Chem.* Phys. (2010), 12, 5535;

[17] J. C. Labiche, O. Mathon, S. Pascarelli, M. A. Newton, G. G. Ferre, C. Curfs, G. Vaughan, A. Homs and D. F. Carreiras *Rev. Sci. Instrum.* (2007), 78, 091301 27;

[18] E. Achilli, A. Minguzzi, A. Visibile, C. Locatelli, A. Vertova, A. Naldoni, S. Rondinini, F. Auricchio, S. Marconi, M. Fracchia, and P. Ghigna, *J. Synchrotron Rad.* (2016), 23;

[19] http://pymca.sourceforge.net/;

[20] S. J. A. Figueroa, and C. Prestipino, J. Phys.:Conf. Ser. (2016), 712, 012012;

[21] J. Garcia, M. Benfatto, C.R. Natoli, A. Bianconi, A. Fontaine, and H. Tolentino, *Chem. Phys.* (1989), 132, 295—302;

[22] P. Frank, M. Benfatto, M. Qayyam, B. Hedman, and K. O. Hodgson, *J. Chem. Phys.* (2015), 142, 084310;

[23] M. Benfatto, J. A. Solera, J. Chaboy, M. G. Proietti, and J. Garcìa, *Phys. Rev.* (1996), 56, 2447—2452;

[24] A. I. Frenkel, G. V. Korshin, and A. L. Ankudonov, *Environ. Sci. Technol.* (2000), 34, 2138—2142;

[25] J. Brugger, B. Etschmann, W. Liu, D. Testemale, J.L. Hazemann, H. Emerich, W. van Beek, and O. Proux, *Geochim. Cosmochim. Ac.* (2007),71, 4920–4941;

[26] G. La Penna, V. Minicozzi, S. Morante, G. C. Rossi, and F. Stellato, *J. Chem. Phys.* (2015), 143, 124508;

[27] J. Chaboy, A. Muñoz-Páez, P. J. Merkling, and E. S. Marcosa, *J. Chem. Phys.* (2006), 124, 064509;

[28] A. Manceau, and A. Matynia *Geochim. Cosmochim. Ac* (2010), 74, 2556—2580;

[29] J. Blumberger, *J. Am. Chem. Soc.* (2008), 130, 16065--16068;

[30] X. Liu, X. Lu, E. J. Meijer, and R. Wang *Phys. Chem. Chem. Phys.* (2010), 12, 10801--10804;

[31] X. Liu, J. Cheng, and M. Sprik, *J. Phys. Chem. B* (2014), 119, 1152--1163;

[32] P. Frank, M. Benfatto, M. Qayyam, B. Hedman, and K. Hodgson, *J. Chem. Phys.* (2015), 142, 084310;

[33] A. Manceau, and A. Matynia, *Geochim. Cosmochim. Ac* (2010), 74, 2556—2580.

9. Ag ELECTROCATALYST AND THE DEHALOGENATION OF ORGANIC POLLUTANTS

Organic halides are gaining more and more attention both in fundamental science and in the applied and industrial chemistry. In particular, they have known a worldwide spread as building blocks[1-5] for the synthesis of value added organic compounds and for the industrial production of polymers, pesticides, herbicides and fungicides. The importance of these compounds ranges from agriculture, to the production of mechanical and thermal fluids, and the realization of solvents for industry and housework.

Chlorinated and brominated organic compounds are characterized by varying degrees of toxicity and can cause harmful effects on living organisms[6]. The major problem is associated to their carcinogenic and mutagenic properties[7]. Among the organic halides, benzyl chloride ($PhCH_2Cl$) is being carefully investigated as a model compound since the C-Cl bond present is significantly coupled to the aromatic system[8].

Recent studies have pointed out that the reduction of organic halides can be easily promoted by specific metallic cathodes such as Ag, Pd and Cu[9-12]. In particular Ag is considered the most powerful electrocatalyst for the dehalogenation of organic halides[13-16] and appears to be applicable to a large variety of organic halogenated compounds[11]. Nevertheless, the reasons lying behind this exceptional activity are still not well understood. The purpose of the experiments presented in this chapter is to perform *in situ* and in *operando* measurements combining spectroscopy and electrochemistry in order to shed light on the mechanism governing the electro-cleavage of the C-X bond in

organic pollutants. The most threatening class of organic halides is represented by the chlorinated compounds. In this case only the Ag-K edge is accessible in the hard X-ray region, required to perform *in situ* and *in operando* measurements. It is important to underline that the main downside of this edge is associated to the short extension of the oxidation range presented by Ag. Furthermore, the final states of this transition are of *p* character and thus any charge state variation due to the electrochemistry of Ag (and associated to *d* orbitals) is very difficult to observe in the XANES spectrum. An alternative approach consists in employing a brominated organic compound as model for the organic halide and exploring the Br-K edge.

9.1. THE EXPERIMENTS ON L.I.S.A. BEAMLINE

Two experiments have been carried out on LISA beamline[17] (BM08, ESRF) in order to investigate the exceptional electrocatalytic activity of Ag: *(i)* the first was performed at the Ag-K edge taking tri-chloromethane as a model and *(ii)* the second was performed at the Br-K edge with the aim of studying the adsorption of 2-bromophenol.

A Si(311) double crystal was employed as monochromator, the harmonic rejection was realized by means of Pd mirrors (characterized by a cutoff energy of 20 keV) and the detector was a 13-element Ge.

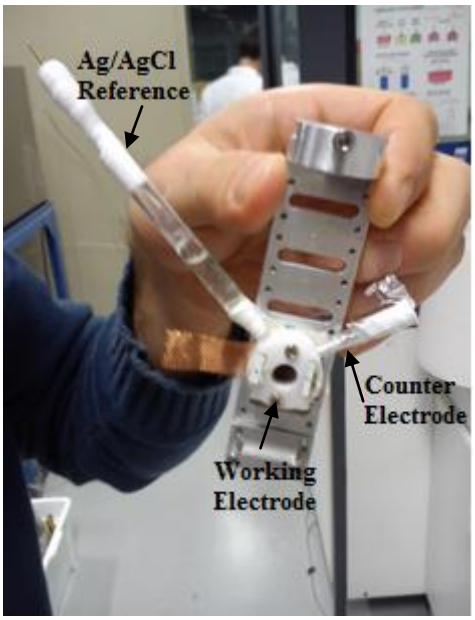

Figure 9.1. Spectro-electrochemical device employed to investigate the electrocatalytic activity of Ag, mounted with the three-electrode configuration.

The spectro-electrochemical device employed is a PTFE cell composed of a plate and a frame cylinder which allows a three-electrode configuration. The sample is irradiated by means of the X-rays through a hole present in the frame. Fig. 9.1 shows an image of the cell assembled with the working electrode, the counter (Au wire) and the Ag/AgCl reference.

The working electrode is made of Ag nanoparticles deposited onto glassy carbon (Goodfellow, 1 mm thick and 1 cm^2 area) in order to obtain 0.1/0.2 mg/cm^2 of Ag (see Section 3.4.1). The counter and the reference electrodes are inserted in the device through two radial holes designed in the main body of the cell.

9.2. Ag-K EDGE AND THE ADSORPTION OF $CHCl_3$

The preliminary X-Ray Absorption analysis we applied to the Ag electrodes was the FEXRAV[18]. The intention was to identify the potential range in which the most important charge state variations of Ag occur. It is important to remember that the μ contrast in the case of a K edge can be quite small if compared to a L edge. As a consequence the choice of the energy value to be fixed is not straightforward and requires a careful evaluation on the basis of XANES standard spectra. In Fig. 9.2 the spectra of three standards are illustrated.

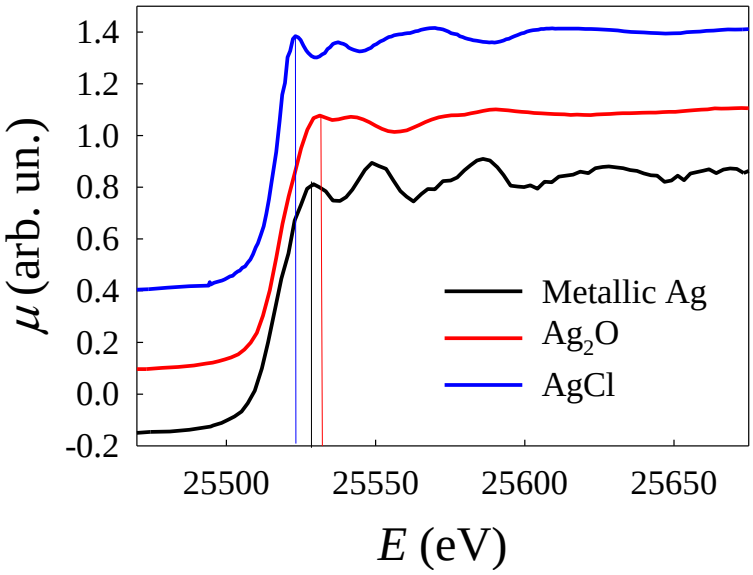

Figure 9.2. XAS spectra of Ag (black), Ag_2O (red), AgCl (blue) standard samples.

The three coloured vertical lines mark the energy of the peaks closest to the absorption edge. In order to obtain the best contrast between metallic Ag and AgCl halide, the energy 25520 eV was chosen: at this value $\mu_{AgCl} > \mu_{Ag} > \mu_{Ag_2O}$. The energy should be selected in the XANES region where the chemical shift is observed. Since this is the first time that FEXRAV is applied to silver nanoparticles and that a heterogeneous charge transfer is studied at a silver electrode, we first investigated the behaviour of the working electrode in presence of 0.1 M KCl in aqueous 0.1 M $KClO_4$ (Fig. 9.3). The CV (indicated by a black line) was carried out at 1 mV/s by means of a CHI potentiostat/galvanostat (model 630D). The starting potential was -1.2 V and the potential range investigated was -1.2 V – +0.5 V. The main Ag oxidation and reduction peaks are situated at about +0.150 V and -0.012 V respectively. The other two anodic/cathodic peaks, observed at -0.08 V and -0.28 V are generated by the adsorption and desorption of chloride ions. The FEXRAV signal (represented by the dashed red line) shows variations in agreement with the electrochemical signal. An increase in the potential determines an increase in

the absorption coefficient when the appropriate value for the oxidation of Ag is reached. In detail, starting from -1.2 V, the absorption coefficient remains stable to its lowest value until +0.13 V when it starts increasing. The maximum value is reached when the potential becomes equal to +0.24 V, thus indicating that the oxidation of Ag from 0 to +1 is complete. When the potential scan is reversed μ remains stable to its largest value until +0.05 V, then it starts decreasing as Ag metallic is formed. During the negative potential scan, FEXRAV signal is marked by two steps levelling at an intermediate potential value between -0.05 V and -0.20 V. At potential equal to -0.3 V, when chlorides desorption is complete, μ reaches its lowest value which remains stable for lower potentials. Furthermore, if a second cycle is performed, the value of the absorption coefficient for E > +0.2 V is lower than the previous one. This accounts for a smaller number of Ag atoms due to a loss of material and is a demonstration that the process is not completely reversible. However, the loss can be considered low if we observe that the absorption coefficient for E < -0.3 V is equal in the two cycles.

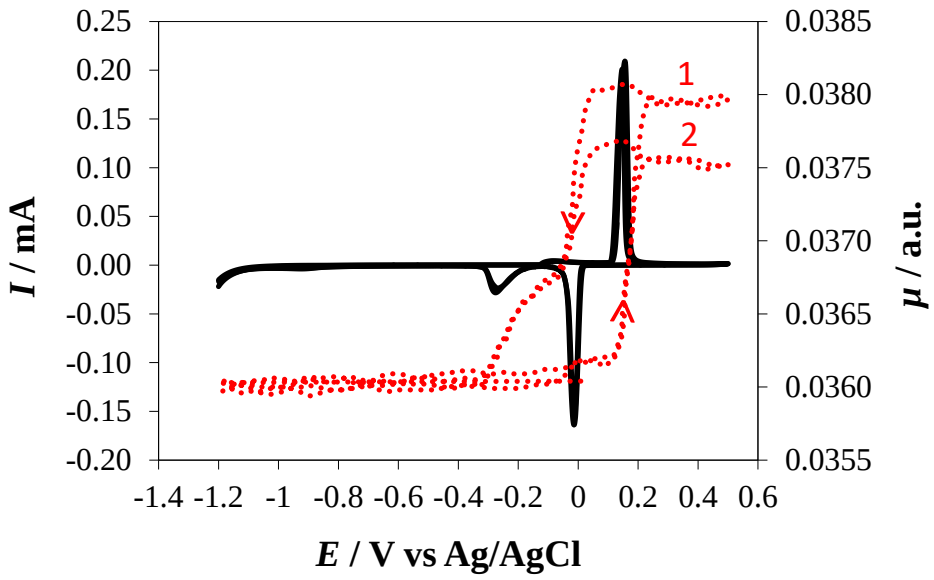

Figure 9.3. CV (full black line) and FEXRAV (dashed red line) signals for Ag electrodes in the presence of 0.1 M KCl in aqueous 0.1 M $KClO_4$, at 1 mV/s, in the −1.2/+0.5 V (vs Ag/AgCl) potential window. The FEXRAV signal has been smoothed.

These results show that FEXRAV technique is very sensitive in detecting small variations in the absorption coefficient and provides a valuable tool for a preliminary investigation. However, in order to perform a deeper and more detailed study, is necessary to record full XAS spectra, carrying further information about the local chemical and geometric environment. As far as the electrochemical oxidation/reduction of Ag is concerned, the *in situ* investigation was carried out in specific electrochemical conditions in order to study the changes in the electronic structure of silver during the occurrence of the electrochemical reactions. Full XAS spectra were obtained at three different potentials: *(i)* -1.2 V, in fully reductive conditions, *(ii)* -0.1 V, in intermediate conditions, and *(iii)* +0.5 V , in fully oxidative conditions. The potential at which Cl^- is expected to be adsorbed and thus to have contribution is -0.1 V. Fig. 9.3 shows the normalized Ag-K edge XAS spectra for the three different applied potentials, for the Open Circuit Potential (OCP) and for the Ag and AgCl standards.

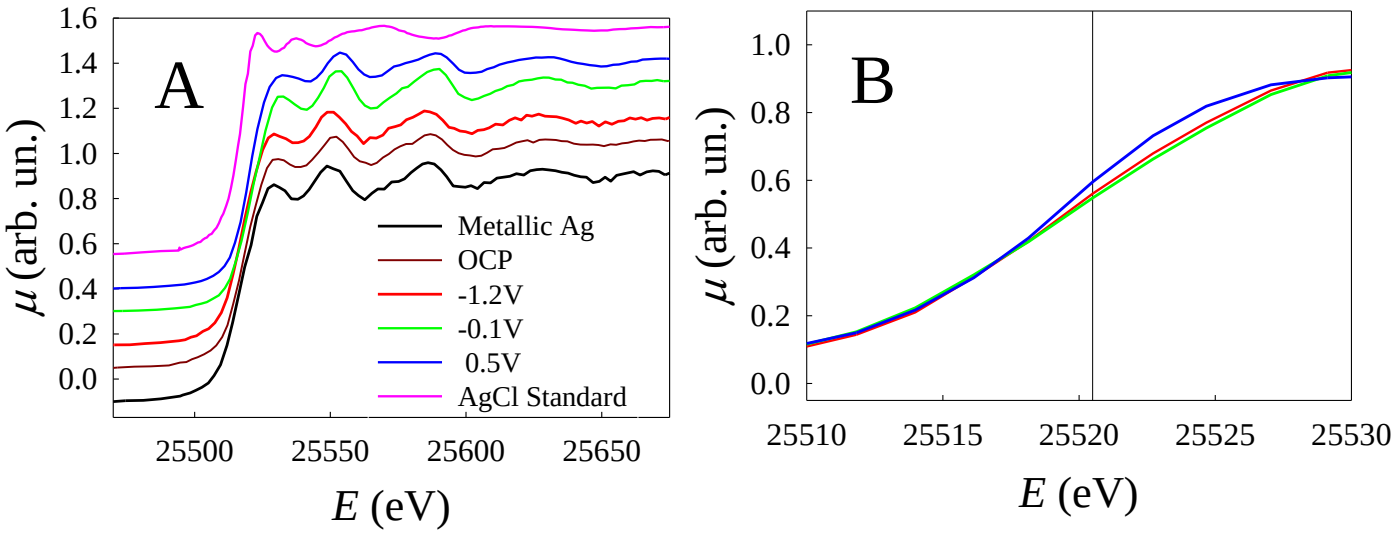

Figure 9.4. A): Normalized Ag-K edge XAS spectra recorded at Open Circuit Potential (brown), at potential -1.2 V (red), -0.1 V (green) and +0.5 V (blue). The spectra of metallic Ag and AgCl standard materials are added and represented by a black line and a pink line respectively. For better clarity the spectra are shifted along the *y* axis. B) XANES spectra recorded at the three different potentials in a smaller energy range. The black vertical line marks the energy value (25520.4 eV) at which FEXRAV investigation was carried out.

Looking at Fig. 9.4.A, as we can expect, at applied potential -1.2 V the spectral profile (red line) is very similar to that of Ag standard: this confirms that Ag is present in the metallic form. In oxidative condition (E=+0.5 V) the XAS spectrum accounts for a partial oxidation of Ag (blue line) while the largest fraction is present in the metallic form. This result is in agreement with electrochemistry pointing to a residual reduced Ag amount of 89/90 %. This behaviour can be explained by the formation of clusters in which the oxidation of Ag takes place only on the outer layer. An enlargement of the spectra acquired at the three different potentials is illustrated in Fig. 9.4.B: the XANES spectra are shown in a smaller energy range and the black vertical line, in correspondence of 25520.5 eV, marks the energy value employed during the preliminary FEXRAV analysis.

The subsequent EXAFS analysis was carried out in order to validate this assumptions for potential -1.2 V (Fig. 9.5.A), -0.1 V (Fig. 9.5.B) and +0.5 V (Fig. 9.5.C). EXAFS signal was extracted by means of ATHENA software[19] and processed by means of EXCURVE code[20]. The oscillations, visible above the noise level up to 9 $Å^{-1}$, allowed us to investigate only the first shell in the local structure of the photoabsorber. EXAFS signals obtained at potentials -1.2 V and -0.1 V were fitted by means of a model made up of one cluster of metallic Ag composed of 12 Ag atoms arranged in a cubic compact environment. The spectrum recorded at +0.5 V was treated with a model constituted of two clusters: the first made of 6 Cl atoms in an octahedral arrangement (typical of AgCl) and the other composed of 12 Ag atoms (typical of metallic Ag). The multiplicities employed are 30% and 70 % respectively, in good agreement with electrochemistry measurements.

Fitting results are illustrated in Tab. 9.1 for the three different applied potentials. In all cases the *GOF* parameter is well below 20 % thus indicating a good fitting procedure.

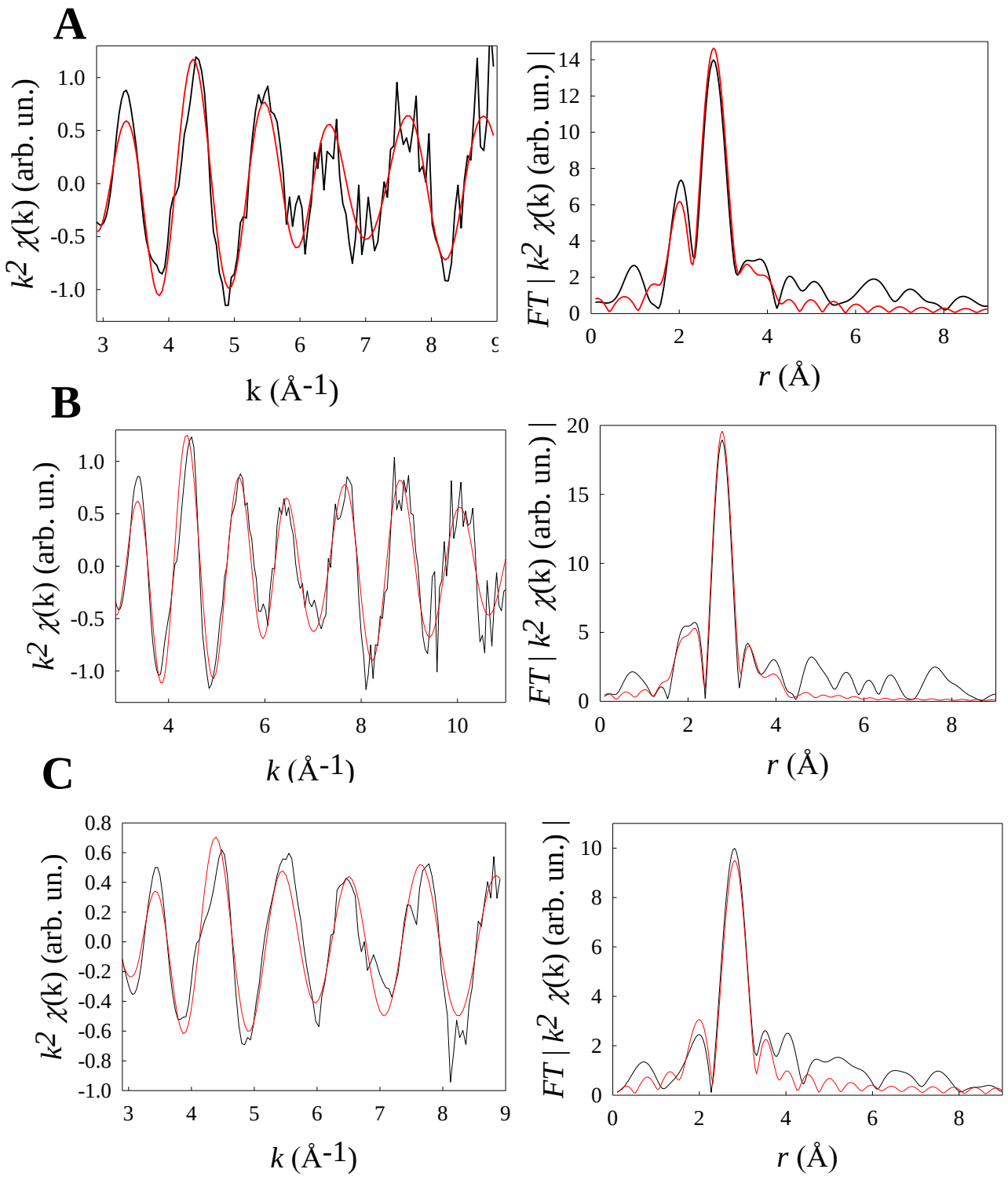

Figure 9.5. Ag–K edge EXAFS signals and the corresponding FTs of the electrode material composed of Ag nanoparticles during the application of an external potential value of −1.2 V (A), −0.1 V (B) and +0.5 V (C). The experimental signal is represented by a black line whereas the theory is indicated by the red one.

Fitting Parameters for Spectrum Recorded at -1.2 V					
Shell	***N***	***Atom***	***r* (Å)**	**σ^2 (Å^2)**	**r^* (Å)**
1	12	Ag	2.88(1)	1.3(1) x10^{-2}	2.889
F = 18.3 %					

Fitting Parameters for Spectrum Recorded at -0.1 V					
Shell	***N***	***Atom***	***r* (Å)**	**σ^2 (Å^2)**	**r^* (Å)**
1	12	Ag	2.872(6)	1.10(6) x10^{-2}	2.889
F = 10.3 %					

Fitting Parameters for Spectrum Recorded at 0.5 V					
Cluster 1: AgCl Multiplicity: 30 %					
Shell	***N***	***Atom***	***r* (Å)**	**σ^2 (Å^2)**	**r^* (Å)**
1	6	Cl	2.84(4)	2.3(8) x10^{-2}	2.735
Cluster 2: Metallic Ag. Multiplicity: 70 %					
Shell	***N***	***Atom***	***r* (Å)**	**σ^2 (Å^2)**	**r^* (Å)**
1	12	Ag	2.86(1)	1.25(9) x10^{-2}	2.889
F = 14.4 %					

Table 9.1. Fitting parameters for EXAFS spectra in Figure 9.5. *r*: Distances, σ^2: Distance variances. Coordination numbers *N* have been kept constant. r^* refers to coordination distances present in literature.

Further considerations can be made on the base of a deeper look of the XANES region of the spectra, in correspondence of the spectral features observed at ca. 25532 and 25553 eV. In the single electron approximations these structures can be attributed to the *1s* → *5p* and to the *1s* → *4f* transitions respectively. Fig. 9.6 shows a comparison of the XANES spectra acquired at -1.2 V and at –0.1 V (at which Cl^- are expected to be adsorbed) in the region between 25490 and 25590 eV.

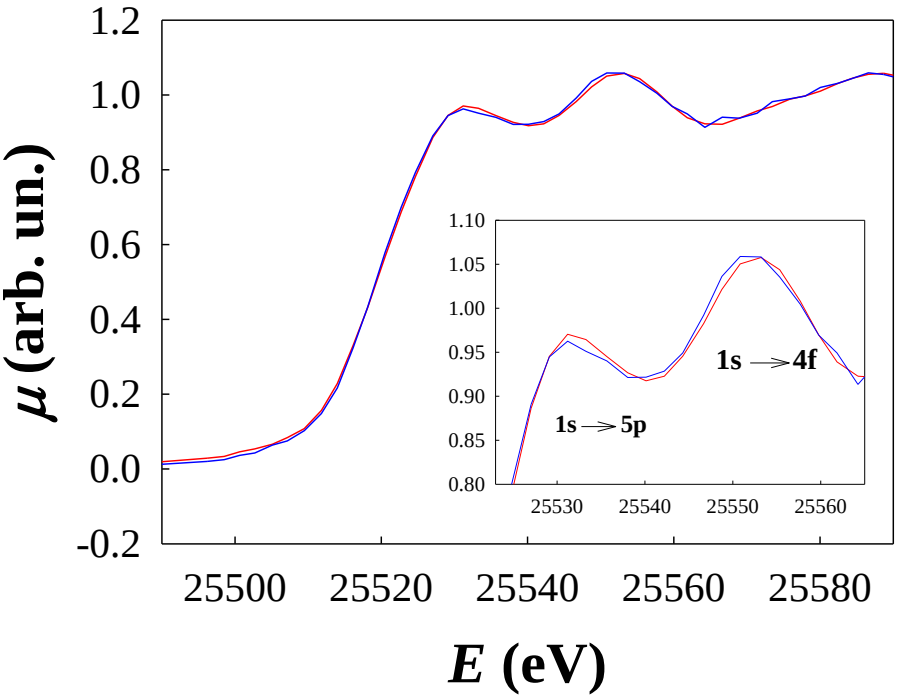

Figure 9.6. Normalized XANES spectrum of Ag electrode at potential equal to –0.1 V (red line) compared to the one at–1.2 V (blue line) in the presence of 0.1 M KCl in 0.1 M $KClO_4$.

The first thing that we note by observing the insight in the figure is that the potential -0.1 V (less negative than -1.2 V) determines an increase in the spectral structure present at ca. 25532 eV and a variation in the shape of the feature at 25553 eV. The only reasonable explanation underneath this experimental evidence is a modification of the electronic structure of Ag determined by the

adsorption of Cl^- anions occurring at -0.1 V. Similar effects characterize the spectral shape of Pd at the K edge[21] (very similar to that of Ag).

Let's discuss the results obtained in presence of the volatile organic halide $CHCl_3$. Fig. 9.7 gives information about the FEXRAV analysis applied to an Ag electrode in presence of 10 mM $CHCl_3$ in 0.1 M $KClO_4$.

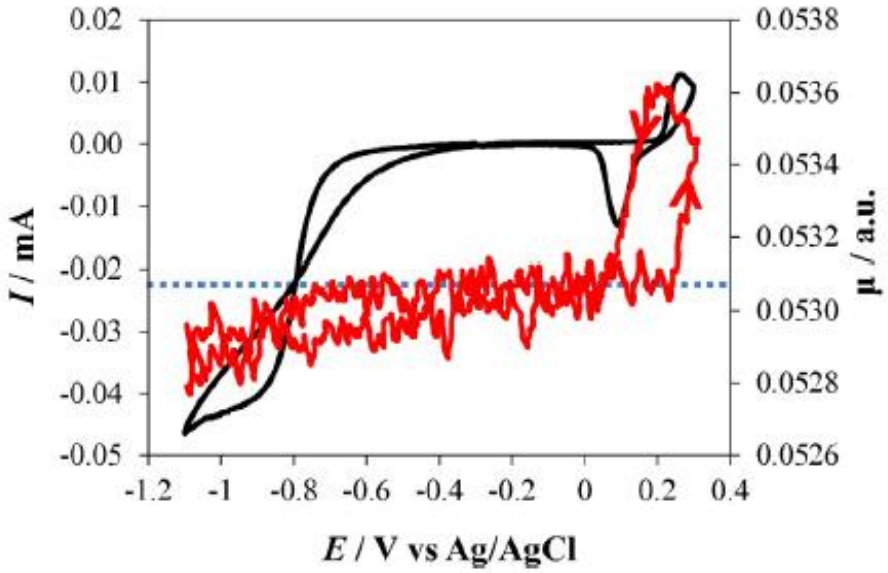

Figure 9.7. CV (full black line) and FEXRAV (dashed red line) signals for Ag electrodes in the presence of 10 mM $CHCl_3$ in aqueous 0.1 M $KClO_4$, at 1 mV/s.

The CV, carried out in the potential range between -1.1 V and +0.3 V, is represented by the black line and accounts for the formation of AgCl at +0.3 V: the presence of an Ag oxidation peak is a support for the presence of Cl^- ions generated by the dehalogenation electroreduction. When the potential is reversed, a peak associated to the electroreduction of AgCl appears. FEXRAV result, indicated by the red line, is in good agreement with the electrochemistry: the increase in the signal at ca. +0.3 V is due to Ag oxidation while the decrease at ca. +0.1 V accounts for its reduction. Furthermore, FEXRAV signal is marked by a slight (but well above the noise level) decrease in the first potential scan performed from -0.3 V to -1.1 V. This trend is reversible as the absorption

coefficient increases back to the original value if the potential scan is reversed. In order to clarify the reason behind this phenomenon, a XANES spectrum was acquired while applying a potential equal to -0.3 V. Afterwards, this was compared to a XAS spectrum acquired in absence of $CHCl_3$ (Fig. 9.8).

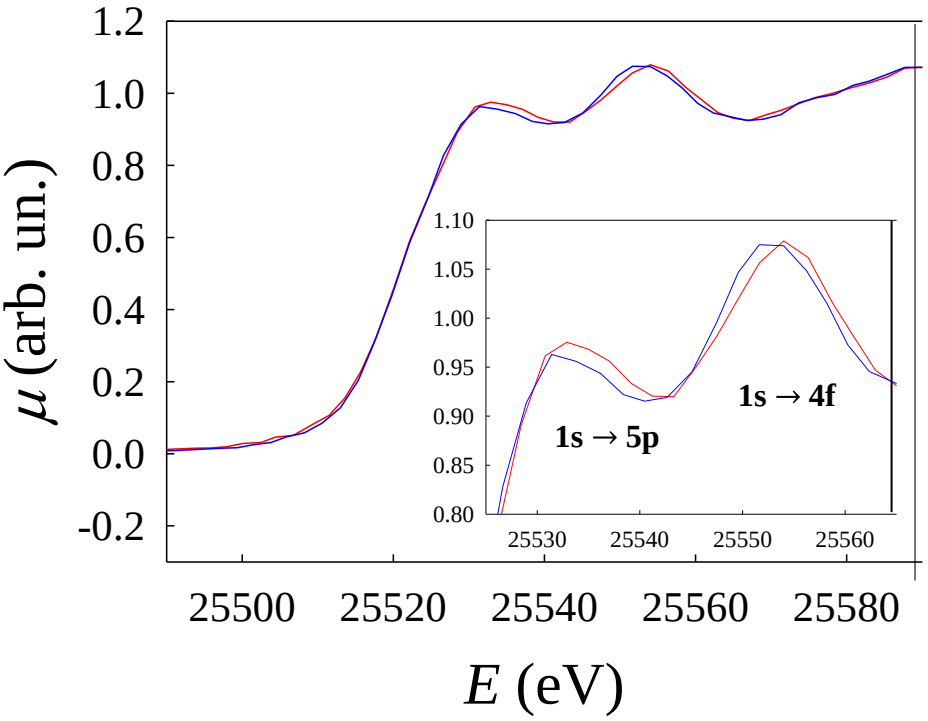

Figure 9.8. Normalized XANES spectrum of Ag electrode at potential –0.3 V in presence (red line) and in absence (blue line) of 10 mM $CHCl_3$ in 0.1 M $KClO_4$.

The effect determined by the presence of the organic chloride is analogous to that observed in Fig. 9.6, which compares the XANES spectra recorded in conditions where Cl^- ions are adsorbed (-0.1 V) and in conditions where Cl^- ions are desorbed (-1.2 V). The similarity between the two cases is a clear suggestion that a similar mechanism is involved for the presence and absence of $CHCl_3$. Therefore, it is reasonable to assess that polarizing the electrode at -0.3 V, in presence of $CHCl_3$, determines the absorption of the organic halide on the surface of Ag. On the base of this assumption, it is possible to make further

considerations about the mechanism governing the process under investigation. The decreasing trend of FAXRAV signal observed starting from a condition in which $CHCl_3$ is adsorbed (-0.3 V) (Fig. 9.7) and going towards more negative potentials (-1.1 V) can be explained by the occurrence of $CHCl_3$ desorption after its electroreduction. This is confirmed by the significant current observed in the CV. The results presented so far provide support to the exceptional electrocatalytic activity of Ag in the dechlorination of organic pollutants.

9.3. Br-K EDGE AND THE ADSORPTION OF PhBr

The aim of the second experiment, carried out on Ag electrodes, is the study of the adsorption of an organic bromide: 2-bromophenol. This compound provides a good model that can be investigated also from a different absorption edge, still belonging to the hard X-ray region: Br-K edge (13474 eV). This is preferable to the Ag-K edge because it allows access to the valence states of the halogen, which are directly involved in the electrochemically driven interaction with Ag.
In order to start the investigation of the interaction between bromide and Ag a FEXRAV analysis was carried out in presence of a 150 µM solution of KBr. The CV was performed in the potential range from -0.4 V to -1.0 V starting from -0.4 V (Vs Ag/AgCl), while maintaining the energy fixed to 13488.2 eV (Fig. 9.10).

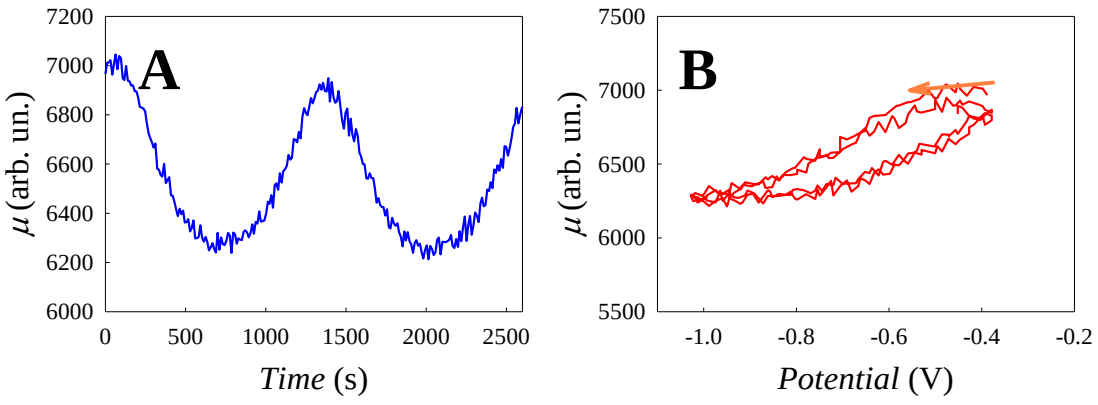

Figure 9.10. FEXRAV signal for Ag electrode in presence of a 150 µM solution of KBr in the potential range -0.4 – -1.0 V (Vs Ag/AgCl) as a function of time (A) and of the potential (B).

This value was chosen in correspondence of AgBr absorption edge in order to gain the maximum contrast in the absorption coefficient μ. The aim was to investigate the region in which Br^- adsorption is expected to take place. The absorption coefficient assumes its largest value at -0.4 V and gradually decreases as the potential is reduced, reaching its lowest value at -1.0 V: from the reverse path we can observe that the phenomenon is reversible. Potential -1.0 V represents the electrochemical conditions at which Br^- ions are in solution and do not interact with Ag. Since the oxidation of Ag to AgBr does not occur for potentials lower than 0.0711 V[22], the variation in the absorption coefficient can only be attributed to a modification in the local environment of Br^- due to its adsorption onto the Ag electrode. In order to check the reproducibility of the process two cycles were performed.

Fig. 9.11 illustrates the Br-K edge spectral profile for three different local environments of Br: 150 µM aqueous bromide (green line), silver bromide (blue line) and for a 150 µM solution of KBr while applying a potential equal to -0.2 V (red line), conditions in which Br^- is expected to be adsorbed. This last spectrum is the average of three spectra acquired in the same conditions.

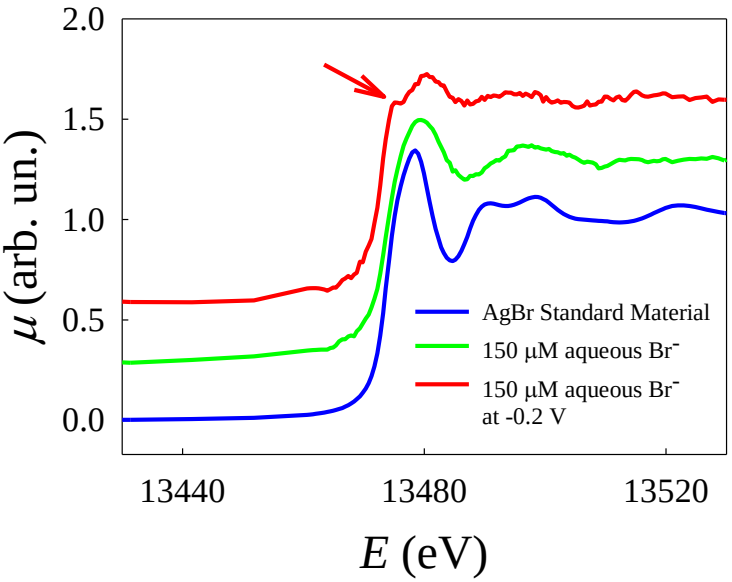

Figure 9.11. Normalized Br-K edge XANES spectra of AgBr standard material (blue line), of 150 µM aqueous bromide (green line) and for a 150 µM solution of KBr while applying a potential equal to -0.2 V (Vs Ag/AgCl).

In the cases of 150 μM aqueous Br^- without potential and of AgBr no pre-peaks are observed. If a potential of -0.2 V is applied to the solution of KBr, a peak appears in the pre-edge region: this signal is ascribed to the *1s* → *4p* electronic transitions. This difference, observed in the pre-edge region, can be explained on the base of the electronic configuration of Br. Br^- anion is characterized by external configuration $3d^{10}4s^24p^6$. *4p* electronic states are thus completely filled both in the aquoion and in AgBr, where the degree of iconicity of the Ag—Br bond is very high. For these two cases no absorption peaks are present in the pre-edge region as no *p* states are available for localized electronic transitions. Observing the XANES spectrum recorded at applied potential -0.2 V in presence of a 150 μM solution of KBr, we note a pre-peak at 13475 eV (indicated by the arrow). This is a clear experimental evidence that in these conditions *4p* electronic states are not completely filled and therefore the local electronic environment of Br is different from both that of the aquoion and that of the silver bromide. It is reasonable to assume that the electrochemically driven process leads to the adsorption of Br on Ag causing a partial emptying of *4p* states. In order to confirm this assessment the whole XAS spectrum was considered and the EXAFS signal was extracted and fitted.

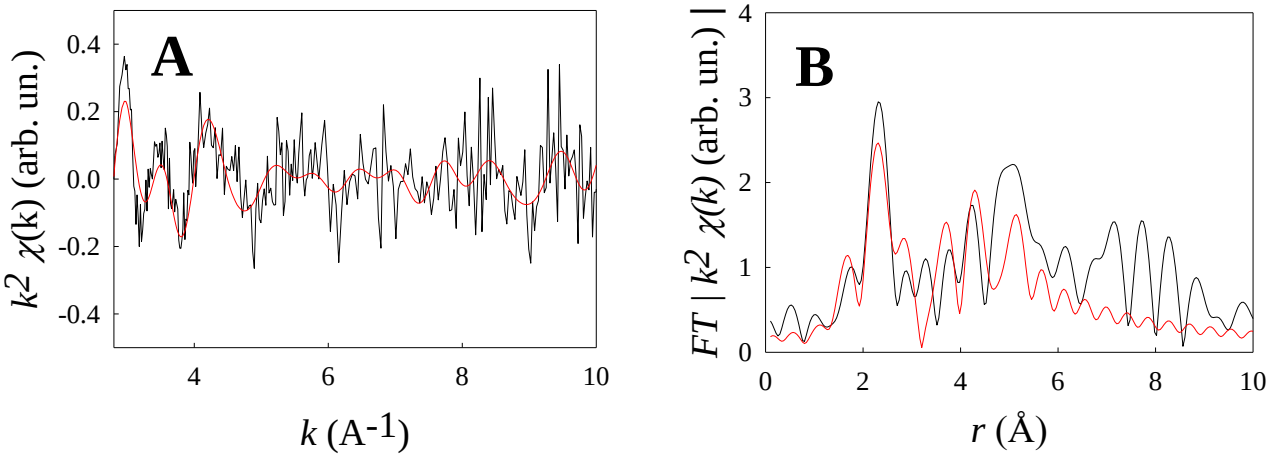

Figure 9.12. Br–K edge EXAFS signals (A) and the corresponding FT (B) obtained at potential -0.2 V in presence of a 150 μM solution of KBr. The experimental is represented by the black line while the theory is the red one.

Fig 9.12 shows the EXAFS modulations (A) and the corresponding FT (B). Oscillations are visible up to 10 Å^{-1} but the low signal/noise ratio, due to the fact that the phenomenon under investigation occurs at an interface, gives rise to many peaks at large distances in the FT and does not allow to obtain *F* values lower than 30 %. The EXAFS fitting was performed by means of EXCURVE code[20]: full multiple scattering was employed in presence of a cluster composed of five shells of Ag atoms and characterized by C_{4V} punctual symmetry (Fig. 9.13). The choice of such a geometrical surrounding was based on the assumption that bromine atoms adsorbs onto the Ag electrode in crystallographic positions corresponding to Ag sites. On that basis each Br atom can be considered as situated in the apical position of an octahedron constituted of Ag atoms: the first shell comprises the four Ag atoms in the equatorial position and the second one consists of the one Ag atom present in the other apical position. The other shells, entirely made of silver atoms, are constructed considering the *fcc* arrangement of the metal. Tab. 9.2 shows the best fitting parameters obtained for the EXAFS spectrum illustrated in Fig. 9.12.

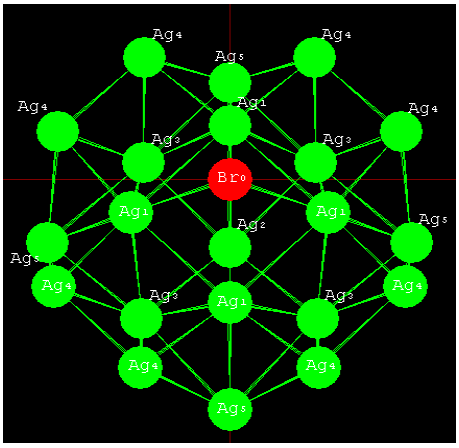

Figure 9.13. Scheme of the cluster employed in the fitting of the EXAFS spectrum obtained at -0.2 V in presence of a 150 µM solution of KBr.

Shell	***N***	***Atom***	***r* (Å)**	***σ*^{2} (Å^2)**	***B1* (Å^3)**	***C1* (Å^4)**
1	4	Ag	2.66(3)	3.1(8) x10^{-2}	3(2) x10^{-1}	6.9(4) x10^{-3}
2	1	Ag	3.9(1)	0(1) x10^{-2}	-	-
3	4	Ag	4.2(2)	1(2) x10^{-2}	-	-
4	8	Ag	4.1(2)	3(4) x10^{-2}	-	-
5	4	Ag	5.11(7)	3(8) x10^{-3}	-	-
F = 33.4 %						

Table 9.2. Fitting parameters for EXAFS spectra in Figure 9.12. *r*: Distances, *σ*^{2}: Distance variances, *B1*: 3rd cumulant or *Skewness*, *C1*: 4th cumulant or *Kurtosis*. Coordination numbers *N* have been kept constant.

For the first coordination shell, also the 3rd and the 4th cumulants were considered and fitted. The former, also defined *Skewness*, represents a measure of the asymmetry of the probability distribution while the latter, also called *Kurtosis*, refers to the deviation from the Gaussianity. The distance found for the first shell of Ag atoms is smaller if compared to literature data referred to Br Nearest Neighbours in silver bromide (2.83 Å)[23]. This is reasonably explained by the presence of a partially covalent interaction and therefore is a further support to the fact that Br, when adsorbed, is characterized by a different local electronic environment.

Let's turn the discussion to the results obtained in presence of the brominated organic model compound. In order to verify the structure of the 2-bromophenol we acquired and analyzed a full XAS spectrum of a 150 µM solution of bromophenol. Fig. 9.14 shows EXAFS spectrum and the corresponding FT: the experimental is the black line whereas the best fit obtained by means of EXCURVE[20] is the red line.

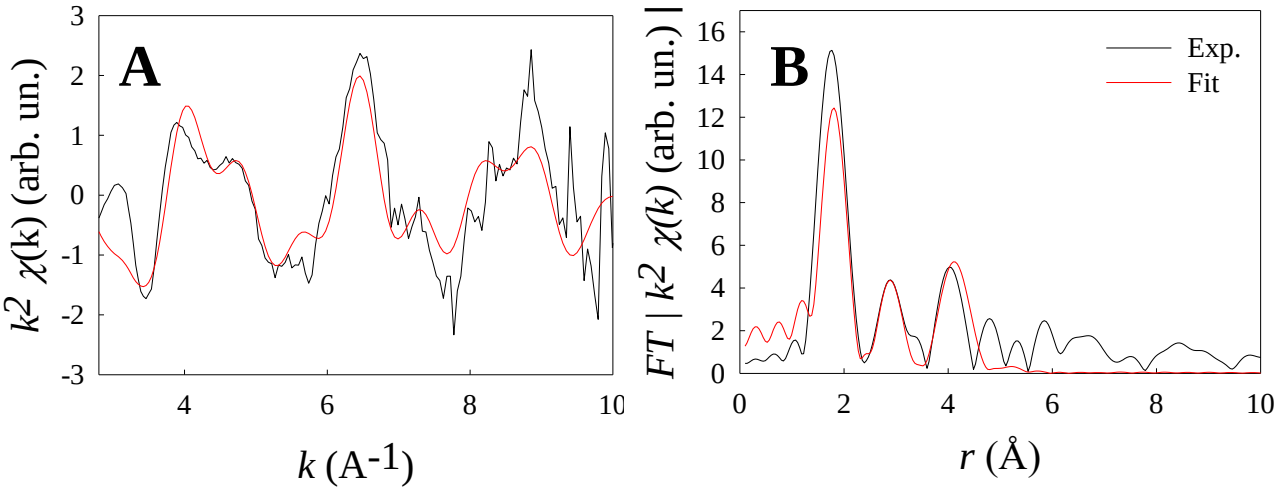

Figure 9.14. Br–K edge EXAFS signals (A) and the corresponding FT (B) referred to a 150 µM solution of bromophenol.

Tab. 9.3 illustrates the parameters obtained for the best fit and Fig. 9.15 presents a scheme of the cluster employed. This is made of seven shells

containing one atom each: EXAFS fitting was carried out applying multiple scattering and imposing C_1 point symmetry to the central atom.

Shell	*N*	*Atom*	*r* (Å)	σ^2 (Å^2)
1	1	C	1.89	4(2) x10^{-3}
2	1	C	2.88	1.2(5) x10^{-2}
3	1	C	2.88	1.2(5) x10^{-2}
4	1	C	4.14	4(3) x10^{-3}
5	1	C	4.15	4(3) x10^{-3}
6	1	C	4.66	2(3) x10^{-2}
7	1	O	3.4(1)	2(2) x10^{-2}
F = 29.7 %				

Table 9.3. Fitting parameters for EXAFS spectra in Figure 9.14. *r*: Distances, σ^2: Distance variances.

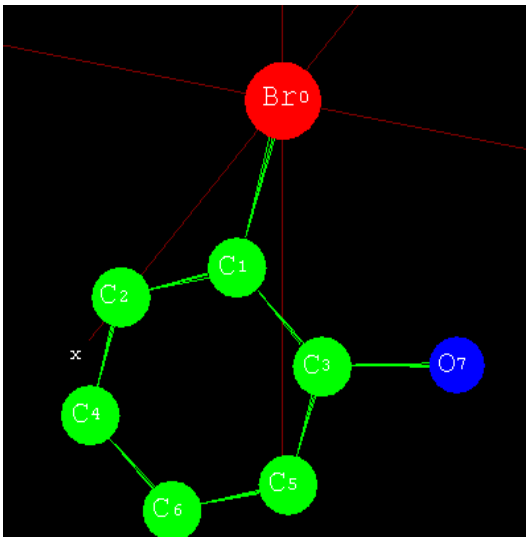

Figure 9.15. Scheme of the cluster employed in order to fit the spectrum shown in Fig. 9.14.

In order to preserve the interatomic distances of the organic compound the cluster was treated as a stable unit. On the basis of electrochemical measurements (Fig. 9.16) we investigated the local structure of Br at potential -0.8 V, at which the bromophenol is supposed to be adsorbed.

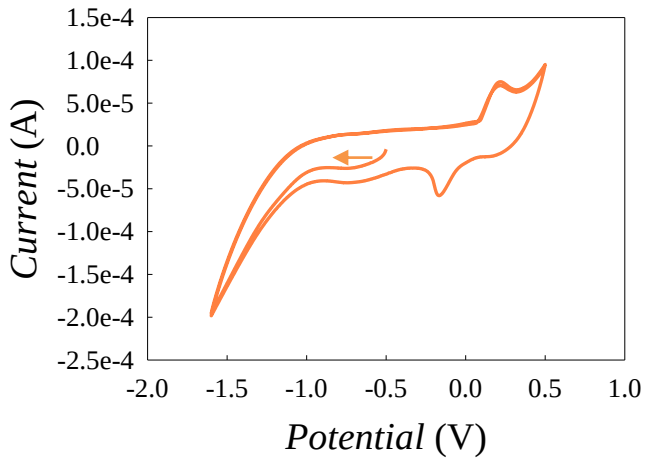

Figure 9.16. CV performed in the potential range within -1.6 V and 0.5 V, starting from -0.5 V and applying 0.05 V/s. The desorption peak can be seen at ca. -0.8 V. Potentials are Vs Ag/AgCl.

Fig. 9.17 compares the Br-K edge XANES spectra of a 150 µM solution of 2-bromophenol (blue line), of the same solution while applying a potential equal to -0.8 V (red line) and of the adsorbed bromides (black line). In all cases the pre-peak ascribed to the *1s* → *4p* transition is observed: the covalent bond between Br and C in the bromphenol determines a partial emptying in the *4p* states of Br.

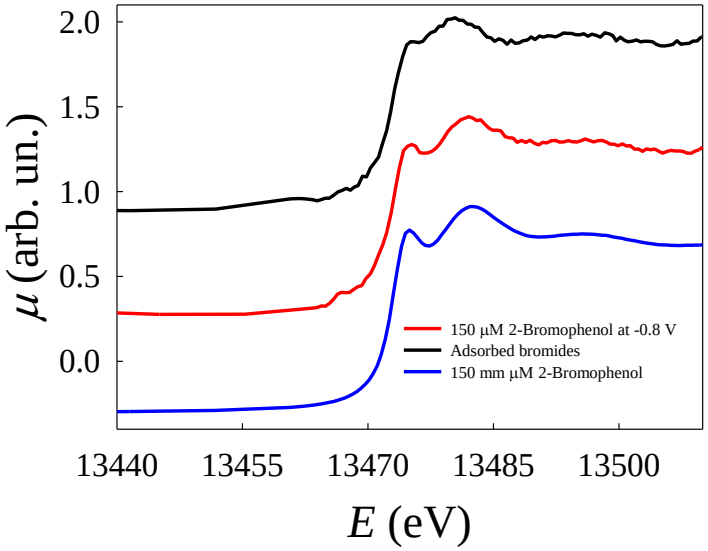

Fig. 9.17. Br-K edge XANES spectra of a 150 µM solution of 2-bromophenol (blue line), of the same solution applying a potential equal to -0.8 V (red line) and of the adsorbed bromides (black line).

A detailed observation of the spectral profile in the three pre-edge regions points out small variations in the shape of the pre-peaks: the aqueous 2-bromophenol spectrum presents a peak characterized by a sharp maximum while the adsorbed bromides give raise to "plateau-like" structure in correspondence of the maximum. The intermediate shape observed with the application of potential -0.8 V suggests an interaction between the Br atoms of the organic compound and the Ag of the electrode. In this case, EXAFS signal was extracted and fitted (Fig. 9.18). The experimental is represented by the black line while the best fit is the red one: although the oscillations are visible up to 9 $Å^{-1}$ the low signal to noise ratio prevents us from obtaining a good fit index.

In Tab. 9.4. the best fitting parameters obtained are presented. EXAFS fit is compatible with a model constituted of two clusters: *(i)* an organic part (contained in the bromophenol) and *(ii)* the metallic part (Ag in a *fcc* arrangement). This fit, carried out treating the bromophenol as a stable unit, is in agreement with the previous assumptions made by observing the XANES spectrum. On the basis of this analysis we can hypothesize that at -0.8 V (Vs Ag/AgCl) 2-bromophenol is adsorbed onto Ag.

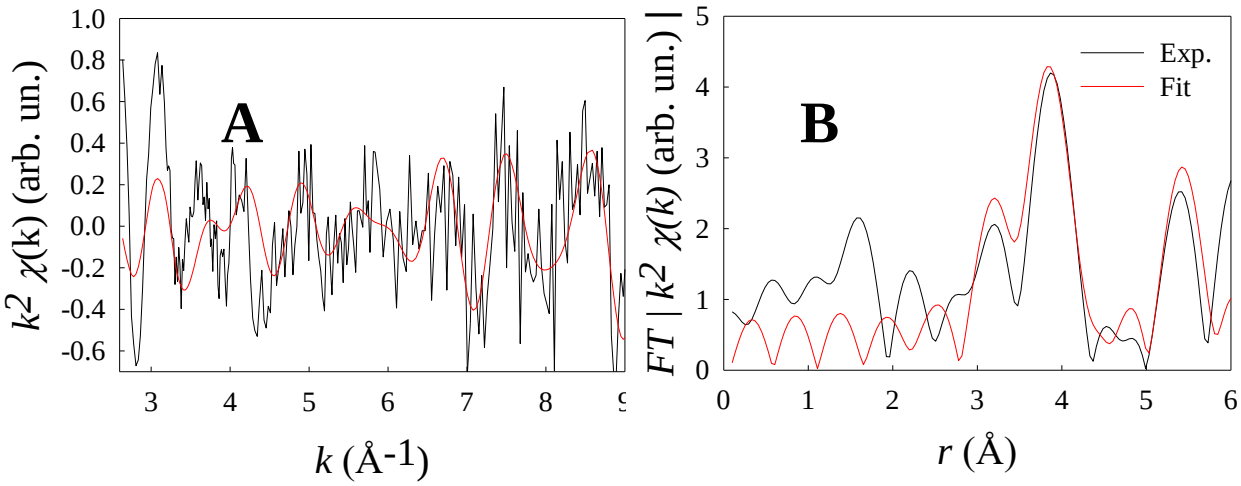

Figure 9.18. Br–K edge EXAFS signals (A) and the corresponding FT (B) referred to a 150 µM solution of bromophenol applying a potential of -0.8 V.

Shell	N	Atom	r (Å)	σ^2 (Å^2)
1	1	C	1.89	7(5) x10^{-2}
2	1	C	2.73	3(4) x10^{-2}
3	1	C	2.90	1(2) x10^{-2}
4	1	C	4.02	0(4) x10^{-2}
5	1	C	4.15	0(3) x10^{-2}
6	1	C	4.59	1(7) x10^{-2}
7	1	O	3.20(6)	0(1) x10^{-2}
8	5	Ag	3.57(3)	7(3) x10^{-3}

9	4	Ag	3.84(6)	$9(8)\ x10^{-3}$
10	8	Ag	4.06(8)	$3(2)\ x10^{-2}$
11	4	Ag	4.89(4)	$6(5)\ x10^{-3}$
F: 50.3 %				

Table 9.4. Fitting parameters for EXAFS spectra in Figure 9.18. *r*: Distances, σ^2: Distance variances.

9.4. CONCLUSIONS

This chapter illustrates two experiments with the aim of studying the exceptional electrocatalytic power of Ag in the dehalogenation of organic halides: in the first one XAS investigation was performed at the Ag-K edge and in the second one at the Br-K edge.

In the first case we investigated the process of C-Cl electro-cleavage in the $CHCl_3$ organic chloride. XANES spectral shape and electrochemical measurements suggest that at -0.3 V (Vs Ag/AgCl) trichloromethane is adsorbed onto the Ag electrode and, by comparison to the results obtained in presence of a 0.1 M solution of KCl, it is possible to assume that the adsorption process of $CHCl_3$ is very similar to that of Cl^-. Furthermore, starting from a condition in which $CHCl_3$ is adsorbed and polarizing the electrode to more negative potentials, we observe a decrease in FEXRAV signal thus accounting for a desorption as a consequence of electroreduction of the organic compound.

In the second experiment we investigated the interaction of Ag electrodic material and 2-bromophenol. The low signal/noise ratio observed in the XAS spectra and associated to the nature of the system under investigation made it difficult to treat data. However, on the basis of the model compatible with the

experimental signal at -0.8 V, we can hypothesize that in these conditions 2-bromophenol is adsorbed.

REFERENCES:

[1] J. Simonet, in: M. Stratmann (Ed.), Electrochemistry applied to organic synthesis: principles and main achievements, encyclopedia of electrochemistry (2007), 5, 317–376;
[2] S. Rondinini, P.R. Mussini, G. Sello, and E. Vismara, *J. Electrochem. Soc.* (1998), 145, 1108–1112;
[3] O. Scialdone, A. Galia, S. Sabatino, G.M. Vaiana, D. Agro, A. Busacca, and C. Amatore, *ChemElectroChem* (2014), 1, 116–124;
[4] A.A. Isse, C. Durante, and A. Gennaro, *Electrochem. Commun* (2011), 13, 810–813;
[5] F. Amemiya, D. Horii, T. Fuchigami, and M. Atobe *J. Electrochem. Soc.*(2008), 155, E162–E165;
[6] S. Manzetti, E.R. van der Spoel, and D. van der Spoel, Chem. Res. Toxicol. (2014), 27, 713–737;
[7] WHO World Health Organization, Agents Classified by the IARC Monographs, vol. 1–112, International Agency for Research on Cancer (2015);
[8] Y.-F. Huang, D.-Y. Wu, A. Wang, B. Ren, S. Rondinini, Z.-Q. Tian, and C. Amatore, *J. Am. Chem. Soc.* (2010), *132*, 17199–17210;
[9] S. Rondinini, P. R. Mussini, F. Crippa, and G. Sello, *Electrochem. Commun.* (2000), 2, 491–496;
[10] A. A. Isse, S. Gottardello, C. Maccato, and A. Gennaro, *Electrochem. Commun.* (2006), 8, 1707–1712;
[11] S. Rondinini, P. R. Mussini, P. Muttini, and G. Sello, *Electrochim. Acta* (2001), 46, 3245–3258;
[12] A. A. Isse, A. De Giusti, A. Gennaro, L. Falciola, and P. R. Mussini, *Electrochim. Acta* (2006), 51, 4956–4964;
[13] O. Lugaresi, H. Encontre, C. Locatelli, A. Minguzzi, A. Vertova, S. Rondinini, and C. Comninellis, *Electrochem. Commun.* (2014), 44C, 63–65;
[14] A. Minguzzi, O. Lugaresi, G. Aricci, S. Rondinini, and A. Vertova, *Electrochem. Commun.* (2012), 22, 25–28;
[15] C. Durante, A.A. Isse, G. Sandonà, and A. Gennaro, *Appl. Catal. B Environ.* (2009), 88, 479–489;
[16] O. Scialdone, A. Galia, L. Gurreri, and S. Randazzo, *Electrochim. Acta* (2010), 55, 701–708;
[17] F. D'Acapito, A. Trapananti, and A. Puri, *J. Phys.: Conf. Ser.* (2016), 712, 012021;
[18] A. Minguzzi, O. Lugaresi, C. Locatelli, S. Rondinini, F. D'Acapito, E. Achilli and P. Ghigna, *Anal. Chem.* (2013), 85, 7009–7013;
[19] B. Ravel, and M. Newville, *J. Synchrotron Radiat.* (2005), 12, 537– 541;
[20] N. Binsted, S.S. Hasnain *J. Synch. Rad.* (1996), 3, 185;
[21] A.L. Bugaev, V.V. Srabionyan, A.V. Soldatov, L.A. Bugaev, J.A. van Bokhoven, *J. Phys. Conf. Ser.* (2013), 430, 012028;
[22] R. Parsons, Handbook of Electrochemical Constants, Butterworths Scientific Publications, London, 1959;
[23] http://rruff.geo.arizona.edu/AMS/amcsd.php.

10. FINAL REMARKS

This PhD thesis dealt with research works aimed at shading light onto the mechanism and kinetics of electrocatalytic and photo-electrocatalytic processes of increasing interest. Electrochemical and photo-electrochemical methods were coupled to X-ray techniques for an *in situ* and *in operando* investigation: X-ray absorption analysis were performed to study the local chemical and electronic environment of the materials considered while applying specific electrochemical and/or photochemical conditions.

The electrodic materials chosen for the experiments play a key role in the catalysis of two processes: the water splitting reaction and the dehalogenation of organic pollutants. IrO_x based electrodes show great potentialities in the electrocatalysis of the former process: thanks to X-rays as local structure probe, a deeper understanding about the mechanism and kinetics of the electrochemical reaction was gained. Associating this electrocatalytic material to hematite it was possible to obtain and study bilayer architectures for the UV-Vis light-induced catalysis of the water splitting reaction. Other electrodes considered provide a sustainable and cheaper material for the photo-elecrocatalysis of the water oxidation reaction: these are constituted of $Ni(OH)_2$ as electrocatalytic domain and hematite as semiconductor part. The last material taken into account for the water splitting process is Cu(I) oxide, one of the most important candidates for energy conversion devices. In particular the attention was focused on the characterization and the stability of the precursor: a Cu(II) lactate solution.

As far as the electrochemical dehalogenation of organic pollutants is concerned, this thesis focused the attention onto Ag electrocatalyst. Two organic halides

were considered as model compounds in the experiments performed: trichloromethane and bromophenol.

All the *in situ* and *in operando* experiments were carried out at the E.S.R.F. (European Synchrotron Radiation Facility in Grenoble, France) on different beamlines depending on the experimental needs associated to the samples and to the electrochemical programs applied. In order to perform the measurements, adequate spectro-electrochemical devices were designed and built so that they could host the three–electrodes setup in the beamline hutches. Thanks to FEXRAV (Fixed Energy X-ray Absorption Voltammetry) it was possible to identify the potential windows in which the most important processes occur. This method therefore served as a preliminary study in order to chose the most suitable potentials for the subsequent full-XAS investigation. The XANES (X-ray Absorption Near Edge Spectroscopy) part allowed to study the local geometric and electronic environments and the EXAFS (Extended X-ray Absorption Fine Structure) oscillations brought information associated to the chemical surrounding within 10 Å. Moreover, the employment of time-resolved energy dispersive XAS was successful in the investigation of the kinetics associated to the processes considered. In presence of photo-electrodes, composed of an electrocatlytic part and a semiconductor domain, the experimental setup was complicated by the presence of a UV-Vis light source acting as a solar simulator. In some cases the study of the mechanisms and the kinetics was further improved by a X-ray multi-bunch based setup, which allowed to gain a time resolution of hundreds of nanoseconds.

To conclude, the experiments carried out not only proved the exceptional catalytic power and the most important properties of the samples but also identified the best running conditions of the electrochemical tools. Furthermore, the techniques employed displayed strategies that can be useful in the investigation of other (photo-)electrochemical devices.

11. PUBLICATIONS – E. ACHILLI

[1] Alessandro Minguzzi, Ottavio Lugaresi, Cristina Locatelli, Sandra Rondinini, Francesco D'Acapito, **Elisabetta Achilli**, Paolo Ghigna *Fixed Energy X-ray Absorption Voltammetry*. Anal. Chem. (2013), 85, 7009—7013;

[2] Alessandro Minguzzi, Ottavio Lugaresi, **Elisabetta Achilli**, Cristina Locatelli, Alberto Vertova, Paolo Ghigna, Sandra Rondinini *Observing the Oxidation State Turnover in Heterogeneous Iridium-Based Water Oxidation Catalysts*. Chem. Sci. (2014), 5, 3591—3597;

[3] Alessandro Minguzzi, Cristina Locatelli, Ottavio Lugaresi, **Elisabetta Achilli**, Giuseppe Cappelletti, Marco Scavini, Mauro Coduri, Paolo Masala, Benedetta Sacchi, Alberto Vertova, Paolo Ghigna, Sandra Rondinini *Easy Accommodation of Different Oxidation States in Iridium Oxide Nanoparticles With Different Hydration Degree as Water Oxidation Electrocatalysts*. ACS Catal. (2015), 5, 5104—5115;

[4] **Elisabetta Achilli**, Alessandro Minguzzi, Ottavio Lugaresi, Cristina Locatelli, Sandra Rondinini, Giorgio Spinolo, Paolo Ghigna *In Situ Dispersive EXAFS in Electrocatalysis: The Investigation of the Local Structure of IrOx in Chronoamperometric Conditions as a Case Study*, Journal of Spectroscopy (2014), 2014, 480102;

[5] **Elisabetta Achilli**, Alessandro Minguzzi, Albrto Visibile, Cristina Locatelli, Sandra Rondinini, Ferdinando Auricchio, Stefania Marconi, Paolo Ghigna *3D-printed Spectroelectrochemical and Photo-spectroelectrochemical devices for in situ and in operando X-Ray Absorption Spectroscopy investigation,* J. Synchrotron Rad. (2016), 23, 622–628;

[6] Sandra Rondinini, Ottavio Lugaresi**, Elisabetta Achilli**, Cristina Locatelli, Alessandro Minguzzi, Alberto Vertova, Paolo Ghigna, Christos Comninellis *Fixed*

Energy X-ray Absorption Voltammetry and Extended X-ray Absorption fine Structure of Ag nanoparticle electrodes, J.Electroanal. Chem. (2016), 766, 71–77;

[7] Tomasz Baran, Martina Fracchia, Alberto Vertova, **Elisabetta Achilli**, Alberto Naldoni, Francesco Malara, Giacomo Rossi, Sandra Rondinini, Paolo Ghigna, Alessandro Minguzzi, Francesco D'Acapito *Operando and Time-Resolved X-Ray Absorption Spectroscopy for the Study of Photoelectrode Architectures,* Electrochim. Acta (2016), 207, 16—21;

[8] Sandra Rondinini, Alessandro Minguzzi, **Elisabetta Achilli**, Cristina Locatelli, Giovanni Agostini, Sakura Pascarelli, Giorgio Spinolo, Alberto Vertova, Paolo Ghigna *The dynamics of pseudocapacitive phenomena studied by Energy Dispersive XAS on hydrous iridium oxide electrodes in alkaline media*, Electrochim. Acta (2016), 212, 247—253;

[9] Tomasz Baran, Szymon Wojtyla, Cristina Lenardi, Alberto Vertova, Paolo Ghigna, **Elisabetta Achilli**, Martina Fracchia, Sandra Rondinini, Alessandro Minguzzi *An Efficient Cu_xO Photocathode for Hydrogen Production at Neutral pH: New Insight from Combined Spectroscopy and Electrochemistry*, ACS Appl. Mater. Interfaces (2016), 8, 21250—21260;

[10] Alessandro Minguzzi, Ottavio Lugaresi, **Elisabetta Achilli**, Francesco D'Acapito, Alberto Naldoni, Francesco Malara, Cristina Locatelli, Alberto Vertova, Sandra Rondinini, Paolo Ghigna *Observation of charge transfer cascade in α-Fe_2O_3/IrO_2 photoanodes by in-operando X-rays absorption spectroscopy,* PCCP**, in progress**;

[11] **Elisabetta Achilli**, Ottavio Lugaresi, Cristina Locatelli, Sandra Rondinini, Giovanni Agostini, Sakura Pascarelli, Giorgio Spinolo, Paolo Ghigna *Kinetics of ion diffusion during faradic phenomena: in in-situ dispersive XAS investigation on amorphous IrO_x*, **in progress**;

[12] **Elisabetta Achilli**, Alberto Visibile, Sara Morandi, Alberto Vertova, Alessandro Minguzzi, Sandra Rondinini, Paolo Ghigna *Structure and stability of Copper(II) lactate Complex in Alkaline Solution: a Case Study by dispersive XAS*, **in progress**.